



저작자표시-비영리-변경금지 2.0 대한민국

이용자는 아래의 조건을 따르는 경우에 한하여 자유롭게

- 이 저작물을 복제, 배포, 전송, 전시, 공연 및 방송할 수 있습니다.

다음과 같은 조건을 따라야 합니다:



저작자표시. 귀하는 원저작자를 표시하여야 합니다.



비영리. 귀하는 이 저작물을 영리 목적으로 이용할 수 없습니다.



변경금지. 귀하는 이 저작물을 개작, 변형 또는 가공할 수 없습니다.

- 귀하는, 이 저작물의 재이용이나 배포의 경우, 이 저작물에 적용된 이용허락조건을 명확하게 나타내어야 합니다.
- 저작권자로부터 별도의 허가를 받으면 이러한 조건들은 적용되지 않습니다.

저작권법에 따른 이용자의 권리는 위의 내용에 의하여 영향을 받지 않습니다.

이것은 [이용허락규약\(Legal Code\)](#)을 이해하기 쉽게 요약한 것입니다.

[Disclaimer](#)

工學博士學位論文

**Fabrication of Zinc Oxide Nanostructure/ Poly(vinylidene  
fluoride) Hybrid Thin Films and Their Application for  
Pressure Sensors and Acoustic Actuators**

산화아연 나노구조체/폴리플루오르화비닐리덴 기반 혼합 박막  
제조 및 압전 센서와 음향작동기 응용

2015年 8月

서울대학교 大學院

化學生物工學部

**James S. Lee**

**Fabrication of Zinc Oxide Nanostructure/ Poly(vinylidene fluoride) Hybrid Thin Films and Their Application for Pressure Sensors and Acoustic Actuators**

산화아연 나노구조체/폴리플루오르화비닐리덴 기반 혼합 박막  
제조 및 압전 센서와 음향작동기 응용

指導教授: 張 正 植

이 論文을 工學博士 學位論文으로 提出함

2016年 5月

서울대학교 大學院

化學生物工學部

**James S. Lee**

**James S. Lee** 의 工學博士 學位論文을 認准함

2016年 5月

委員長 \_\_\_\_\_ (인)

副委員長 \_\_\_\_\_ (인)

委 員 \_\_\_\_\_ (인)

委 員 \_\_\_\_\_ (인)

委 員 \_\_\_\_\_ (인)

**Fabrication of Zinc Oxide Nanostructure/ Poly(vinylidene  
fluoride) Hybrid Thin Films and Their Application for  
Pressure Sensors and Acoustic Actuators**

by

James S. Lee

Submitted to the Graduate School of Seoul National University

in Partial Fulfillment of the Requirements

for the Degree of Doctor of Philosophy

May, 2016

Thesis Adviser: Jyongsik Jang

## **ABSTRACT**

As a representative piezoelectric material, poly(vinylidene difluoride) (PVDF) and its copolymers have been widely used owing to their light weight, non-toxicity and ease of processing. In general, the piezoelectricity refers to the ability of a material to generate a piezoelectric potential in response to an external force, and thus the enhanced dielectric property like permittivity is a key factor for improving the sensitivity of PVDF-based electronic devices. For this reason, inorganic fillers with high dielectric constants such as zinc oxide (ZnO) have been dispersed into the PVDF matrix. Since the piezoelectric behavior occurred in crystals that have anisotropic unit cells or in macroscopically separated regions with different charges, the coefficient value for piezoelectric strain constant of PVDF increased via addition of the inorganic fillers, which resulted in the enhanced PVDF based device ability.

This dissertation describes the three different ZnO/PVDF thin films were prepared for tactile sensor, wireless health care system and acoustic actuator by piezoelectricity and pyroelectricity enhanced hybrid film. First, an 80- $\mu\text{m}$ -thick film (which is around 15% of the thickness of the human epidermis), which is a highly sensitive hybrid bifunctional gauge sensor, and was fabricated from

PVDF and rod-like ZnO nanostructures with graphene electrodes. Using this film, we were able to simultaneously measure pressure and temperature in real time. The pressure was monitored from the change in the electrical resistance via the piezoresistance of the material, and the temperature was inferred based on the recovery time of the signal. Our thin film system enabled us to detect changes in pressure as small as 10 Pa that is pressure detection limit was  $10^3$ -fold lower than the minimum level required for artificial skin, and to detect temperatures in the range 20–120 °C. Second, highly sensitive, wearable and wireless heart rate monitoring system was successfully fabricated based on the PVDF/ZnO nanoneedle hybrid film. The nanoneedle structure of ZnO with large aspect ratio and hexagonal vertical grown pyramid form could lower the elastic modulus of the hybrid film compared to the rod-like ZnO. Due to its high permittivity, low polarization response time and outstanding durability, the hybrid film can be applied for a real-time pressure sensor to monitor the heart rate. Notably, the lowest detectable pressure of the hybrid film was as small as 4 Pa. Furthermore, the reduced graphene oxide (rGO) electrode-based Bluetooth antenna attained high peak gain (2.70 dBi) and radiation efficiency (78.38%), which was applicable to be used as an omnidirectional antenna to

transmit wireless signal to the smart phone. Interestingly, the received wireless heart beat signal within a distance of 8 m was more sensitively measured on the radial artery than carotid artery without distortion and time delay, and it had a similar oscillation in comparison with the wire pressure sensor. This approach offers a valuable and promising tool for producing the commercial and continuous wireless pressure sensor for use in routine biomedical research and critical healthcare. Lastly, a bass frequency response enhanced flexible PVDF based thin film acoustic actuator was successfully fabricated. High concentration of urchin-like ZnO was embedded in PVDF matrix, enhancing the  $\beta$  phase content and the dielectric property of the composite thin film. ZnO acted as a nucleation agent for the crystallization of PVDF. A chemical vapor deposition (CVD) grown graphene was used as electrodes, enabling high electron mobility for the distortion free acoustic signals. The frequency response of the fabricated acoustic actuator was studied as a function of the film thickness and filler content. The optimized film had the thickness of 80  $\mu\text{m}$  with 30 wt% filler content, and showed 72% and 42 % frequency response enhancement in bass and midrange compared to the commercial PVDF, respectively. In addition, the total harmonic distortion decreased 82 % and

74 % in the bass and midrange regions, respectively. Furthermore, the composite film showed a promising potential for microphone applications. Most of all, it is demonstrated that acoustic actuator performance is strongly influenced by degree of PVDF crystalline.

**KEYWORDS:** PVDF; ZnO nanofillers; Hybrid film; Tactile sensor; Acoustic actuator

**STUDENT NUMBER:** 2013–31306

## **List of Abbreviations**

AFM : atomic force microscopy

ANC : active noise cancellation

APS : (3-aminopropyl)trimethoxysilane

CNT : carbon nanotubes

CVD : chemical vapor deposition

DC : direct current

DMF : dimethylformamide

DSC : differential scanning calorimetry

*f*: frequency in free space

FTIR : fourier transform infrared

GO : graphene oxide

H<sub>2</sub>SO<sub>4</sub> : sulfuric acid

H<sub>2</sub>O<sub>2</sub> : hydrogen peroxide

HCl : Hydrochloric acid

ITO : indium tin oxide

MWCNT : multi-walled carbon nanotube

NW: nanowire

PANI : polyaniline

PCB : printed circuit board

PEDOT: poly (3,4-ethylenedioxythiophene)

PET : poly (ethyleneterephthalate)

POM : polarized optical microscopy

PZT : lead zirconate titanate

PPy : polypyrrole

$P_z$ : Piezoelectric effect

PVDF : poly (vinylidene fluoride)

RFID : Radio Frequency Identification

rGO : reduced graphene oxide

RL : return loss

SEM : scanning electron microscope

Si : silicon

TEM : transmission electron microscopy

$t_{rec}$  : recovery times

$t_{res}$  : response times

VSWR : voltage standing wave ratio

wt% : weight content

XPS : X-ray photoelectron spectroscopy

XRD : X-ray diffraction

Zinc Oxide : ZnO

$A_{\alpha}$  : absorbance at  $766\text{ cm}^{-1}$

$A_{\beta}$  : absorbance at  $840\text{ cm}^{-1}$

$\alpha$  : fine structure constant

$\epsilon_r$  : relative permittivity of medium

$\epsilon'$  : permittivity

$\epsilon''$  : loss factor

$F(\beta)$  :  $\beta$  content in the PVDF

$\lambda$  : wavelength

$\lambda_0$  : wavelength in free space.

$\Delta R/R_s$  : sheet resistance change

## List of Figures

**Figure 1.** Molecular depictions of PVDF, an electrostrictive ferroelectric polymer. The  $\beta$  phase (with an all-*Trans* conformation) is responsible for ferroelectricity, whereas the  $\alpha$  phase (with both *Trans* and *Gauche* conformations) promotes para-electricity.

Reprinted with permission. Copyright 2007 Elsevier.

**Figure 2.** (a) Initial state without a mechanical force. (b) Piezoelectric potential when the external force starts to be applied. (c) Piezoelectric and triboelectric charge distribution at full-contact state. (d) Negative piezoelectric and triboelectric generation at separating state. Reprinted with permission. Copyright 2015 Nature Publishing Group.

**Figure 3.** Schematic sketch of the pyroelectric generating mechanism. (a) The diagrams are showing no output without temperature change, (b) the bound charge change caused from the polarization state change and external current flow after contacting hot flow, and (c) cold flow. Reprinted with permission. Copyright 2014 Royal Society of

## Chemistry

**Figure 4.** Unit cell of the wurtzite structure of ZnO. Reprinted with permission. Copyright 2013 Royal Society of Chemistry.

**Figure 5.** Various PVDF based nanocomposites. (a) PVDF/ZnO, (b) PVDF/CoFe<sub>2</sub>O<sub>4</sub>, (c) PVDF/PZT and (d) PVDF/BaTiO<sub>3</sub>. Reprinted with permission. Copyright 2008 Wiley-VCH Verlag GmbH & Co. KGaA, 2012 American Chemical Society and 2016 MDPI AG.

**Figure 6.** Human skin-inspired multifunctional e-skin. Reprinted with permission. Copyright 2015 American Association for the Advancement of Science.

**Figure 7.** (a) Schematic diagram and (b) a photograph of the device consisting of the PVDF/ZnO composite film and rGO electrodes.

**Figure 8.** SEM images and lattice structure of the (a) ZnO nanorods and (b) ZnO nanodisks

**Figure 9.** XRD spectra to investigate the crystal structure of the ZnO nanorods and disks.

**Figure 10.** a) Setup for electrical poling process along the parallel to the film

and b) time dependence of the applied electrical fields.

**Figure 11.** Representative AFM image of the exfoliated GO as a conducting ink for inkjet printing.

**Figure 12.** XPS spectrum with fitted lines of the pristine and rGO solution for C–C, C–O and C=O bonds.

**Figure 13.** a) Deconvoluted XPS spectrum of patterned GO films by repeat inkjet printing for 30 passes (top image) and graphene sheets resulted from the reduction procedure (bottom image) in the C1s region. Fit lines are labeled as: C–C, C–O and C=O bonds.

**Figure 14.** FTIR spectra of PVDF film fabricated as part of this work, and a commercially available PVDF film.

**Figure 15.** Polarized optical microscopy image of a) pristine PVDF, b) PVDF/ZnO rods, c) PVDF/ZnO disks.

**Figure 16.** The permittivity and losses of the tactile sensor fabricated with PVDF and different ZnO nanostructures.

**Figure 17.** Schematic illustration of the pressures sensing measurement which consists of a pressure controller, pressure gauge sensor and

computer based resistance analyzing interface.

**Figure 18.** The change in resistance of the pristine PVDF, and the PVDF/ZnO composite films. In response to an applied pressure of 30 Pa, showing the response time.

**Figure 19.** Schematic illustration of (a) current-sensing AFM method and (b) I-V characteristic curve of a pristine ZnO rod.

**Figure 20.** Schematic illustration of (a) current-sensing AFM method and (b) I-V characteristic curve of a ZnO rod with rGO.

**Figure 21.** The change in resistance of the pristine PVDF, and the PVDF/ZnO composite films. Testing the minimum pressure level of the films at 20°C.

**Figure 22.** The response times of the PVDF film, the ZnO nanodisk/PVDF film, and the PVDF/ZnO nanorod with various pressures.

**Figure 23.** The recovery times of the PVDF film, the ZnO nanodisk/PVDF film, and the PVDF/ZnO nanorod with various pressures.

**Figure 24.** Change in resistance of PVDF/ZnO nanorod composite film with three different electrodes by applied various pressure.

**Figure 25.** (a) The spatial variation in the change in resistance. The effective area of fabricated device are  $6 \times 6 \text{ cm}^2$ . (b) The PVDF/ZnO nanorod film exhibited a higher pressure sensitivity than (c) the PVDF/ZnO nanodisk film. The film was divided into 144 regions ( $0.5 \times 0.5 \text{ cm}^2$ ) and Pt weights were used to apply a pressure of 30 Pa at each division, one at a time.

**Figure 26.** The output resistance of the PVDF/ZnO nanorod device at various temperatures, 20, 70, and  $120^\circ\text{C}$ , under constant pressure of 30 Pa in the center of device.

**Figure 27.** The response time of PVDF/ZnO nanorod film at the different pressures with various temperatures.

**Figure 28.** The recovery time of PVDF/ZnO nanorod film to the different pressures at various temperatures.

**Figure 29.** (a) The spatial variation of recovery time distribution by milliseconds. (b) . The fabricated PVDF/ZnO rod based film (effective area of  $6 \times 6 \text{ cm}^2$ ) was divided into 144 regions ( $0.5 \times 0.5 \text{ cm}^2$ ) and  $70^\circ\text{C}$  of Pt weights were used to apply a pressure of 30 Pa at each

division, one region at a time, and it shows that 94 % of reliable uniformity by visual color distribution for recovery time of 679~682 ms which represents surface temperature of 70°C.

**Figure 30.** The relationship between external pressure and the temperature of the object placed on the device to induce a pressure response. (a) The change in the resistance and recovery time. (b) Pseudocolor plots showing the applied pressure on the PVDF/ZnO nanorod film.

**Figure 31.** The relationship between external pressure and the temperature of the object placed on the device to induce a pressure response. (a) The response to impact of a droplet with an unknown temperature. (b) The recovery time shows that the temperatures of the droplets were 20°C and 80°C, and the pressure was 90 Pa.

**Figure 32.** . Low and high magnification of SEM images for ZnO (a) nanorod and (b) nanoneedle.

**Figure 33.** XRD spectra to investigate the crystal structure of the ZnO nanorods and nanoneedle.

**Figure 34.** FTIR spectroscopy of pristine PVDF, ZnO nanorod/PVDF and ZnO

nanoneedle/PVDF film.

**Figure 35.** DSC thermograms of pristine PVDF, PVDF/ZnO nanorod and PVDF/ZnO nanoneedle film.

**Figure 36.** The data represented by relative crystallinity as a function of time for three different films (Inset: The plot of  $\ln[-\ln(1 - X_t)]$  versus  $\ln t$  for thermal behavior parameters).

**Figure 37.** Polarized optical microscopy images of pristine PVDF, ZnO nanorod/PVDF and ZnO nanoneedle/PVDF film.

**Figure 38.** Dielectric properties such as permittivity and losses of the hybrid films.

**Figure 39.** Photograph of wearable and wireless pressure sensor for heart rate monitoring.

**Figure 40.** Schematic diagram of the pressure sensor using free standing ZnO/PVDF hybrid film between rGO electrodes.

**Figure 41.** The I-V characteristic curve of the hybrid device that rectifying behaviour of Schottky contact under compressive strain. The insets show a  $\log I$  vs  $V$  plot and schematic illustration of forward bias

when pressure is applied.

**Figure 42.** Energy diagrams of rGO/ZnO junction a) at equilibrium and b) under forward bias.

**Figure 43.** Fabrication of rGO-based Bluetooth antenna pattern on PCB board via screen printing and (e) photograph of the Bluetooth transmitter with rGO-based antenna to transmit inputted pulse signal to the smart phone.

**Figure 44.** (a) XPS spectrum in the C 1s region and (b) Raman spectra of the exfoliated GO and rGO electrode for ZnO/PVDF hybrid film-based pressure sensor..

**Figure 45.** (a) The return loss curve of rGO and gold pattern-based Bluetooth antenna. (b) The radiation 3D pattern of rGO pattern-based Bluetooth antenna.

**Figure 46.** Minimum pressure detection limits and response time of ZnO nanoneedle/PVDF hybrid films as a function of film thickness.

**Figure 47.** The change in resistance of pristine PVDF, ZnO rod/PVDF and ZnO needle/PVDF hybrid film-based pressure sensor according to

the applied pressure of (a) 10 Pa, (b) 25 Pa and (c) 50 Pa.

**Figure 48.** The sensitivity of three different pressure sensors with pristine PVDF, ZnO rod and ZnO needle.

**Figure 49.** Multiple-cycle test of ZnO needle/PVDF film-based pressure sensor with repeated loading-unloading of pressure in the range of 5, 15 and 30 Pa.

**Figure 50.** Resistance changes of ZnO needle/PVDF film-based pressure sensor with different curvature radius under constant applied pressure, 5 Pa.

**Figure 51.** Aging bending cycle test of ZnO needle/PVDF film-based pressure sensor under constant applied pressure of 5 Pa.

**Figure 52.** High magnification of SEM images and the discrimination of strain field under identical applied force for ZnO (a) nanorod and (b) nanoneedle.

**Figure 53.** The difference in the electrical resistance of ZnO needle/PVDF film-based wireless pressure sensor as a function of time for measuring the pulse on the (a) carotid artery and the (b) radial artery

of a human object. For the normal pulse, the heart rate was recorded as 88 bpm for 10 s, and 121 bpm after exercise.

**Figure 54.** Comparing measured difference in the electrical resistance of pulse signal that received by wire and wireless sensor using ZnO needle/PVDF film..

**Figure 55.** The sensor patched on wrist and the changing of pulse was monitored during cycle pedaling, and the speed of pedaling was maintained *ca.* 17 km/h for 45 s.

**Figure 56.** The respond time and RSSI of the wireless pressure sensor according to the distance between Bluetooth transmitter and smartphone.

**Figure 57.** Low and high magnification of SEM images for the fabricated (a) urchin-like (b) rod-like ZnO.

**Figure 58.** XRD patterns to investigate the crystal structure of the ZnO nanofillers.

**Figure 59.** (a) SEM image of ZnO rod power, and several crystal plan sketch of ZnO (b and c).

**Figure 60.** Polarized optical microscopy images of (a) Pristine PVDF film, PVDF hybrid films with (b) rod-like ZnO and (c) urchin-like ZnO by isothermally crystallized at 170 °C and maintained for 240 s then cooled down to room temperature to observe the crystal growth morphology.

**Figure 61.** Polarized optical microscopy images of (a) Pristine PVDF film, PVDF hybrid films with (b) rod-like ZnO and (c) urchin-like ZnO by isothermally crystallized at 170 °C and maintained for 240 s then cooled down to room temperature to observe the crystal growth morphology.

**Figure 62.** IR spectrum of pristine PVDF films and ZnO embedded PVDF hybrid films.

**Figure 63.** a) DSC thermograms of pristine PVDF and PVDF/ZnO hybrid films that cooled from 190 °C at a cooling rate of 10°C/min, b) Relative crystallinity as a function of time, and c) plot of  $\ln[-\ln(1-X_t)]$  versus  $\ln t$  for thermal behavior parameters.

**Figure 64.** (a) Permittivity and loss factor of the fabricated thin films and (b)

Cole-Cole fitting curves by permittivity verse dielectric loss..

**Figure 65.** (a) A schematic illustration of the structural and interphase mechanism with fillers and (b) a photograph of the hybrid thin film loudspeaker consisting of ZnO/PVDF or pristine PVDF with graphene electrodes.

**Figure 66.** (a) HR-TEM (inset: Raman spectrum) and (b) AFM of the fabricated graphene electrode.

**Figure 67.** (a) The frequency responses and (b) total harmonic distortion of different PVDF-based thin film loudspeakers. (c) The frequency response as a function of the film thickness. (d) Relative efficiency of the actuators performance compare to the pristine PVDF acoustic actuator at 100 Hz as a function of the filler content.

**Figure 68.** The frequency responses of PVDF/ZnO urchin-based thin film acoustic actuators with CVD graphene, rGO and CNT electrodes.

**Figure 69.** Initial condition and after-used condition of urchin-like ZnO SEM images (a and b). Comparing c) XRD patterns and d) frequency response.

**Figure 70.** The frequency response as a function of the film thickness.

**Figure 71.** Relative efficiency of the actuators performance compare to the pristine PVDF acoustic actuator at 100 Hz as a function of the filler content.

**Figure 72.** (a) The schematic illustration of measurement setup to investigate the PVDF based acoustic analyzer. The real time change in the resistance of the urchin-like ZnO/PVDF hybrid film as the acoustic analyzer was monitored during speech.

**Figure 73.** (a) The real time change in the resistance of the urchin-like ZnO/PVDF hybrid film as an acoustic analyzer. (b) The phrase “I love sunny days” was tested in different decibels. Each spoken words and phrases show unique I-V peaks as a function of time (c-d).

## List of Tables

- Table 1.** The dielectric parameters of the PVDF film and the two composite ZnO/PVDF films.
- Table 2.** Relevant dielectric parameters at  $10^4$  Hz for PVDF/ZnO nanodisk composite with various filler contents.
- Table 3.** The values of  $n$ ,  $k$ ,  $t_{1/2}$  and dielectric parameters for pristine PVDF and ZnO/PVDF hybrid films.
- Table 4.** VSWR, return loss (RL) and transmitted power values of rGO and gold pattern-based Bluetooth antenna.
- Table 5.** Values of  $n$ ,  $k$  and  $t_{1/2}$  for pristine PVDF and PVDF/ZnO hybrid film.
- Table 6.** The values of  $\beta$  content and dielectric parameters of the commercial, pristine PVDF and ZnO/PVDF hybrid films.

## Table of Contents

|                                                                |             |
|----------------------------------------------------------------|-------------|
| <b>Abstract</b> .....                                          | <b>i</b>    |
| <b>List of Abbreviations</b> .....                             | <b>v</b>    |
| <b>List of Figures</b> .....                                   | <b>viii</b> |
| <b>List of Tables</b> .....                                    | <b>xxi</b>  |
| <b>Table of Contents</b> .....                                 | <b>xxii</b> |
| <br>                                                           |             |
| <b>1. INTRODUCTION</b> .....                                   | <b>1</b>    |
| <b>1.1. Background</b> .....                                   | <b>1</b>    |
| 1.1.1. Poly(vinylidene fluoride) .....                         | 1           |
| 1.1.1.1. Piezoelectricity .....                                | 3           |
| 1.1.1.2. Pyroelectricity.....                                  | 5           |
| 1.1.2. Zinc oxide .....                                        | 7           |
| 1.1.3. Zinc oxide/ poly(vinylidene fluoride) hybrid film ..... | 9           |
| 1.1.4. Application fields .....                                | 11          |
| 1.1.4.1. Tactile sensor.....                                   | 11          |
| 1.1.4.2. Acoustic actuator .....                               | 15          |
| <b>1.2. Objectives and Outlines</b> .....                      | <b>16</b>   |
| 1.2.1. Objectives .....                                        | 16          |
| 1.2.2. Outlines .....                                          | 16          |
| <br>                                                           |             |
| <b>2. EXPERIMENTAL DETAILS</b> .....                           | <b>21</b>   |

|                                                                                                                             |            |
|-----------------------------------------------------------------------------------------------------------------------------|------------|
| <b>2.1. Fabrication of PVDF Thin Film with Free-standing Rod-like ZnO for Pressure and Temperature Gauge Sensing.....</b>   | <b>21</b>  |
| 2.1.1. Fabrication of PVDF thin film with free-standing ZnO rod.....                                                        | 21         |
| 2.1.2. Bifunctional tactile sensor for pressure and temperature .....                                                       | 25         |
| <b>2.2. Fabrication of PVDF Thin Film with Free-standing Needle-like ZnO for Wireless Heart Rate Monitoring System.....</b> | <b>26</b>  |
| 2.2.1. Fabrication of PVDF thin film with free-standing needle-like ZnO rod.....                                            | 26         |
| 2.2.2. Wearable and wireless heart rate system .....                                                                        | 28         |
| <b>2.3. Fabrication of PVDF Thin Film with Urchin-like ZnO for Acoustic Actuator .....</b>                                  | <b>30</b>  |
| 2.3.1. Fabrication of PVDF thin film with urchin-like ZnO.....                                                              | 30         |
| 2.3.2. Acoustic generator and receiver .....                                                                                | 33         |
| <b>3. RESULTS AND DISCUSSION.....</b>                                                                                       | <b>34</b>  |
| <b>3.1. Fabrication of PVDF Thin Film with Free-standing Rod-like ZnO for Pressure and Temperature Gauge Sensing.....</b>   | <b>34</b>  |
| 3.1.1. Fabrication of PVDF thin film with free-standing ZnO rod.....                                                        | 34         |
| 3.1.2. Bifunctional tactile sensor for pressure and temperature .....                                                       | 53         |
| <b>3.2. Fabrication of PVDF Thin Film with Free-standing Needle-like ZnO for Wireless Heart Rate Monitoring System.....</b> | <b>75</b>  |
| 3.2.1. Fabrication of PVDF thin film with free-standing needle-like ZnO rod.....                                            | 75         |
| 3.2.2. Wearable and wireless heart rate system .....                                                                        | 86         |
| <b>3.3. Fabrication of PVDF Thin Film with Urchin-like ZnO for Acoustic Actuator .....</b>                                  | <b>113</b> |

|                                                                |            |
|----------------------------------------------------------------|------------|
| 3.3.1. Fabrication of PVDF thin film with urchin-like ZnO..... | 113        |
| 3.3.2. Acoustic generator and receiver .....                   | 128        |
| <b>4. CONCLUSIONS .....</b>                                    | <b>143</b> |
| <b>REFERENCES .....</b>                                        | <b>148</b> |
| <b>국문초록 .....</b>                                              | <b>158</b> |

# 1. INTRODUCTION

## 1.1. Background

### 1.1.1. Poly(vinylidene fluoride)

Among the various piezoelectric materials, poly(vinylidene fluoride) (PVDF) has received considerable attention in the past decade because of its nontoxicity, low cost and density. As a representative semi-crystallin polymer, it has three possible polymorphs such as alpha( $\alpha$ ), beta( $\beta$ ), and gamma( $\gamma$ ) phases according to the chain conformation of trans and gauche linkages.[1-4] The  $\alpha$  phase of PVDF is composed of repeating 1,1-difluoroethyl units joined to CF<sub>2</sub> groups in a *trans-gauche* configuration and  $\beta$  crystalline phase has an *all-trans* conformation, which is a planar zigzag configuration whose CH<sub>2</sub>-CF<sub>2</sub> rocking and asymmetric stretching modes (Figure 1). Especially, the piezoelectric property of PVDF is strongly dependent of its  $\beta$  phase content owing to high net dipole moment originates from the all-trans structure. Therefore, a large effort has been devoted to improve  $\beta$  phase content of PVDF for piezoelectric devices. The  $\beta$  phase enhanced PVDF makes it valuable material for use as sensors and actuators since its strong piezoelectric response and chemical and mechanical durability[5-8]. However, fabricateing fully  $\beta$  phase contained PVDF film is still limited using film drawing process. Therefore, it is still a challenge to use commerical PVDF as an electronic

device matrix.

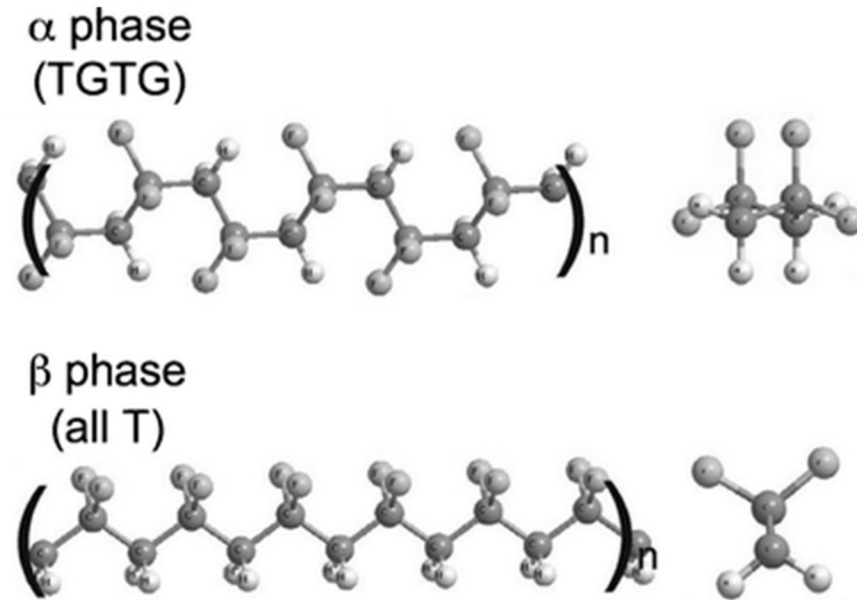


**Figure 1.** Molecular depictions of PVDF, an electrostrictive ferroelectric polymer. The  $\beta$  phase (with an all-*Trans* conformation) is responsible for ferroelectricity, whereas the  $\alpha$  phase (with both *Trans* and *Gauche* conformations) promotes para-electricity. Reprinted with permission. Copyright 2007 Elsevier.

#### 1.1.1.1. Piezoelectricity

By the simplest and broadest definition, a piezoelectric material is one that undergoes a change in electrical polarization in response to mechanical stress. [9,10]. Piezoelectricity is a characteristic of materials that can transfer kinetic energy to electrical energy. In other words, an input of mechanical energy will produce an electrical polarization. The reverse piezoelectricity also can be occurred by applying an electrical polarization will cause changes in dimensions. The piezoelectric effect is understood as the linear electromechanical interaction between the mechanical and the electrical state in crystalline materials with no inversion symmetry (Figure 2). The nature of the piezoelectric effect is closely related to the occurrence of electric dipole moments in solids. The latter may either be induced for ions on crystal lattice sites with asymmetric charge surroundings or may directly be carried by molecular groups. More deeply, piezoelectric materials are a class of low-symmetry materials that can be polarized, in addition to an electric field, also by application of a mechanical stress. The linear relationship between the stress  $\Pi_m$  applied on a piezoelectric material and the resulting charge density  $D_i$  is known as the direct piezoelectric effect and may be written as:

$$D_i = d_{im} \Pi_m$$

where  $d_{im}$  (C/N) are piezoelectric coefficients.  $d$  is a third-rank tensor[11].

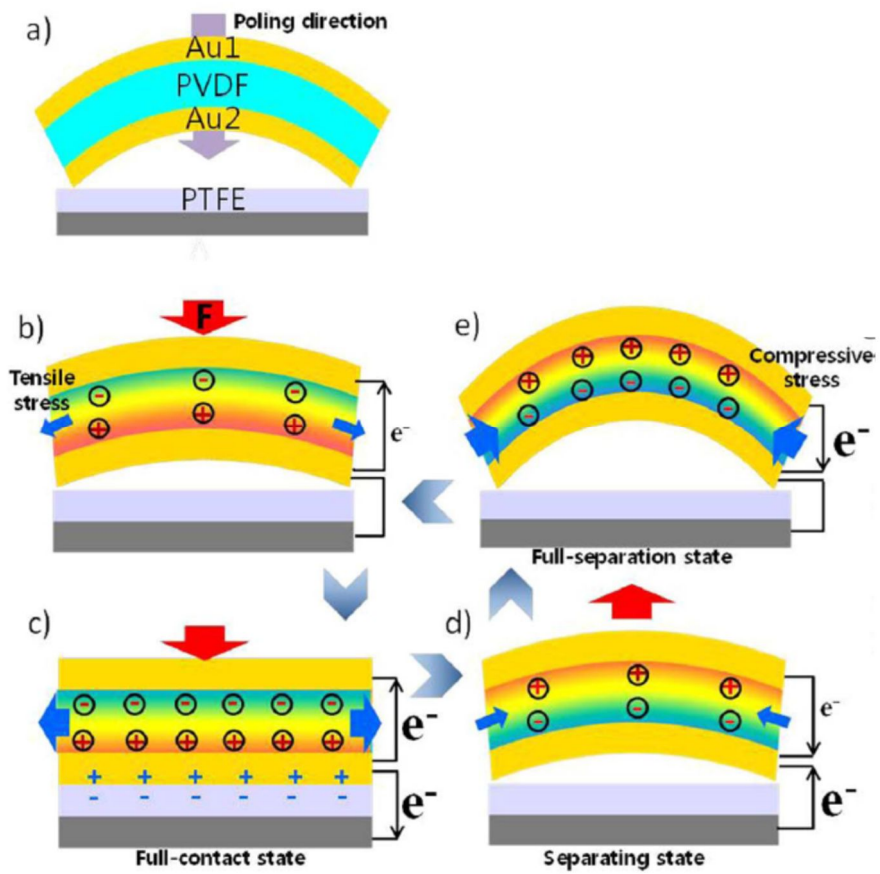


**Figure 2.** (a) Initial state without a mechanical force. (b) Piezoelectric potential when the external force starts to be applied. (c) Piezoelectric and triboelectric charge distribution at full-contact state. (d) Negative piezoelectric and triboelectric generation at separating state. Reprinted with permission. Copyright 2015 Nature Publishing Group.

The piezoelectric effect is a reversible process, in which electrical potential is transformed into the mechanical stress and *vice versa*. Representative piezoelectric materials are quartz, BaTiO<sub>3</sub>, Pb(Zr,Ti)O<sub>3</sub> (PZT) (lead zirconated titanate), zinc oxide (ZnO), PVDF, and so on [12-18]. Although inorganic materials exhibit large piezoelectric moduli, the use of these materials as thin film applications is limited because of brittleness and difficulty in shaping these materials to complex and flexible structures. Thus, organic piezoelectric materials such as PVDF have received considerable attention.

#### 1.1.1.2. Pyroelectricity

Polar materials possess an effective electric dipole moment the absence of an external field. In general, the individual dipoles are randomly oriented in the space. In so-called pyroelectric materials, all dipoles are oriented in the same sense, creating surface charge, which is a measure of the macroscopic spontaneous polarization (Figure 3). Simply, pyroelectricity is the ability of certain materials to generate a temporary voltage when they are heated or cooled [19]. The change in temperature modifies the positions of the atoms slightly within the crystal structure, such that the polarization of the material changes. This polarization change gives rise to a voltage across the crystal.

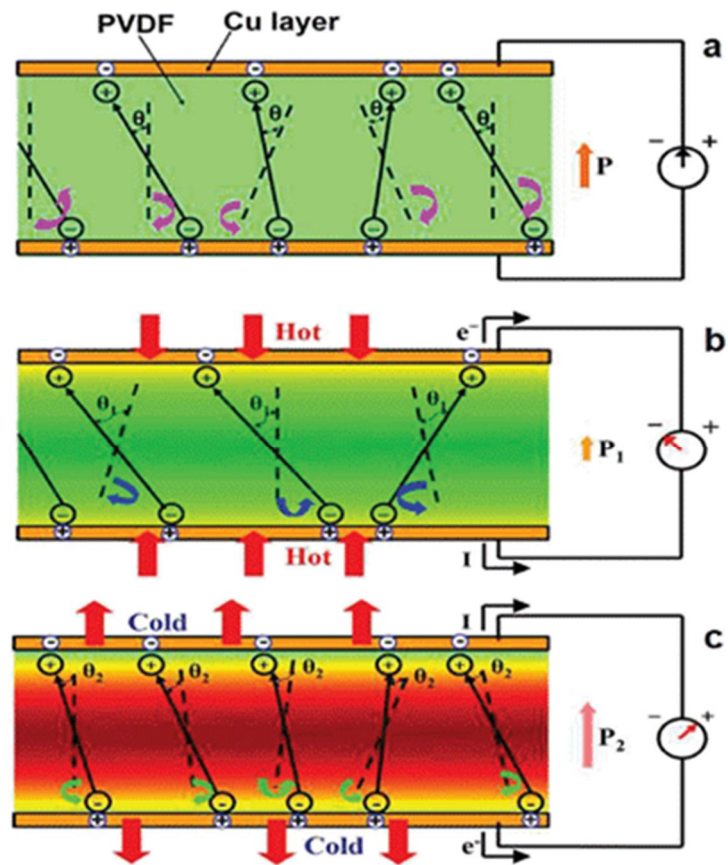


**Figure 3.** Schematic sketch of the pyroelectric generating mechanism. (a) The diagrams are showing no output without temperature change, (b) the bound charge change caused from the polarization state change and external current flow after contacting hot flow, and (c) cold flow. Reprinted with permission. Copyright 2014 Royal Society of Chemistry.

### 1.1.2. Zinc oxide

ZnO is a wide-bandgap semiconductor of the II-VI semiconductor group. The native doping of the semiconductor due to oxygen vacancies or zinc interstitials is n-type [20-26]. This semiconductor has several favorable properties, including good transparency, high electron mobility, wide bandgap, strong room-temperature luminescence and dielectric constant. Zinc oxide crystallizes in two main forms, hexagonal wurtzite and cubic zincblende (Figure 4). The wurtzite structure is most stable at ambient conditions and thus most common. The zinc blende form can be stabilized by growing ZnO on substrates with cubic lattice structure. Moreover, ZnO can be created high piezoelectric potential by the relative displacement of the  $Zn^{2+}$  cations with respect to the  $O^{2-}$  anions, resultant in the wurtzite crystal structure. Therefore, these ionic charges can freely move and recombine with each other as releasing the strain [27-45].

Among the known one-dimensional (1D) nanomaterials, ZnO has three key advantages. First, it exhibits both semiconducting and piezoelectric properties that can form the basis for electromechanically coupled sensors and transducers. Second, ZnO is relatively biosafe and biocompatible, and it can be used for biomedical applications with little toxicity. Finally, ZnO exhibits the most diverse and abundant so far, such as nanowires, nanobelts, nanosprings,

nanorings, nanobows, and nanohelices

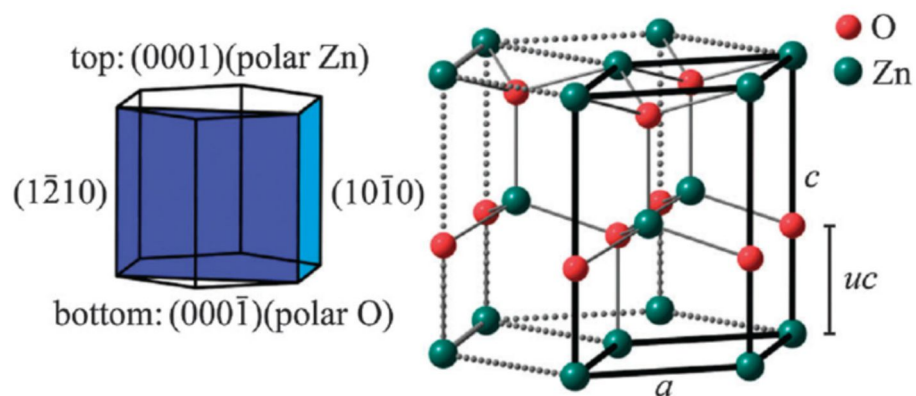


**Figure 4.** Unit cell of the wurtzite structure of ZnO. Reprinted with permission. Copyright 2013 Royal Society of Chemistry.

### 1.1.3. Zinc oxide/poly(vinylidene) fluoride hybrid film

As a representative piezoelectric material, PVDF and its copolymers have been widely used owing to their light weight, non-toxicity and ease of processing. In general, the piezoelectricity refers to the ability of a material to generate a piezoelectric potential in response to an external force, and thus the enhanced dielectric property like permittivity is a key factor for improving the sensitivity of PVDF-based pressure sensors. For this reason, inorganic fillers with high dielectric constants including TiO<sub>2</sub>, BaTiO<sub>3</sub>, PZT and ZnO have been dispersed into the PVDF matrix (Figure 5). Martins *et al.* loaded dielectric BaTiO<sub>3</sub> nanoparticle in PVDF thin film increasing dielectric permittivity, resulting from the increased  $\beta$  phase content [14]. In spite of the loading of dielectric fillers increased the piezoelectric effect of the composite PVDF-based film, they suffer from the low dispersity of fillers in the matrix. Namely, incorporating a high concentration of nanofillers to the matrix caused the particle–particle aggregation that result in the reduction of the dielectric permittivity.

The enhanced permittivity, which is related to the polarization and dipole moment of PVDF, is key factor for improving the piezoelectric and pyroelectric properties of PVDF. For this reason, the semiconductor ZnO is of interest, as it may increase the piezoelectric response, is thermally stable, and

may increase the permittivity of PVDF.

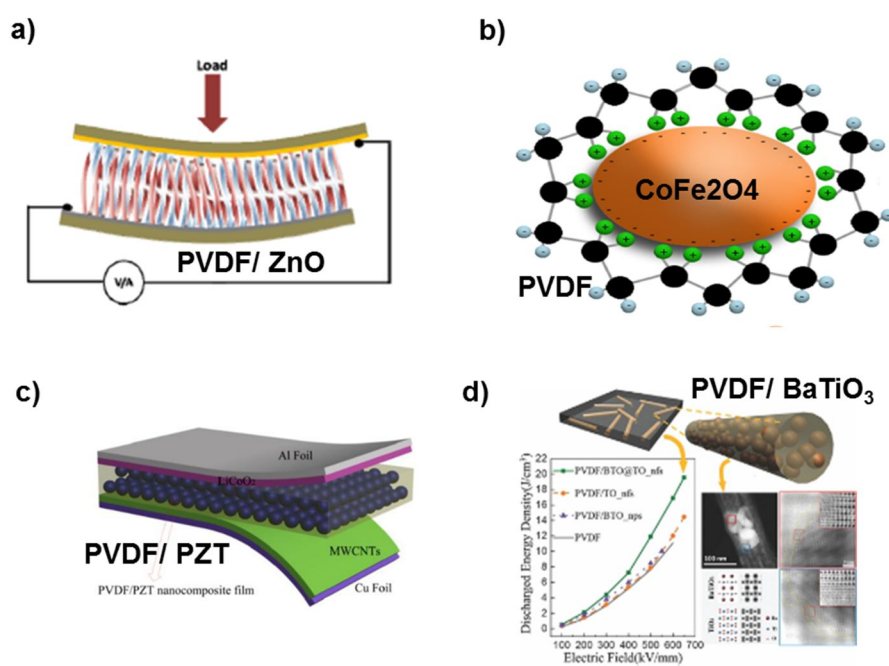


**Figure 5.** Various PVDF based nanocomposites. (a) PVDF/ZnO, (b) PVDF/CoFe<sub>2</sub>O<sub>4</sub>, (c) PVDF/PZT and (d) PVDF/BaTiO<sub>3</sub>. Reprinted with permission. Copyright 2008 Wiley-VCH Verlag GmbH & Co. KGaA, 2012 American Chemical Society and 2016 MDPI AG.

#### **1.1.4. Application fields**

##### 1.1.4.1. Tactile sensor

Electronic skin (e-skin) mimics some of the functionality of human skin, aiming to provide sensory responses to mechanical, thermal, chemical, biological and optical stimuli (Figure 6). Therefore, multifunctional electronic sensors are of great interest for medical and industrial applications. In particular, thin-film systems have been investigated for use in sensor devices, due to the convenient, low-cost processing techniques and flexibility. Moreover, the development of a flexible thin-film device that can replace the epidermis has important applications in the treatment of injuries. Much effort has been devoted to enhancing the performance of pressure-sensing films. Integrated, strain-gauge sensors have been reported by Kahp-Yang Shu *et al.* that could detect pressure, shear and torsion [46]. In contrast, relatively little attention has been paid to sensing of combined external stimuli in a single device, such as sensing mechanical strain and temperature. It is not straightforward to design a system that can discriminate among different stimuli, because the fabrication of such multifunctional sensors typically involves integration of a number of organic and inorganic devices using hybrid matrix arrays and circuit elements, which involves complex, expensive processes [47-61]. Thus, it is still challenging to realize a sensor that enable to

detect multiple stimuli accurately and simultaneously.

To date, much effort has been devoted to investigating the piezoelectric and pyroelectric properties of thin films for fabrication of multifunctional sensors. The piezoelectric and pyroelectric properties of thin films enable fabrication of multifunctional sensors. Reverse-piezoelectricity can respond to an applied mechanical displacement by inducing an electric potential and pyroelectricity. Therefore, a hybrid PVDF matrix with a ZnO nanofillers may enable fabrication of a hybrid piezoelectric/pyroelectric sensor. Furthermore, piezoresistive and piezoresistive sensing, which transduces mechanical displacement and temperature signals into an electrical signal, may be a valuable and simple monitoring method for small structures [62-67]. In particular, a change in the electron mobility or resistance can be measured using a transistor structure

A wearable and wireless pressure sensor for real-time remote monitoring the physiological variables such as heartbeat rate, acceleration, and motion has recently attracted a great deal of interest in routine biomedical research and critical healthcare. The various promising strategies to develop highly flexible and sensitive pressure sensors in low-pressure regime ( $< 10$  kPa) have been demonstrated, which required the rational design of innovative materials and devices in large area [68-75]. Especially, thin-film systems using a

piezoelectric material have been investigated for use in pressure sensor devices due to the convenient, low-cost processing techniques and flexibility.

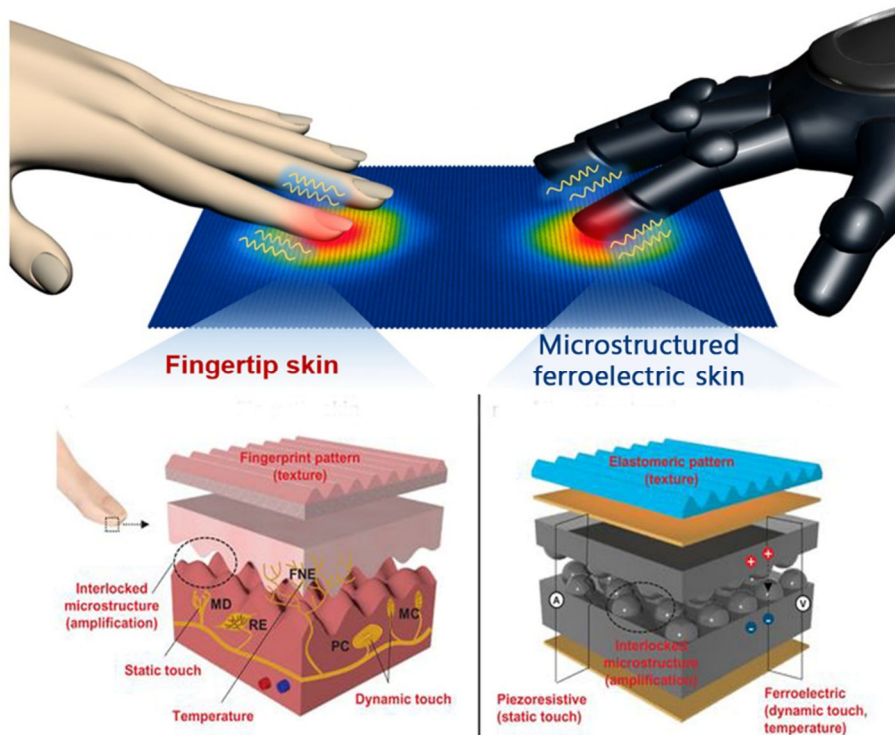


**Figure 6.** Human skin–inspired multifunctional e-skin. Reprinted with permission. Copyright 2015 American Association for the Advancement of Science.

#### 1.1.3.2. Acoustic actuator

Recently, portable devices have attracted great attention. Due to the limited allowed space and weight, all components are obligated to be small, lightweight, as well as power-efficient. Traditionally, electrodynamic loudspeaker, which operates based on the movement of the voice coil motor, have been used in many audio devices. However, its use in small portable devices has been limited due to relatively heavy and thick device structure. Thus, new forms of loudspeaker have been extensively studied as alternative electrodynamic loudspeaker. Among them, the piezoelectric acoustic actuators have received attention as the most remarkable option. Piezoelectric acoustic actuators can be prepared into a film that is thinner than 1 mm, whereas electrodynamic loudspeakers have 3 mm or greater thickness. Also, piezoelectric acoustic actuators are more power-efficient than electrodynamic types due to its high impedance characteristics, generating a large sound pressure at a relatively low operating voltage.

The piezoelectric acoustic actuator is a type of transducers that generates the sound pressure in response to the electrical audio signal inputs, which is in a form of electrical potential. Piezoelectric acoustic actuators operate based on the piezoelectric effect.

## **1.2. Objectives and Outline of the Study**

### **1.2.1. Objectives**

In the preceding section, the importance of PVDF/zinc oxide nanostructure hybrid thin films were introduced from the viewpoint of academic research and practical applications. The aim of this dissertation is to present dielectric characteristics of PVDF thin film depending on different ZnO morphologies as a nanofiller. Furthermore, mechanism underlying the phase of PVDF and ZnO are systematically investigated, and their application fields are also explored, including piezo-, pyro sensor, wireless hearth care system and acoustic actuator.

### **1.2.2. Outline**

This dissertation involves the following subtopics:

- I. Fabrication of PVDF Thin Film with Free-standing Rod-like ZnO for Pressure and Temperature Gauge Sensing
  1. Fabrication of PVDF thin film with free-standing ZnO rod
  2. Bifunctional tactile sensor for pressure and temperature
- II. Fabrication of PVDF Thin Film with Free-standing Needle-like ZnO for Wireless Heart Rate Monitoring System
  1. Fabrication of PVDF thin film with free-standing needle-like ZnO rod
  2. Wearable and wireless heart rate system

### III. Fabrication of PVDF Thin Film with Urchin-like ZnO for Acoustic

#### Actuator

1. Fabrication of PVDF thin film with urchin-like ZnO
2. Acoustic generator and receiver

A detailed outline of the study is as follows:

1. A highly sensitive hybrid bifunctional gauge sensor was fabricated using a PVDF thin film and vertically grown ZnO nanorods. As electrodes, a graphene was utilized which is derived from the vacuum-assisted reduction of GO film by inkjet printing. This is the first experimental demonstration of the detection of two different independent stimuli (i.e., pressure and temperature) simultaneously and in real time. The pressure was inferred from the change in the electrical resistance via the piezoresistance of the material, and the temperature was determined based on the recovery time of the signal. The morphology of the ZnO nanostructures was controlled to maximize the response of the device, and the output signals were monitored while controlling the pressure and temperature to calibrate the device.
2. A novel route toward the fabrication of highly sensitive, wearable and wireless pressure sensor using the ZnO nanoneedle/PVDF hybrid film. This is the first experimental evidence for highly reproducible and durable ZnO/PVDF hybrid film via tailoring the shape and size of ZnO structure. Importantly, needle-like ZnO nanostructures with high aspect ratio and hexagonal vertical grown pyramid form, acted as nucleating agent, allowed for enhanced crystallinity, permittivity and reduced elastic modulus of ZnO/PVDF hybrid film. Furthermore, the reduced graphene oxide (rGO)

with high conductivity was utilized for the electrodes of pressure sensor and Bluetooth antenna using screen printing. Moreover, the changes in resistance as a function of applied pressure, loading/unloading cycle and curvature radius under constant pressure were evaluated. In addition, we applied the ZnO nanoneedle/PVDF hybrid film for a wearable and wireless pressure sensor to real-time monitor the heart rate via smart phone screen.

3. The behavior of a PVDF based thin film acoustic actuator which the performance of every frequency range has been increased by the incorporation of urchin-like ZnO as nanofillers and CVD-grown graphene electrodes. Especially, high dielectric urchin-like ZnO nanofillers have prevented the filler aggregation and allowed the nanospike-to-nanospike current path, while they also acted as a nucleation agent augmenting the  $\beta$  phase content of the fabricated composite film. To investigate the composite film, the crystalline behavior and dielectric permittivity parameters were studied. Furthermore, the fabricated composite film was applied as the active component of a loudspeaker and microphone. In case of the loudspeaker application, the fabricated PVDF/ZnO thin film demonstrated the enhanced bass frequency response and decreased total harmonic distortion compared to other PVDF based thin films. Moreover, the fabricated PVDF/ZnO thin film has shown the first experimental

potential for the application in thin film microphone.

## **2. EXPERIMENTAL DETAILS**

### **2.1. Fabrication of PVDF Thin Film with Free-standing Rod-like ZnO for Pressure and Temperature Gauge Sensing**

#### **2.1.1. Fabrication of PVDF thin film with free-standing ZnO rod**

To fabricate flexible multilayer device as a gauge sensor, a large areal density of ZnO nanorods was embedded in the PVDF on a reduced graphene oxide (rGO)-treated flexible polyethylene terephthalate (PET) thin film. First, exfoliated GO aqueous ink was modified on the flexible PET substrate via inkjet printing, and reduced for use as an electrode [76-79]. The ZnO nanorods were then grown, followed by a hydrothermal treatment.

First of all, the ZnO nanostructures were fabricated using a seed solution zinc acetate ( $\text{Zn}(\text{CH}_3\text{COO})_2$ ) (Sigma–Aldrich) dissolved in ethanol, which was spin-coated onto the rGO-treated PET film. The ZnO nanorods were grown from a mixture of zinc nitrate hexahydrate ( $\text{Zn}(\text{NO}_3)_2 \cdot 6\text{H}_2\text{O}$ ), hexamethylenetetramine (Sigma–Aldrich) and water at 90°C. The morphology of the ZnO nanorods was controlled by varying the time and concentration of the solution of growth precursor. During the early stages of the hydrothermal method, ZnO nucleates spontaneously from the ionized  $\text{Zn}(\text{OH})_4^{2-}$  seed, to form a hexagonal nanostructure in the mixture, which then initiates the growth of one-dimensional (1D) nanorods by increasing the temperature and

concentration. After then, the 20-wt% PVDF (molecular weight of 275,000, determined via gel permeation chromatography) solution which dissolved in a 1:1 mixture of acetone and dimethylformamide (DMF), and was spin-coated onto the ZnO grown film, which then coagulated<sup>28</sup> A poling process was then carried out under a strong constant electric field of 300 kV/cm at 90°C to induce piezoelectricity and pyroelectricity in the PVDF<sup>4</sup>. A top electrode of conductive ink was coated onto the PVDF/ZnO nanorod composite film using inkjet printing.

To fabricate the conductive ink electrode, an aqueous solution GO was synthesized using the Hummers and Offeman method as originally presented by Kovtyukhova and colleagues. Synthesized purified GO suspensions were dispersed in water. Exfoliation of GO was achieved by sonication of the dispersion for 3 h to avoid the nozzle blockage. The obtained brown dispersion was then washed for 5 cycles of centrifugation at 3,000 rpm to remove any unexfoliated graphite oxide. The graphite flakes used in the majority of experiments was purchased from Sigma-Aldrich (Product Number 332461). GO was printed using a commercial office inkjet printer (Canon Pixima IP1300). Poly (ethyleneterephthalate) (PET, 3M) film was used as a substrate for inkjet printing.

For inkjet printing method, the ink cartridge (printer head) was

disassembled and washed several times by ethanol and distilled water after removing all inks. The exfoliated GO in distilled water was injected into the modified cartridge as an alternative ink. Subsequently, the completely sealed ink cartridge was placed in the printer body and prepared to use for further experiments. In addition, the PET film was treated by oxygen plasma in order to modify the surface energies of target substrate (gas flow rate: 20 sccm, power: 100 W, time: 20 s). The complex patterned architectures were designed by computer software in advance (Microsoft PowerPoint 2003). The exfoliated GO solution was printed on the flexible PET film as the designed images using the modified inkjet printer. Subsequently, the printed film was properly cut and located in VDP chamber containing hydrazine and ammonia solution. The graphene sheets patterns were formed immediately at low temperature (90 °C, 1 h).

The X-ray diffraction (XRD) patterns were collected using a MAC Science Co. M18XHF-SRA model and (FTIR) spectrometer (Bomen MB 100, USA) was used. Transmission electron microscopy (TEM) image was taken with a JEOL 6700F and the X-ray photoelectron spectroscopy (XPS) spectra were recorded using Kratos Model AXIS-HS system. Field-emission Scanning electron microscope (FE-SEM) images were acquired with JSM-6700F microscope (JEOL, Tokyo, Japan) at an acceleration voltage of 10 keV, and the

atomic force microscopy (AFM) topography of the GO solution deposited on Si wafer was obtained by a Digital Instrument Nanoscope IIIA from veeco systems in tapping mode using silicon tips with a resonance frequency of of 320 KHz. . Raman spectra were recorded using a LabRAM HR (Horiba, Japan) with 1064-nm laser excitation. Optical micrographs were taken using a Leica DM2500 P. The measurement of electrical resistances was performed with a Keithley 2400 sourcemeter at 25 °C by a four-probe method. The sheet resistance was measured at 10 different locations of graphene sheets based films and calculated as an average value.

### **2.1.2. Bifunctional tactile sensor for pressure and temperature**

To compare the pressure-sensing properties of the PVDF and ZnO/PVDF composite films, pressure stimuli were used, and the performance was measured from the change in the electrical resistance; i.e.,  $\Delta R = R_{\text{loading}} - R_{\text{Unloading}}$ . The assembled device had an overlap area of  $6 \times 6 \text{ cm}^2$ , and was measured with a gradual increase in pressure and temperature.

For the analysis of detailed force responses, a computer-based user interface and a micro pressure sensor (FT-S270, Nano Science Instrument) with nanoscale-controlled stage by piezoelectric stepping positioner (SLC-1730, Nano Science Instrument) were used to apply an external pressure. Moreover, direction of stepper to apply pressure was vertically loaded and unloaded in order to avoid distortion output signals by torsion or shear stress. Analysis of the static contact angles was carried out using a DSA 100 drop shape analysis system (Kruss GmbH). The electrical resistance was measured using a Keithley 2400 source meter at  $25^\circ\text{C}$  using a four-probe method.

## **2.2. Fabrication of PVDF Thin Film with Free-standing Needle-like ZnO for Wireless Heart Rate Monitoring**

### **2.2.1. Fabrication of PVDF thin film with free-standing needle-like ZnO rod**

Zinc acetate was dissolved in 100ml of ethanol as seed solution. It was spin-coated on rGO treated PET, and it placed on 100 °C of oven to be dried for 30 min. After then, ZnO nanorod and nanoneedle were grown in a the 90 °C of mixture solution, 0.05 M hexamethylenetetramine and 0.05 M zinc nitrate hexahydrate and de-ionized water (500 ml), for 3 to 7 h to control the morphology of ZnO nanostructure. The graphite used in the experiments was purchased from Sigma-Aldrich. Polyethylene terephthalate (PET) film, PVDF pellets (molecular weight *ca.* 275,000 by gel permeation chromatography), zinc acetate dihydrate, zinc nitrate hexahydrate, hexamethylenetetramine and ethanol were obtained from Sigma–Aldrich.

PVDF was dissolved in a 1:1 mixture of dimethylformamide (DMF), and acetone. The mixture was solution was stirred at 60 °C for 12 h and dropped onto the substrate that free standing ZnO grown film. After then, it was spin coated at 1,200 rpm for 150 s. The fabricated film was poling under a strong constant electric field at 30 kV/mm at 90 °C.

Unreduced GO was synthesized from natural graphite by a modified

Hummers and Offeman method, and exfoliation of GO was achieved by a sonication method [89-82]. As an electrode for pressure sensor, the exfoliated GO could be printed out precisely onto the PET substrate through screen printing mesh using only a scraper (6,000 rpm), and the patterned architectures were designed by screen printing mesh. The printed GO thin film was located in vapor deposition chamber containing hydrazine solution (1mL). The chamber was sealed and placed in an oven at 90 °C for 1 h. The rGO was also fabricated on top of the ZnO/PVDF hybrid thin film for pressure sensor device. To be applied for the Bluetooth antenna, rGO pattern was printed on the printed circuit board (PCB) of Bluetooth transmitter using rGO conducting ink via screen printing

### **2.2.2. Wearable and wireless heart rate sensor**

For the wireless pressure sensor, the hybrid film was connected on the operational amplifier (op-amp) to amplify the pulse signal. Then, the amplified analog signal was converted to digital via signal analyzer (ATmega128), and the data could be transmitted to the smart phone using the Bluetooth module.

For the analysis of pressure level, a computer-based user interface and a micro pressure sensor (FT-S270, Nano Science Instrument) with nanoscale-controlled stage by piezoelectric stepping positioner (SLC-1730, Nano Science Instrument) were used to apply an constant low pressure, from 1 to 50 Pa on the PVDF and the hybrid film. The films were connected to the Keithley 2612A Source Meter and applied DC voltage of 2.5 V to analyze change of electrical resistance,  $\Delta R$ , by external pressure for real-time. Since the corresponding current of the device is about 1 – 2 nA, which does not give any influence on health problem. Moreover, direction of stepper to apply pressure was vertically loaded and unloaded in order to avoid distortion output signals by torsion or sheer stress because of device design.

High-resolution TEM (HR-TEM) images were taken using a JEOL JEM-3010 instrument. Field-emission scanning electron microscopy (FE-SEM, JEOL JSM-6700F, Japan) and a FTIR spectrometer (Bomem MB 100, USA) were also used. The I-V curves were evaluated by current-sensing atomic force

microscopy (CSAFM, Agilent 7500, USA) at 300 K. Differential scanning calorimetry (DSC, Q1000, TA instruments, USA) was used, and the work function was measured by ultraviolet photoelectron spectroscopy (UPS). Electrical resistances were measured with a Keithley 2400 (USA) source meter at 25°C using the four-probe method. To investigate the crystal structure of the ZnO nanorod and nanoneedle, High resolution X-ray diffraction (HR-XRD, Bruker D8 DISCOVER, Germany) analysis and Polarized optical microscopy (POM, Lv100 microscope, Nikon, Japan) images were carried out. An E5071B ENA RF Network Analyzer from Agilent Technologies was used to characterize the RFID antennas using SMA type connector, and impedance was plotted on a Smith chart by first normalizing to the characteristic impedance of the system (50 ohms). The radiation pattern was measured in the anechoic chamber at the Electromagnetic Wave Technology Institute (Korea).

## **2.3. Fabrication of PVDF Thin Film with Urchin-like ZnO for Acoustic Acuator**

### **2.3.1. Fabrication of PVDF thin film with urchin-like ZnO**

First, an appropriate amount of high purity Zn (purity, 99.99%) was ground in an agate mortar for 20 min. Then, 1 g of powder was loaded on an alumina boat and placed in a 1.2 m long quartz tube furnace. The growth process was divided into three steps. Initially, the furnace purged with Ar gas for 20 min. First, an appropriate amount of high purity Zn (purity, 99.99%) was ground in an agate mortar for 20 min. Then, 1 g of powder was loaded on an alumina boat and placed in a quartz tube furnace. The growth process was divided into three steps. Initially, the furnace purged with Ar gas for 20 min. The furnace was heated to 650 °C in the presence of Ar gas. Soon after the growth temperature is reached, a flow of oxygen (120 sccm) is introduced into the quartz tube and the growth process was maintained for 30 min. On a cooling to room temperature, a white woolly deposit was observed on the alumina boat. On a cooling to room temperature, a white woolly deposit was observed on the alumina boat.

To fabricate CVD graphene as an electrodes, Cu foil (7 x 7 cm<sup>2</sup>) was placed in a quartz tubular furnace and the furnace was vacuumed to 30 mTorr. Then, the furnace was heated to 1000 °C under an 8 sccm flow rate of H<sub>2</sub> gas

at 90 mTorr and maintained for 30 min to maximize the size of Cu domains. To grow graphene on the Cu substrate, a 20 sccm flow of CH<sub>4</sub> gas was injected for 30 min at 560 mTorr. After the growing process, CH<sub>4</sub> gas was shut and cooled to room temperature under H<sub>2</sub> atmosphere. To transfer the graphene, 4 % PMMA solution in anisole was spin coated at 5,000 rpm for 1 min onto the Cu foil. The pristine graphene was isolated after Cu foil was etched in a Cu etchant.

The zinc nanopowder (size *ca.* 250 nm; 99.9%; Nano Technology Inc., South Korea) was used in the fabrication of urchin-like ZnO. Zinc acetate dihydrate, zinc nitrate hexahydrate, hexamethylenetetramine, and ethanol were obtained from Sigma-Aldrich, and they were used in the fabrication of rod ZnO. Gases (H<sub>2</sub>, CH<sub>4</sub>, Ar; 99.99%; Daesung Industrial Gases Co., South Korea), Cu foil (Sigma-Aldrich), and poly(methylmethacrylate) (950 PMMA A4, 4% in anisole, MicroChem Corp., USA) were used in the fabrication of the graphene films. PVDF pellets (molecular weight *ca.* 275,000 by gel permeation chromatography), (3-aminopropyl)trimethoxysilane (APS), and dimethylformamide (DMF) were obtained from Sigma–Aldrich. Commercial PVDF film was purchased from the Films Corporation (South Korea)

Field-emission scanning electron microscopy (FE-SEM) images were taken using JEOL JSM-6700F. Transmission electron microscopy (TEM) images

were acquired with a JEM-2100 (JEOL, Japan). Raman spectra measurement was recorded with LabRAM HR (Horiba, Japan) with 1064 nm laser excitation. Fourier-transform infrared (FT-IR) spectra were measured using FT-IR spectrometer (Bomen MB 100, USA), utilizing universal-ATR mode. Atomic force microscopy (AFM, Nanoscope IIIa, Digital instruments, USA) were used in the tapping mode with silicon tips at a resonance frequency of 330 kHz. Polarized optical microscopy images were carried out by Lv100 microscope, Nikon, Japan. To investigate the crystal structure of the ZnO rod and urchin, high resolution X-ray diffraction (HRXRD, Bruker D8 DISCOVER, Germany) was used.

### 2.3.2. Acoustic generator and receiver

ZnO/PVDF thin film ( $7 \times 7 \text{ cm}^2$ ) was first treated with a 0.5 wt% APS solution for 12 h to reduce hydrophobicity of the PVDF film. The film was dried in a  $60 \text{ }^\circ\text{C}$  oven overnight. Two CVD grown graphene/PMMA films were used to sandwich the ZnO/PVDF film. The PMMA layer was then removed from the graphene by washing the film with acetone several times. The Cu tape was attached on the corner of fabricated thin film speaker and used as contact electrode. The sound signal is connected to an amplifier and it produced time variable voltage (AC electric field) to generate sound wave with attractive and repulsive forces [77]. A dScope Series IIIA (Prism Sound Co., UK) audio analyzer was used to quantify the acoustic actuator performance from 10 Hz to 20 kHz.

The fabricated film speaker is placed in a soundproof chamber to isolate noise and reflection interference. The dynamic microphone, which is connected to an audio analyzer, is placed 10 cm above the fabricated film. The frequency response acoustic output of the film was received by the microphone, and the swept signals were measured by audio analyzer. Additionally, the fabricated film speaker is located in a soundproof chamber to isolate noise and reflection interference as same as speaker test method. The electrical resistance was measured using a Keithley 2400 source meter.

### **3. RESULTS AND DISCUSSION**

#### **3.1. Fabrication of PVDF Thin Film with Free-standing Rod-like ZnO for Pressure and Temperature Gauge Sensing**

##### **3.1.1. Fabrication of PVDF thin film with free-standing ZnO rod**

**Figure 7** show a schematic diagram and photograph of the flexible multilayer device. The ZnO nanorods were then grown, followed by a hydrothermal treatment. A large areal density of ZnO nanorods was embedded in the PVDF on a rGO treated flexible polyethylene terephthalate (PET) thin film. A top electrode of conductive ink was coated onto the PVDF/ZnO nanorods composite film using inkjet printing.

The ZnO nanostructures were fabricated using a seed solution, which was spin-coated onto the rGO-treated PET film. The ZnO nanostructures were grown from a mixture of zinc nitrate hexahydrate and hexamethylenetetramine. FE-SEM images reveal that a high density of ZnO nanorods ( $1.42 \times 10^{10} \text{ cm}^{-2}$ ) and disks were formed (**Figure 8a and b**). Furthermore, HR-TEM images show that the ZnO nanorods and nanodisks had a well resolved single-crystalline wurtzite structure, with a lattice constant of 0.52 nm in the [0001] growth direction [80]. This indicates that they formed a uniform hexagonal crystal structural without crystalline defects (see inset **Figure 8a and b**). The length of the ZnO nanorods was  $\sim 300$  nm, and the diameter was  $\sim 85$  nm; the ZnO

nanodisks were  $\sim 30$  nm in length and  $\sim 100$  nm in diameter. To investigate the crystal structure of the ZnO nanorods and nanodisks, XRD analysis was carried out, as shown in [Figure 9](#). All of the diffraction peaks could be clearly indexed to the hexagonal ZnO with a lattice constant of  $c = 0.5206$  nm, which is in good agreement with that of ZnO along the  $c$ -axis. The prepared ZnO was mixed a PVDF solution, which was then drop casted to form a PVDF/ ZnO mat. The PVDF/ZnO films were drawn at an elevated temperature and poled under a strong constant electric field at 30 kV/mm to transform the  $\alpha$  phase to  $\beta$  phase. The setup for poling process under constant electric fields, the high voltage power supply which is connected in series with the fabricated film and with an oscilloscope for measuring the poling current using an additional resistor in the electrical circuit as shown in [Figure 10a](#). The film is placed between upper and lower aluminum plate and 30 kV/mm was applied along the parallel direction to the film by power supply for 3 min and 5times ([Figure 10b](#)). The measured poling signal as well as a signal which represents the poling voltage are stored in the oscilloscope. Additionally, the temperature was maintained 110 °C during a frequency run.

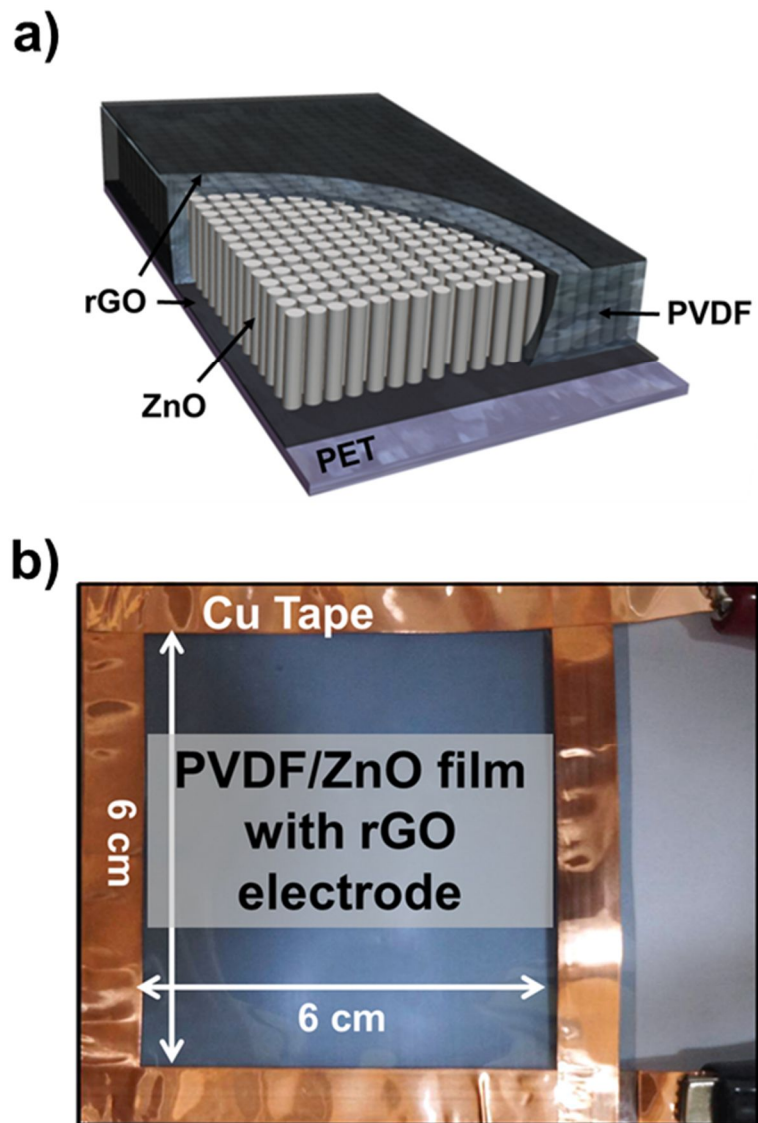


**Figure 7.** (a) Schematic diagram and (b) a photograph of the device consisting of the PVDF/ZnO composite film and rGO electrodes.

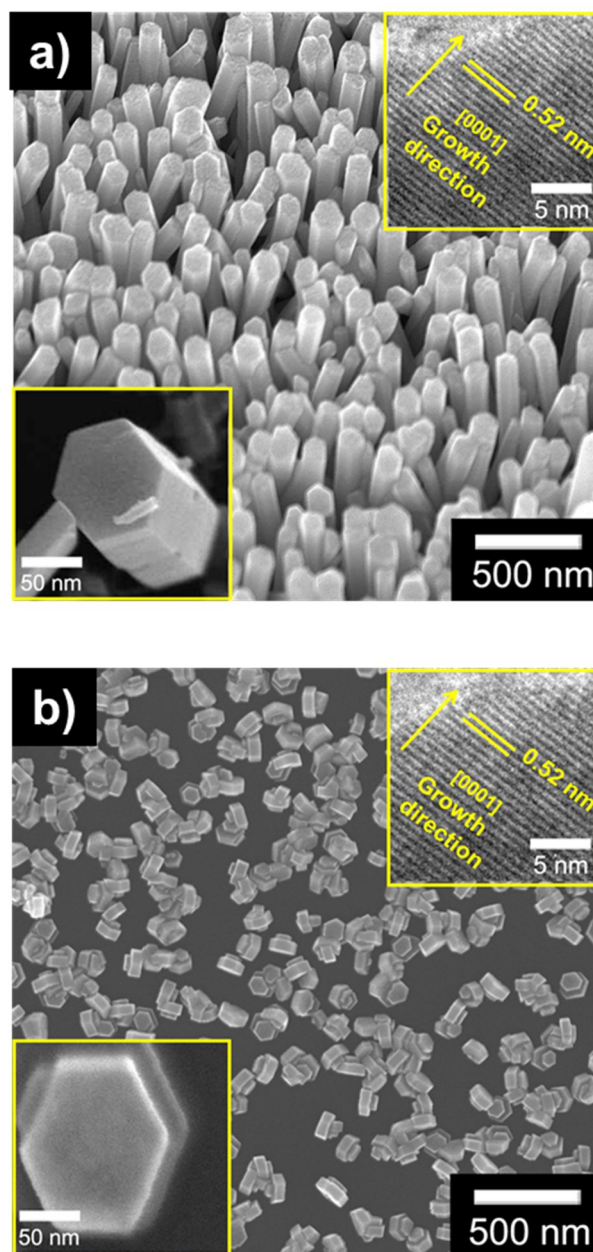


**Figure 8.** SEM images and lattice structure of the (a) ZnO nanorods and (b) ZnO nanodisks

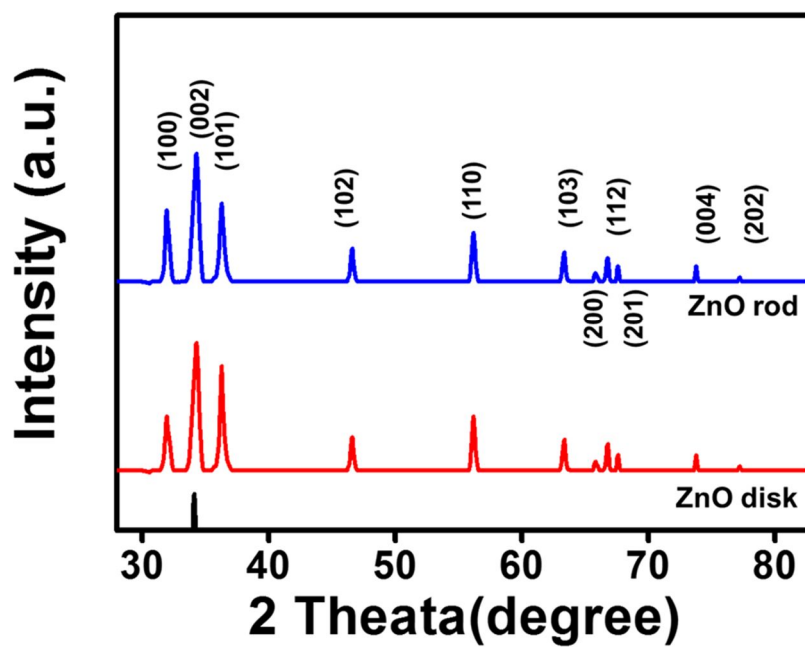


**Figure 9.** XRD spectra to investigate the crystal structure of the ZnO nanorods and disks.

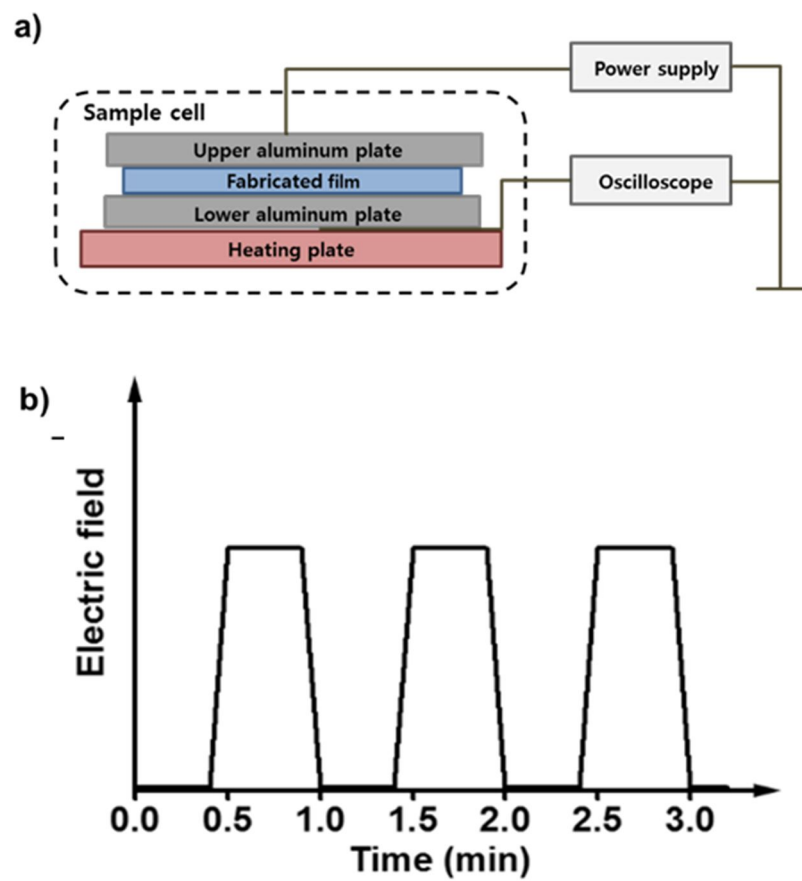


**Figure 10.** a) Setup for electrical poling process along the parallel to the film and b) time dependence of the applied electrical fields.

**Figure 11** shows an AFM image of the fabricated GO ink, which was a few microns thick, and was composed of 2–3-nm-thick bilayers, as well as some multilayers (>3 nm). To demonstrate the reduction of GO solution to graphene, XPS and Raman spectroscopy analysis were carried out. **Figure 12** shows deconvoluted C 1s XPS spectra of the inkjet-printed GO and the reduced GO (rGO) sheets [81]. The C 1s signal of GO has three main components: the C=C and C–C bond vibrations in the aromatic rings (285.0 eV), C–O (286.5 eV) in epoxy or hydroxyl groups, and C=O (288.5 eV) peaks originating from carbonyl and carboxyl groups. The ratio  $I_{C-O}/I_{C-C}$  decreased from 1.1440 (GO) to 0.2432 (rGO). In addition, a Raman spectrum of the printed rGO sheets on the substrate film is shown in **Figure 13**. The Raman spectra of rGO clearly exhibited the characteristic peaks of the D band ( $\sim 1350\text{ cm}^{-1}$ ), which indicate the typical defects ascribed to structural edge effects, such as epoxides covalently bonded to the base plane, the G band ( $\sim 1580\text{ cm}^{-1}$ ), which indicates a graphite carbon structure, and the ration of  $I_D/I_G$  was 0.77.

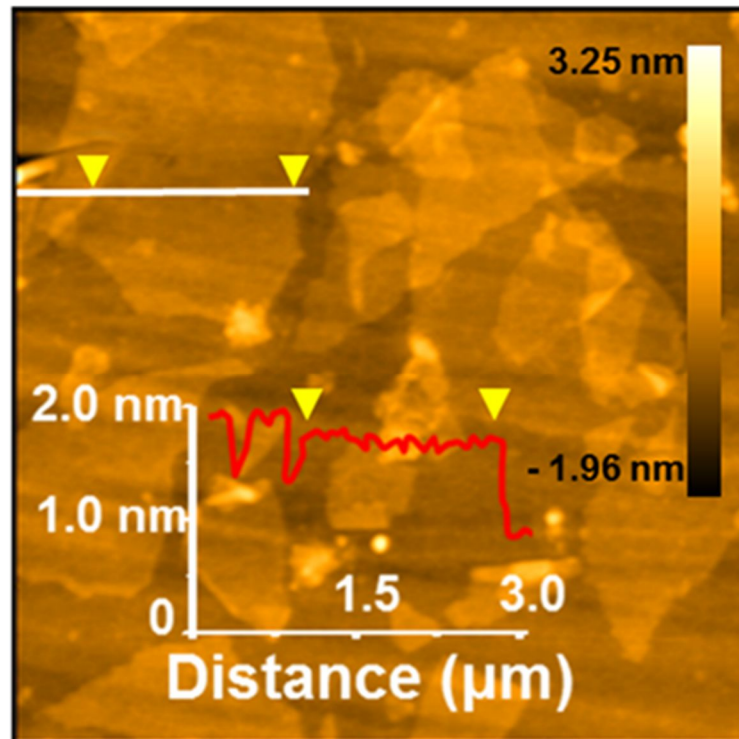


**Figure 11.** Representative AFM image of the exfoliated GO as a conducting ink for inkjet printing.

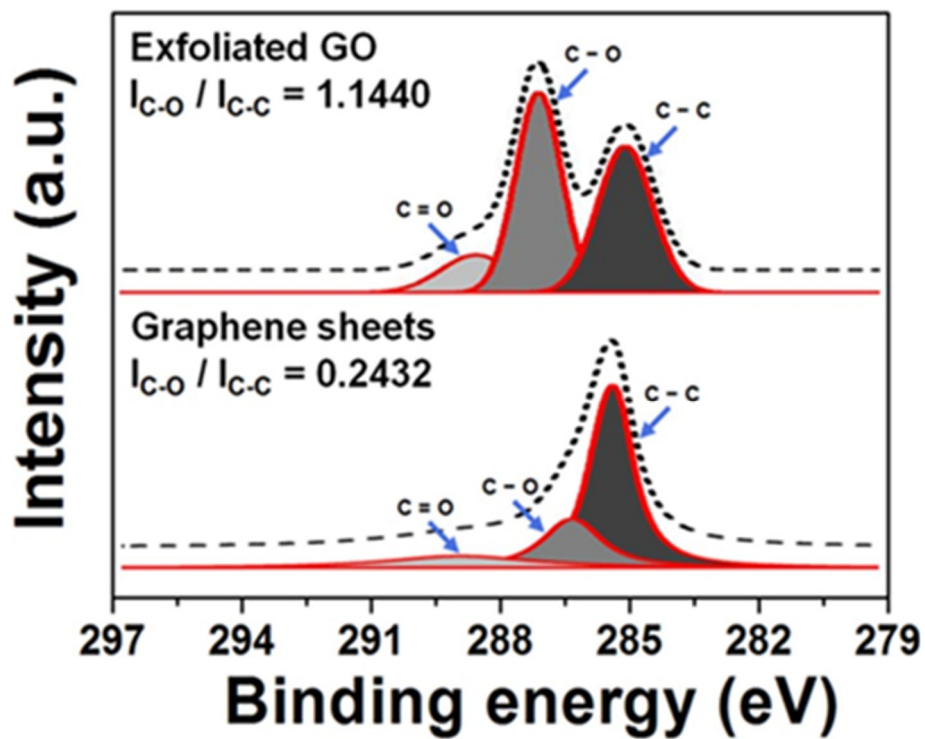


**Figure 12.** XPS spectrum with fitted lines of the pristine and rGO solution for C–C, C–O and C=O bonds.

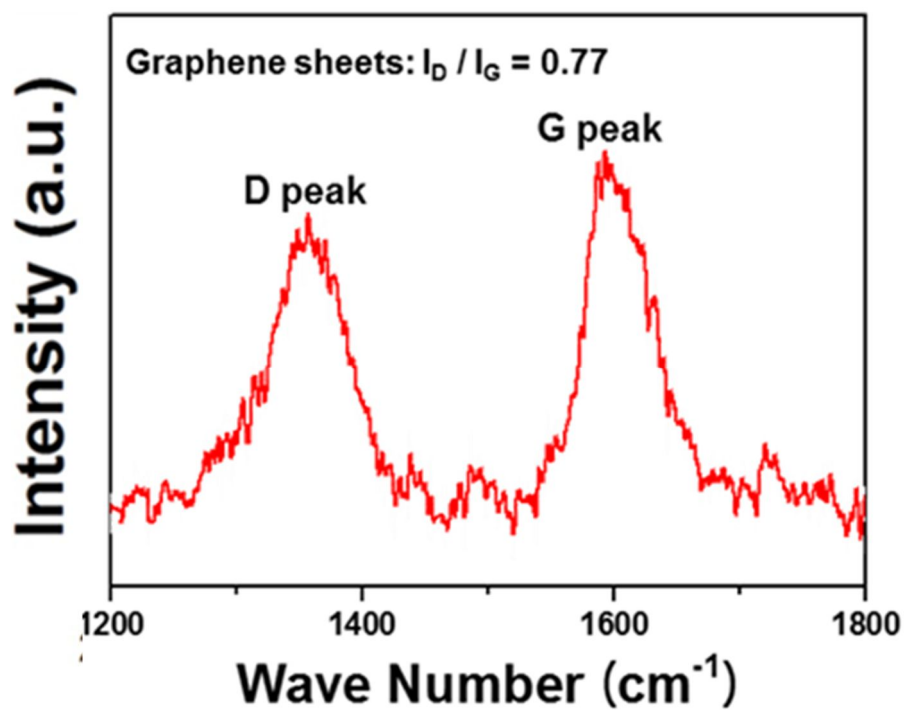


**Figure 13.** a) Deconvoluted XPS spectrum of patterned GO films by repeat inkjet printing for 30 passes (top image) and graphene sheets resulted from the reduction procedure (bottom image) in the C1s region. Fit lines are labeled as: C–C, C–O and C=O bonds.

The piezoelectric and pyroelectric properties of PVDF are strongly dependent on the  $\beta$ -phase content, owing to large net dipole moment, which originates from the all-trans structure<sup>4,34</sup>. Therefore, FTIR spectroscopy was carried out to investigate the strong dielectric potential, based on the ratio of the  $\alpha$  and  $\beta$  phases ( $I_\beta/I_\alpha$ ), and the fraction of the  $\beta$  phase, as shown in **Figure 14**. Assuming that the IR absorption follows the Beer-Lambert law,  $\beta$  content in the PVDF can be measured from [82-83]:

$$F(\beta) = \frac{X_\beta}{X_\alpha + X_\beta} = \frac{A_\beta}{(K_\alpha/K_\beta)A_\alpha + A_\beta}$$

where  $A_\alpha$  and  $A_\beta$  are the absorbance at 766 and 840  $\text{cm}^{-1}$ , respectively, and  $K_\alpha = 6.1 \times 10^4 \text{ cm}^2/\text{mol}$  and  $K_\beta = 7.7 \times 10^4 \text{ cm}^2/\text{mol}$  are the absorption coefficients of  $\alpha$  and  $\beta$  phases at the respective wavenumbers<sup>4</sup>. The PVDF thin film exhibited  $I_\beta/I_\alpha = 2.33$ , which corresponds to an 85%  $\beta$  phase. (For comparison, commercially available PVDF exhibited  $I_\beta/I_\alpha = 1.29$ , which corresponds to a 73%  $\beta$  phase content.)

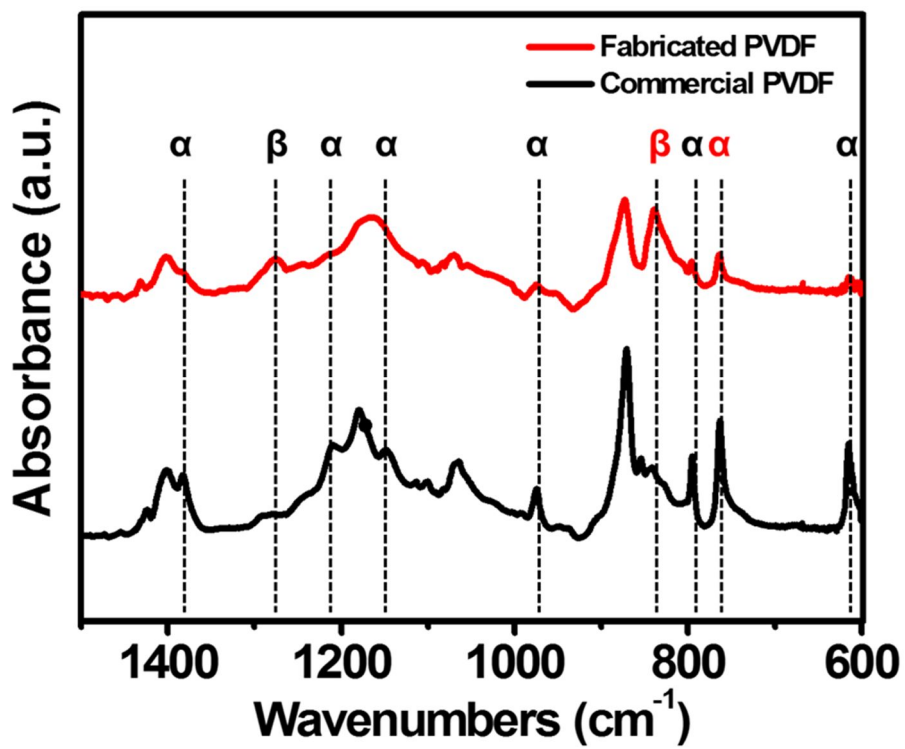


**Figure 14.** FTIR spectra of PVDF film fabricated as part of this work, and a commercially available PVDF film.

Generally, PVDF with a high  $\beta$  phase content exhibits enhanced piezoelectric and pyroelectric responses, due to fact that the dipoles are aligned. The polymer PVDF and semi-conductor ZnO are one of representative dielectric materials which is a substance that inducing electricity by dielectric polarization under electric fields. Especially, the considerable matter of ZnO in our experiment is behavior as role of fillers in the PVDF, whereas matter of conductivity since it is not modified as a transistor. In our previous paper, we reported the function of high permittivity nanofillers for PVDF. As presented [figure 14](#) in the manuscript, it is denoted that ZnO enhanced the crystallinity of PVDF  $\beta$  phase Also, [Figure 15](#) shows that observed POM of the crystal growth of PVDF with various ZnO fillers. All samples were isothermally crystallized at 170 °C and maintained for 240 s, and it cooled down to observe crystal growth morphology. During poling process of film, high external voltage was applied on the film and polarized ZnO induced  $\beta$  phase of PVDF. Thus, regardless of ZnO morphology, it is clarified that ZnO acts as nuclei for PVDF crystallization. However, the sensitivity of detecting pressure capability showed difference because of aspect ratio of ZnO rods and disks. Since free-standing ZnO rod had large aspect ratio (AR = 3.5) than disk (AR = 0.3), polarization at the each upper and lower terminals are easily occurred by applied vertical pressure<sup>2</sup>. Considering these results, ZnO improves

permittivity of PVDF, thus enhanced PVDF with ZnO rod enable to fabricate a highly sensitive tactile sensor. Therefore, we may expect favorable permittivity and losses of sensors fabricated using various ZnO and PVDF thin films. The dielectric properties of PVDF with the embedded ZnO nanorods can be estimated using the Havriliak-Negami and Fourier transfer relationship; i.e. [84]:

$$\varepsilon^* = \varepsilon' + i\varepsilon'' = \varepsilon_\infty + \frac{\Delta\varepsilon}{\{1+(i\omega\lambda)^{1-\alpha}\}^\beta},$$

Where  $\varepsilon'$  is the dielectric constant,  $\varepsilon''$  is the dielectric loss; the permittivity is therefore given by:

$$\Delta\varepsilon = \varepsilon_S - \varepsilon_\infty$$

where  $\varepsilon_S$  is the static permittivity (i.e., when  $\lim_{\omega \rightarrow 0} \varepsilon^*(\omega)$ ), and  $\varepsilon_\infty$  is the high-frequency permittivity (i.e., when  $\lim_{\omega \rightarrow \infty} \varepsilon^*(\omega)$ ).

The measured permittivity of the samples are listed in [Figure 16](#) and [Table 1](#). In general the permittivity of a dielectric is larger at lower frequencies than at higher frequencies, and embedding the ZnO in the PVDF significantly increased the dielectric constant. In particular, the ZnO nanorods possessed a greater dielectric constant than the ZnO disks, which is attributable to the larger aspect ratio of the ZnO nanorods, which resulted in a larger energy barrier. The relaxation time  $\lambda$  is related to the gradient of the loss factor that is associated with the interfacial polarization response of the dielectric material.

The relaxation time is given by:

$$\lambda = \frac{1}{2\pi f_{max}},$$

where  $f_{max}$  is the frequency of the peaks in the loss spectrum<sup>36</sup>. We find a relaxation time of  $\lambda = 159$  for the PVDF,  $\lambda = 130 \mu\text{s}$  for the ZnO nanodisks, and  $\lambda = 121 \mu\text{s}$  for the ZnO nanorods (see [Table 1](#)). Based on these dielectric parameters, the inclusion of ZnO in the PVDF film significantly increased the permittivity and reduced the polarization response time of the PVDF-based sensor devices. Since ZnO nanorods with PVDF possessed a higher dielectric constant, the concentration of seed solution was controlled to investigate effects of ZnO rods density. Approximately 30 wt% of zinc acetate dissolved seed solution grow  $1.42 \times 10^{10} \text{ cm}^{-2}$ , and 25 and 35 wt% represent  $0.68 \times 10^{10} \text{ cm}^{-2}$  and  $2.54 \times 10^{10} \text{ cm}^{-2}$  of ZnO rods. As a result, 25 wt% of zinc acetate solution sparsely grow ZnO rods compare to 30 wt% of seed solution which result in reduced dielectric properties. Additionally, 35 wt% of seed solution limits dielectric properties of fabricated sample because exceeding density of ZnO rods caused aggregation between rods ([Table 2](#)).

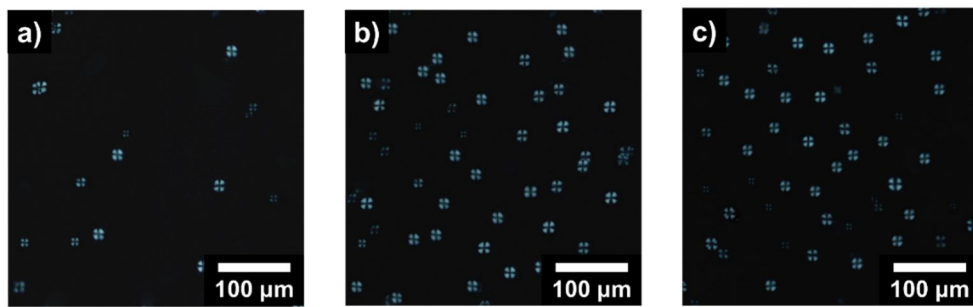


**Figure 15.** Polarized optical microscopy image of a) pristine PVDF, b) PVDF/ZnO rods, c) PVDF/ZnO disks.

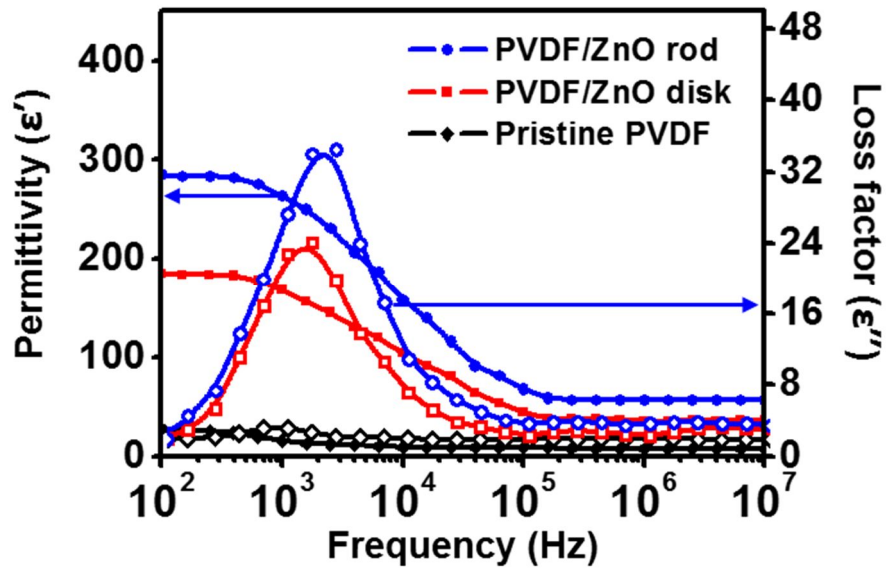


**Figure 16.** The permittivity and losses of the tactile sensor fabricated with PVDF and different ZnO nanostructures.

**Table 1.** The dielectric parameters of the PVDF film and the two composite ZnO/PVDF films.

| Sample        | $\epsilon_s$ | $\epsilon_\infty$ | $\Delta\epsilon^a$ | $\lambda[\mu s]^b$ |
|---------------|--------------|-------------------|--------------------|--------------------|
| PVDF/ZnO rod  | 291          | 73                | 218                | 101                |
| PVDF/ZnO disk | 192          | 54                | 138                | 120                |
| Pristine PVDF | 22           | 13                | 9                  | 157                |

<sup>a</sup> Values were calculated by Havriliak-Negami and Fourier transforms relationship

<sup>b</sup> Values were obtained by interfacial polarization response by relaxation time.

**Table 2.** Relevant dielectric parameters at  $10^4$  Hz for PVDF/ZnO nanodisk composite with various filler contents.

| Sample                         | $\varepsilon'$ | $\lambda$ [ $\mu$ s] |
|--------------------------------|----------------|----------------------|
| PVDF film based on 25 wt% seed | 122            | 128                  |
| PVDF film based on 30 wt% seed | 140            | 121                  |
| PVDF film based on 35 wt% seed | 134            | 122                  |

### 3.1.2. Bifunctional tactile sensor for pressure and temperature

To compare the pressure-sensing properties of the PVDF and ZnO/PVDF composite films, pressure stimuli were used, and the performance was measured from the change in the electrical resistance; i.e.,  $\Delta R = R_{loading} - R_{unloading}$  (Figure 17). The assembled device had an overlap area of  $6 \times 6 \text{ cm}^2$ , and was measured with a gradual increase in pressure. Figure 18 shows how the composite device formed of PVDF, ZnO nanorods and ZnO nanodisks responded to application of a constant pressure. The surface of compressed ZnO nanorods generates a negative potential, and the electrical contact with the rGO electrode layer and the forward bias of the Schottky barrier at the interface results in a change in the resistance of the device. The I-V characteristic curves of bare ZnO nanorods and ZnO nanorods with rGO electrode were evaluated by current-sensing AFM (CSAFM) at 300 K in Figure 19 [85-88]. The I-V curves of pristine ZnO nanorods were evaluated by CSAFM (Figure 19a.). As a result, the point contact on pristine ZnO nanorods showed nonlinear and asymmetric behavior as respected under contact force of 30 nN. Moreover, it has a turn-on voltage of 0.75 V to 1.1 V for the forward bias and reverse bias voltage of -2.1 V that results from rectifying contact in Figure 19b. Also, improved electrical characteristics of ZnO with rGO deposition was obtained in the same manner as shown in Figure 20a and a typical I-V curve between CSAFM tip and rGO layer was observed in Figure

20b which the rectifying behavior in I-V characteristics results in Schottky contact. A difference in the response  $\Delta R$  to the same pressure was observed between devices, and the PVDF/ZnO nanorods composite device exhibited the greatest signal in response to a given stimulus. Because of the 1D structure of the vertically grown ZnO nanorods, they generate an enhanced piezoelectric response to mechanical displacement than the ZnO nanodisks. The larger aspect ratio and permittivity lead to a change in the electrical resistance in response to even a slight deflection of the ZnO nanorods.

The pressure-sensing capability of the system was evaluated from the response  $\Delta R$ , as shown in Figure 21. The smallest detectable pressure using the PVDF/ZnO nanorod film was 10 Pa (giving  $\Delta R = 0.062 \Omega$ ), which corresponds to  $1 \text{ mg mm}^{-2}$ , which is 1000-fold more sensitive than the minimum requirements for artificial skin. The response times of the output signals from PVDF/ZnO nanorod device were obtained under various pressures at 20°C. The recovery times exhibited similar as shown in Figure 22 and 23. Additionally, three different conducting material of rGO, CNT and poly(3,4-ethylenedioxythiophene):poly(styrenesulfonate) (PEDOT:PSS) were candidate to demonstrate pressure sensitivity as a function of various electrode (Figure 24). The sheet resistances of commercial PEDOT:PSS (Sigma-Aldrich) and carbon nanotubes (CNT) (Sigma-Aldrich), and synthesized rGO were 34, 10

and 0.7 k $\Omega$ /sq. As a result, PVDF/ZnO rods with rGO electrode has highest sensitivity under constant pressure compare to other electrode utilized device.

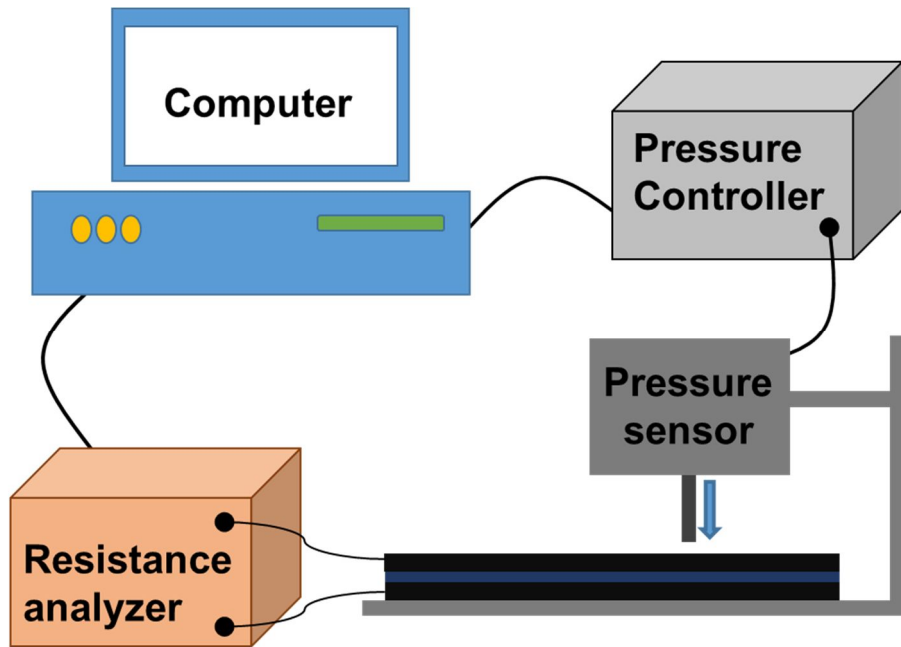


**Figure 17.** Schematic illustration of the pressures sensing measurement which consists of a pressure controller, pressure gauge sensor and computer based resistance analyzing interface.

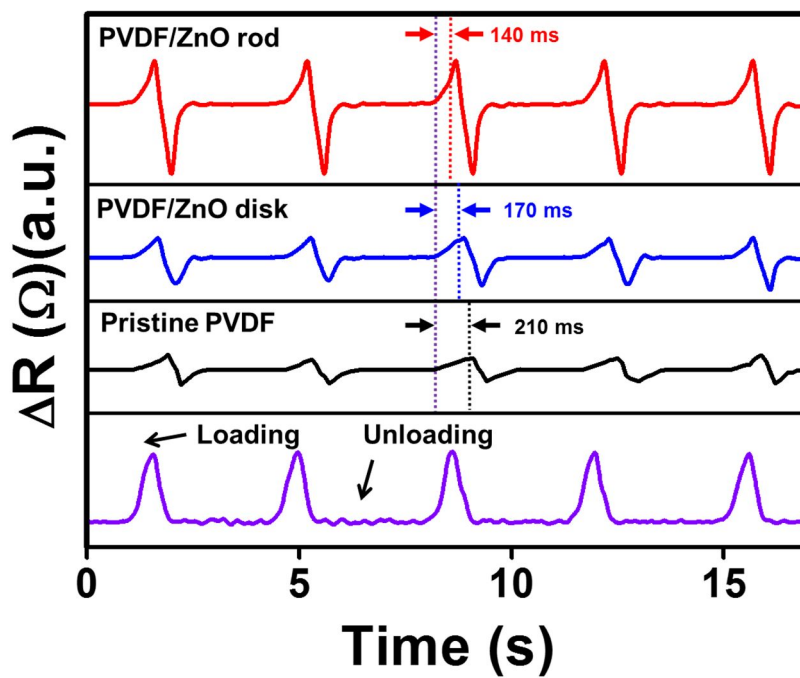


**Figure 18.** The change in resistance of the pristine PVDF, and the PVDF/ZnO composite films. In response to an applied pressure of 30 Pa, showing the response time.

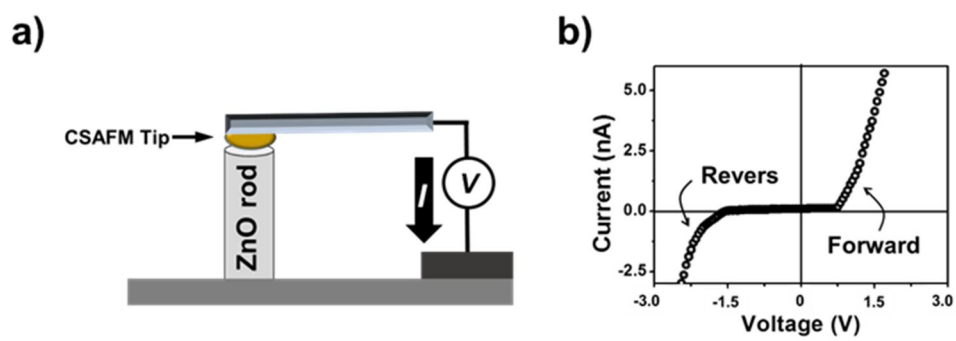


**Figure 19.** Schematic illustration of (a) current-sensing AFM method and (b) I-V characteristic curve of a pristine ZnO rod.

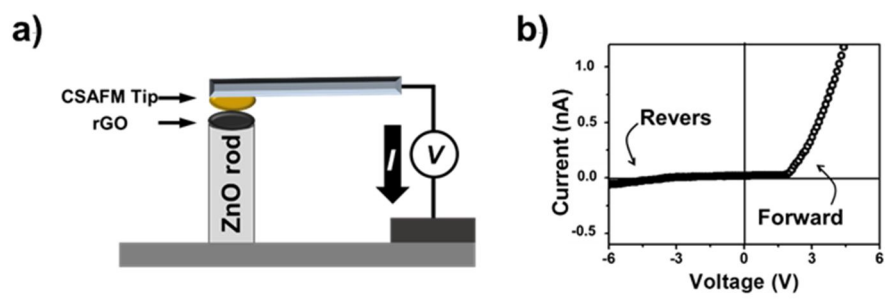


**Figure 20.** Schematic illustration of (a) current-sensing AFM method and (b) I-V characteristic curve of a ZnO rod with rGO.

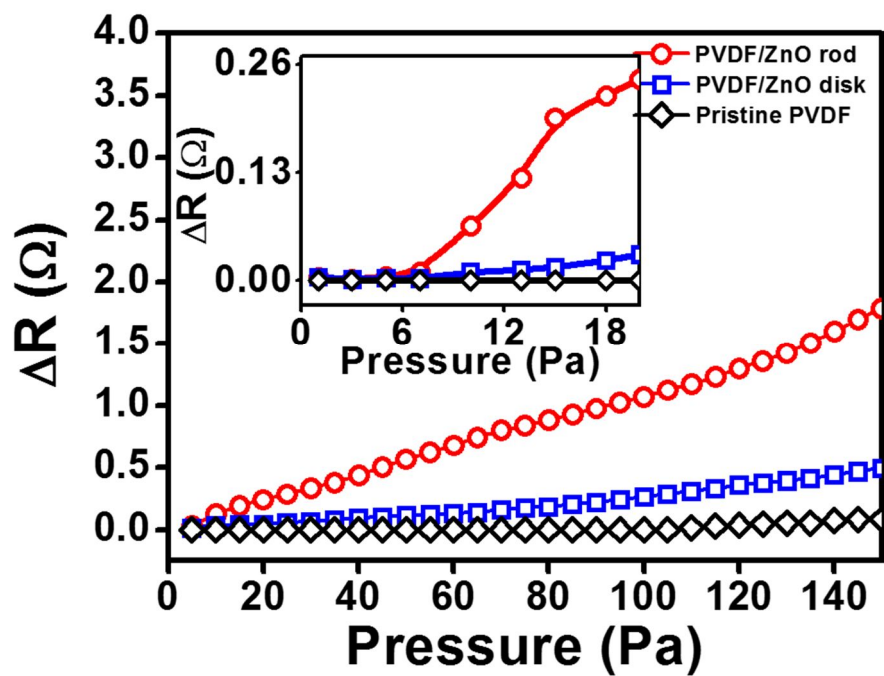


**Figure 21.** The change in resistance of the pristine PVDF, and the PVDF/ZnO composite films. Testing the minimum pressure level of the films at 20°C.

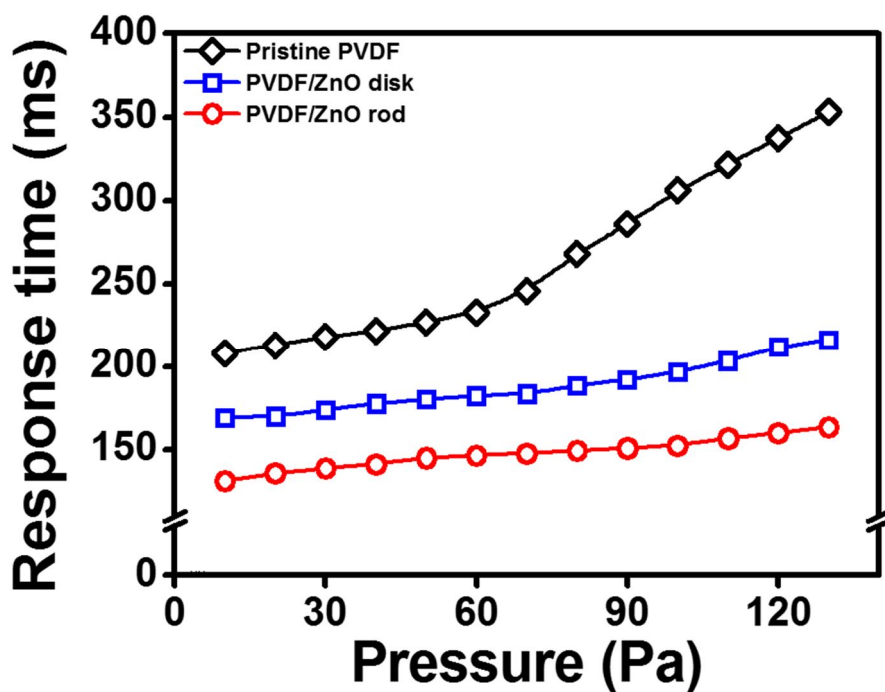


**Figure 22.** The response times of the PVDF film, the ZnO nanodisk/PVDF film, and the PVDF/ZnO nanorod with various pressures.

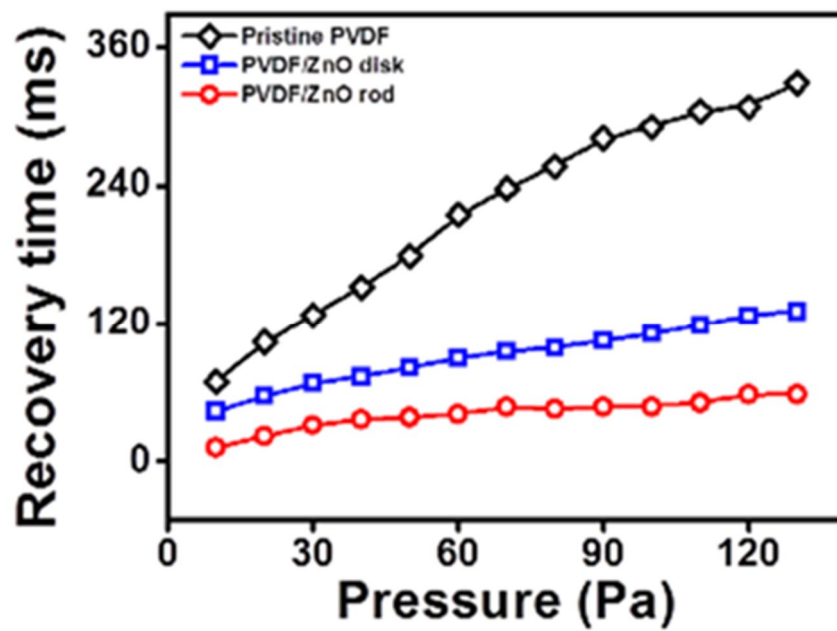


**Figure 23.** The recovery times of the PVDF film, the ZnO nanodisk/PVDF film, and the PVDF/ZnO nanorod with various pressures.

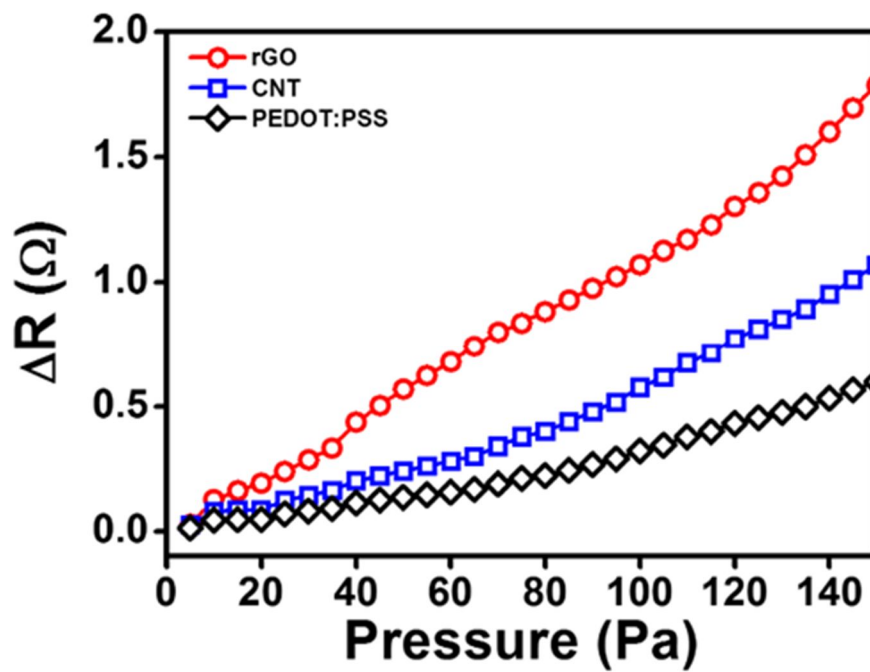


**Figure 24.** Change in resistance of PVDF/ZnO nanorod composite film with three different electrodes by applied various pressure.

To investigate the spatial resolution of the pressure-sensing ability, ZnO/PVDF devices were fabricated, as shown in Fig. 6. The film was divided into 144 regions, each  $0.5 \times 0.5 \text{ cm}^2$ , and Pt weights were used to apply a pressure of 30 Pa at each division, one at a time. The output signal was measured from the change in the resistance using a pseudocolor plot, as shown in Figure 25a. The two-dimensional (2D) intensity profiles of the PVDF/PVDF/ZnO nanorod film are shown in Figure 25b, and the 2D intensity profile of that formed using the PVDF/ZnO nanodisk film are shown in Figure 25c. The distribution of the operational device area containing the ZnO nanorods in the PVDF thin film was 96%, and that containing the ZnO nanodisks was 77%. As the areal density of ZnO nanorods was larger, and significant aggregation did not occur, in contrast to the ZnO nanodisks, and so we may expect a more uniform pressure sensitivity with the PVDF/ZnO nanorods composite film.

The device composed of the PVDF/ZnO nanorods composite was used to measure the output signals with various temperatures and applied pressures. To evaluate the pyroelectric response, a pressure of 30 Pa, was applied at 20, 70, and 120°C in the center of device, as shown in Figure 26. We found that the response was slower, and the recovery time longer, at higher temperatures. This is because the pyroelectricity originated from the PVDF, and the thermal energy released from the heated weight on the surface of PVDF thin film

resulted in slower motion of the dipoles [89-96]. Loading at 20°C resulted in a recovery time of 190 ms, loading at 70°C resulted in a recovery time of 680 ms, and loading at 120°C in a recovery time of 1150 ms.

As shown [Figure 27 and 28](#), reproducible responses to changes in temperature and pressure were obtained. The independence of  $\Delta R$  and the recovery time enabled measurement of pressure and temperature independently. Compare to obtained respons and recovery time, it is found that recovery time has wide delayed time range, 1150 ms at 120 °C with 30 Pa whereas delayed response time observes 92 ms. Additionally, the analyzed uniformity of temperature-sensing at the fabricated ZnO nanorods embedded PVDF thin film was 94% ([Figure 29](#)). Considering these results, it is worth nothing that investigation of resistance difference make it feasible to measure the weight of pressure, and delayed recovery time play a pivotal role in determining the temperature of target object.

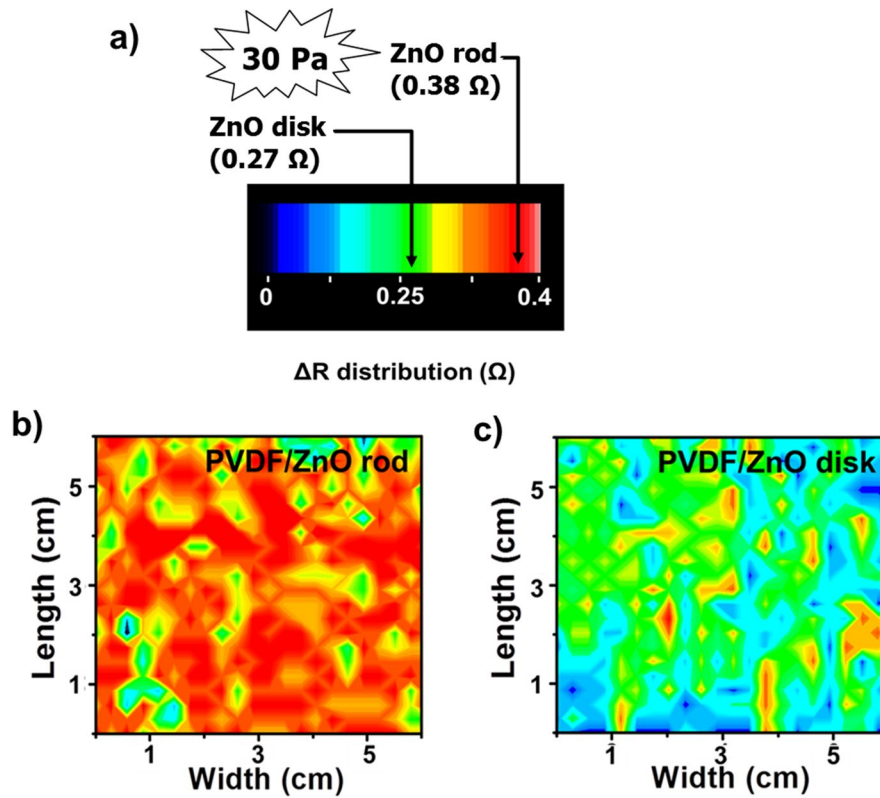


**Figure 25.** (a) The spatial variation in the change in resistance. The effective area of fabricated device are  $6 \times 6 \text{ cm}^2$ . (b) The PVDF/ZnO nanorod film exhibited a higher pressure sensitivity than (c) the PVDF/ZnO nanodisk film. The film was divided into 144 regions ( $0.5 \times 0.5 \text{ cm}^2$ ) and Pt weights were used to apply a pressure of 30 Pa at each division, one at a time.

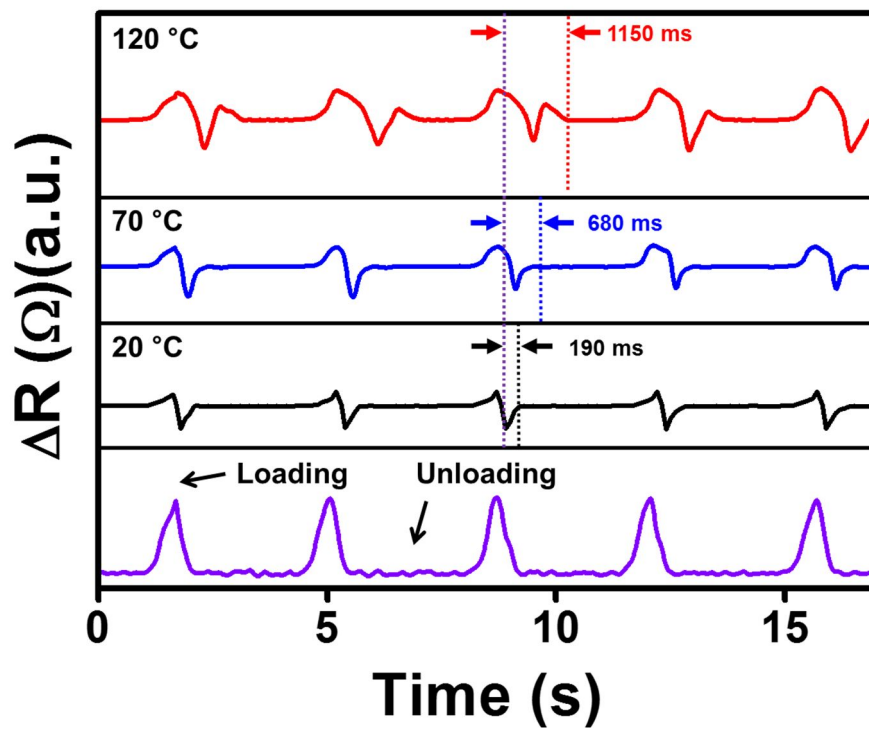


**Figure 26.** The output resistance of the PVDF/ZnO nanorod device at various temperatures, 20, 70, and 120°C, under constant pressure of 30 Pa in the center of device.

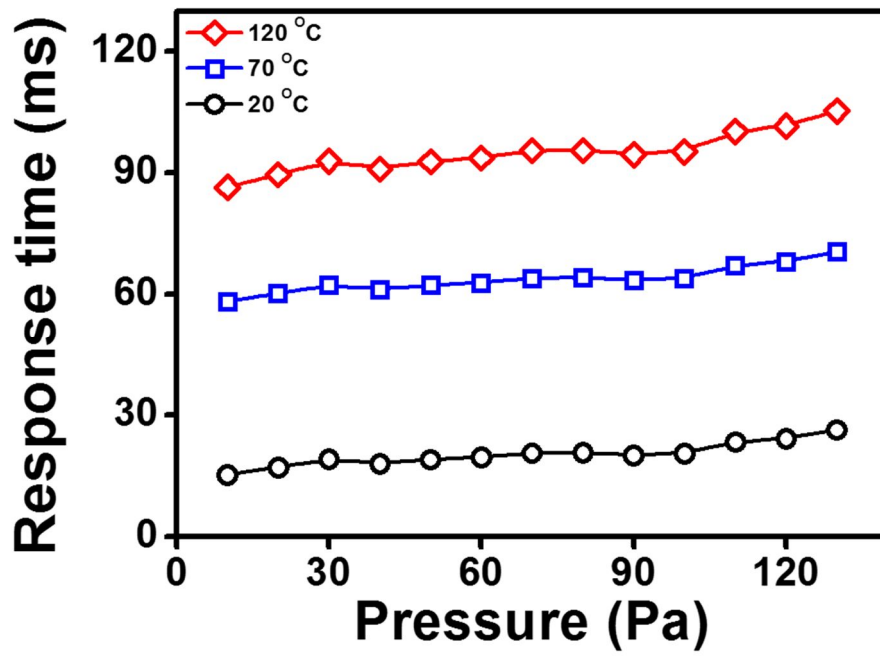


**Figure 27.** The response time of PVDF/ZnO nanorod film at the different pressures with various temperatures.

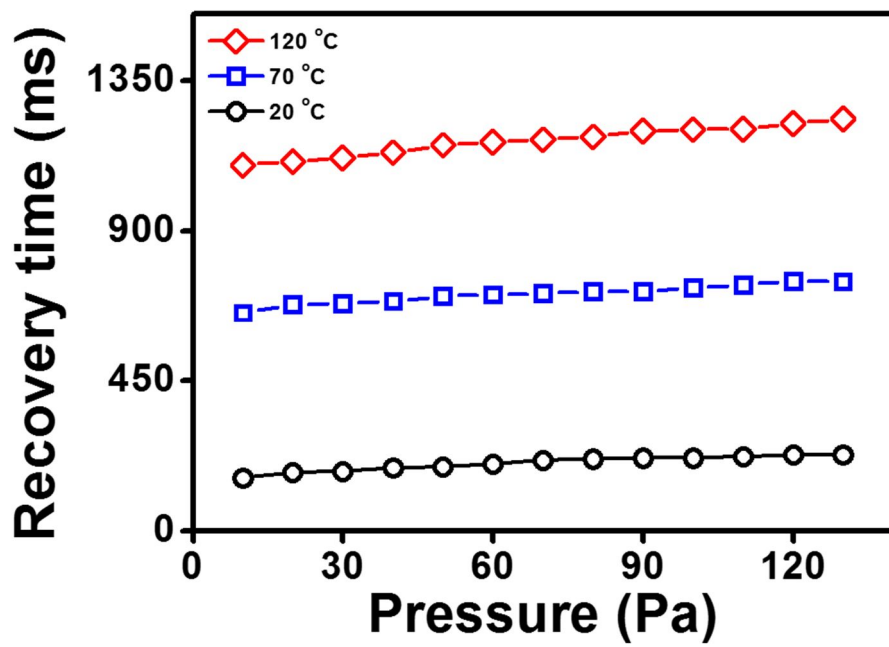
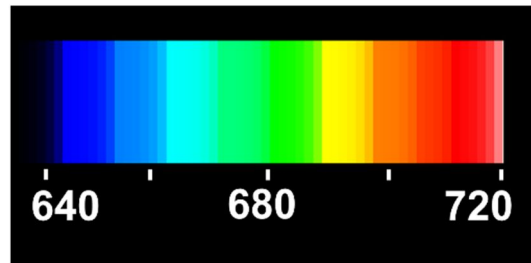


**Figure 28.** The recovery time of PVDF/ZnO nanorod film to the different pressures at various temperatures.

a)



Recovery time distribution (ms)

b)

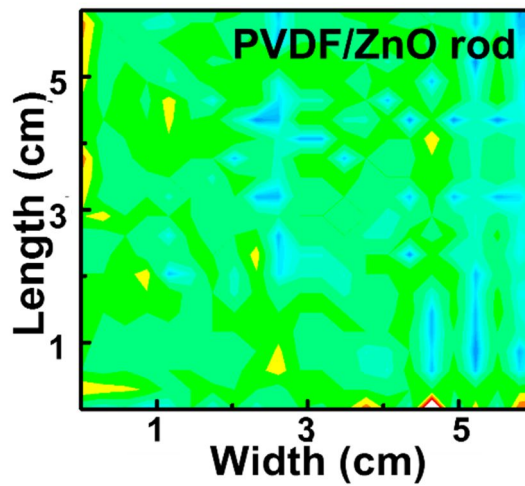


**Figure 29.** (a) The spatial variation of recovery time distribution by mille seconds. (b) . The fabricated PVDF/ZnO rod based film (effective area of  $6 \times 6 \text{ cm}^2$ ) was divided into 144 regions ( $0.5 \times 0.5 \text{ cm}^2$ ) and  $70^\circ\text{C}$  of Pt weights were used to apply a pressure of 30 Pa at each division, one region at a time, and it shows that 94 % of reliable uniformity by visual color distribution for recovery time of 679~682 ms which represents surface temperature of  $70^\circ\text{C}$ .

Mapping data of the two independent factors was evaluated based on external pressure loaded simultaneously and the temperature of the device. As shown in [Figure 30a](#), the applied pressure changed the resistance. Increasing the temperature of the object placed on the thin film to apply the pressure increased the recovery time of the signal, and so the temperature of object could be calculated based on the recovery time. To investigate the scope for simultaneous pressure and temperature sensing in real time, a 15- $\mu$ L mineral oil droplet dropped from an initial height of 1.5 cm was measured under a low-noise environment, as shown in [Figure 30b](#). Data were collected during the initial impact, and during the time when the droplet rebounded from the surface, and impacted again, bouncing on the surface over a period of 1.2 s, as shown in [Figure 31](#). The maximum signal at 20°C following the impact of the droplet onto the film was  $\Delta R = 1.62 \Omega$ , which is equivalent to a pressure of 90 Pa; the recovery time was 180 ms. The signal when a droplet with an unknown temperature was dropped from the same height was monitored. The maximum response was  $\Delta R = 1.61 \Omega$ . However, recovery time was 815 ms, which corresponds to a droplet temperature of 80°C. The difference in the two peak shapes is attributable to the difference in the sample temperature of each droplet. The 20°C droplet that impacted on the film did not heat the film, because they were at an identical temperature. Therefore, the bouncing

movement of a droplet can be detected after its first impact at 510 ms. However, the 80°C droplet was able to transfer both kinetic energy and heat to the film. For this reason, the recovery time was prolonged. Therefore, this system enables independent measurement of pressure and temperature based on the magnitude of the change in the resistance and the recovery time of the signal.

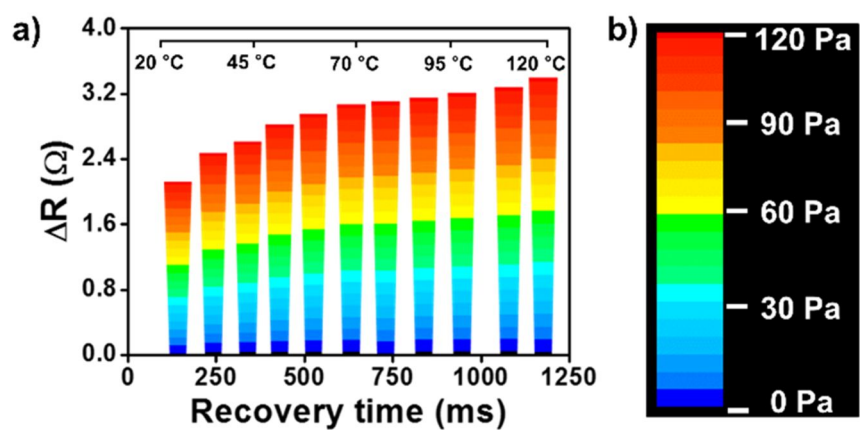


**Figure 30.** The relationship between external pressure and the temperature of the object placed on the device to induce a pressure response. (a) The change in the resistance and recovery time. (b) Pseudocolor plots showing the applied pressure on the PVDF/ZnO nanorod film.

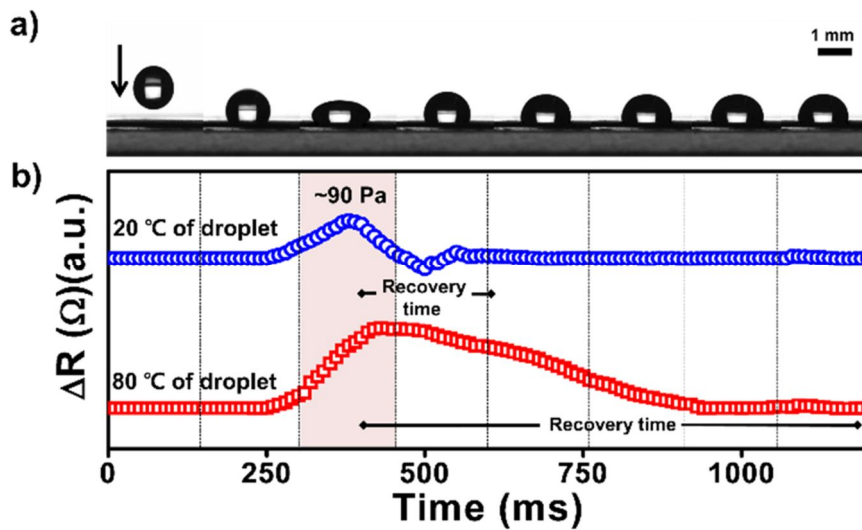


**Figure 31.** The relationship between external pressure and the temperature of the object placed on the device to induce a pressure response. (a) The response to impact of a droplet with an unknown temperature. (b) The recovery time shows that the temperatures of the droplets were 20°C and 80°C, and the pressure was 90 Pa.

## **3.2. Fabrication of PVDF Thin Film with Free-standing Needle-like ZnO for Wireless Heart Rate Monitoring**

### **3.2.1. Fabrication of PVDF thin film with free-standing needle-like ZnO rod**

As piezoelectric materials for pressure sensor, ZnO nanorod and needle were grown via the hydrothermal approach [97-98]. The morphology of ZnO has controlled by hydrothermal time and concentration of growth solution. At the early stage of hydrothermal method, ZnO nucleates spontaneously from the ionized  $\text{Zn}(\text{OH})_4^{2-}$  seed to hexagonal nanostructure, and it can be grown one dimensional rod by increment of temperature and concentration. FE-SEM images reveal that high density of ZnO nanorod ( $1.42 \times 10^{10} \text{ cm}^{-2}$ ) and nanoneedle ( $1.01 \times 10^{10} \text{ cm}^{-2}$ ) were successfully formed (Figure 32a and b). The length of ZnO nanorod and nanoneedle was measured to be *ca.* 300 and 280 nm with diameters of *ca.* 100 nm and 50 nm, respectively. The XRD analysis for ZnO nanorod and nanoneedle indicates that all of the diffraction peaks can be exactly indexed to the hexagonal ZnO with lattice constant  $c = 0.5206 \text{ nm}$ , which is in good alignment of the ZnO along the  $c$ -axis direction (Figure 33).

For the piezoelectric film matrix, PVDF was fabricated by spin coating and poling treatment. The FTIR analysis for pristine PVDF, PVDF/ ZnO nanorod

and PVDF/ ZnO nanoneedle film has been performed to investigate the crystalline ratio of  $\alpha$  and  $\beta$  phase ( $I_{\beta}/I_{\alpha}$ ), since the piezoelectric property of the PVDF is strongly dependent of its  $\beta$  phase content owing to high net dipole moment originated from the all-trans structure (**Figure 34**). Assuming that the IR absorption follows the Beer-Lambert law, the PVDF/ ZnO nanorod and PVDF/ ZnO nanoneedle hybrid film had an increased  $I_{\beta}/I_{\alpha}$  ratio of *ca.* 2.33 (85 %  $\beta$  phase) and *ca.* 2.47 (93 %  $\beta$  phase), respectively, which compared to the pristine PVDF film ( $I_{\beta}/I_{\alpha}$  ratio of *ca.* 1.29 with 73 %  $\beta$  phase content). To achieve an in depth insight into crystallization behavior by ZnO nanofillers in the PVDF matrix, the DSC analysis was conducted (**Figure 35**). The observed crystallization exothermic peaks are observed in the range of 160 to 170 °C, and it was confirmed the role of ZnO nanofillers acted as nucleation agents of PVDF according to increase of crystallization temperature ( $T_c$ ) compared to pristine PVDF. The relative degree of crystallinity as a function of time,  $X(t)$ , can be calculated from relative crystallinity as a function of temperature,  $X(T)$ , by transforming the temperature to a time scale. It indicated that crystallinity of PVDF was the most rapidly formed with ZnO nanoneedle (**Figure 36**). Furthermore, the inset data indicates the natural logarithmic form of Ozawa equation to investigate non-isothermal crystallization of kinetics, which demonstrated that the highest crystallization rate constant ( $k$ ) of 0.05659 could

be obtained with ZnO nanoneedle fillers (Supporting Information). The detailed value has been displayed in **Table 3**. Moreover, POM morphology of the crystal growth shows that the amounts of spherulites have significantly increased with addition of ZnO nanofillers, which means that the ZnO acts as nuclei for PVDF crystallization (**Figure 37**) [99]. Furthermore, it can be inferred that the reinforced crystallization behavior is intimately proportional to content of  $\beta$  phase.

The permittivity and loss factor for three different films were measured as shown in **Figure 38**. According to the Havriliak-Negami and Fourier transfer relationship, the measured permittivities of the samples are listed in **Table 3**. In overall, the permittivity is larger at lower frequencies than at higher frequencies, and embedding the ZnO nanofiller in the PVDF matrix significantly increased the dielectric constant. Especially, the ZnO nanoneedle possessed a greater dielectric constant than the ZnO nanorod due to the larger aspect ratio, which resulted in a larger energy barrier. The relaxation time,  $\lambda$ , is related to the gradient of the loss factor that is associated with the interfacial polarization response of the dielectric material. We found that a relaxation time for pristine PVDF, ZnO nanorod/PVDF and ZnO nanoneedle/PVDF was estimated to be 157, 120 and 101  $\mu$ s, respectively. Based on these dielectric parameters, the inclusion of ZnO in the PVDF film significantly increased the

permittivity and reduced the polarization response time of the PVDF-based pressure sensors.

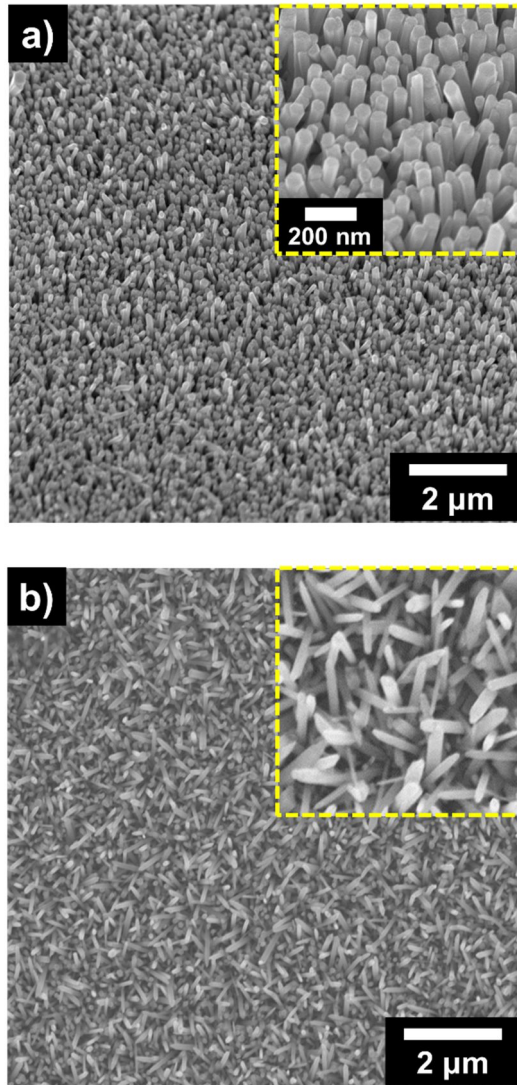


**Figure 32.** Low and high magnification of SEM images for ZnO (a) nanorod and (b) nanoneedle.

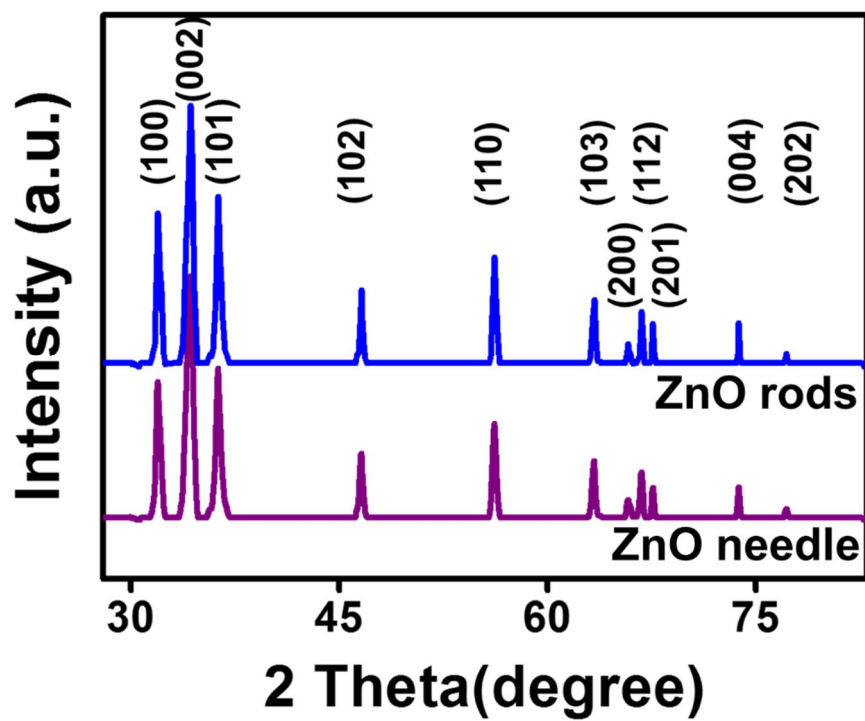


**Figure 33.** XRD spectra to investigate the crystal structure of the ZnO nanorods and nanoneedle.

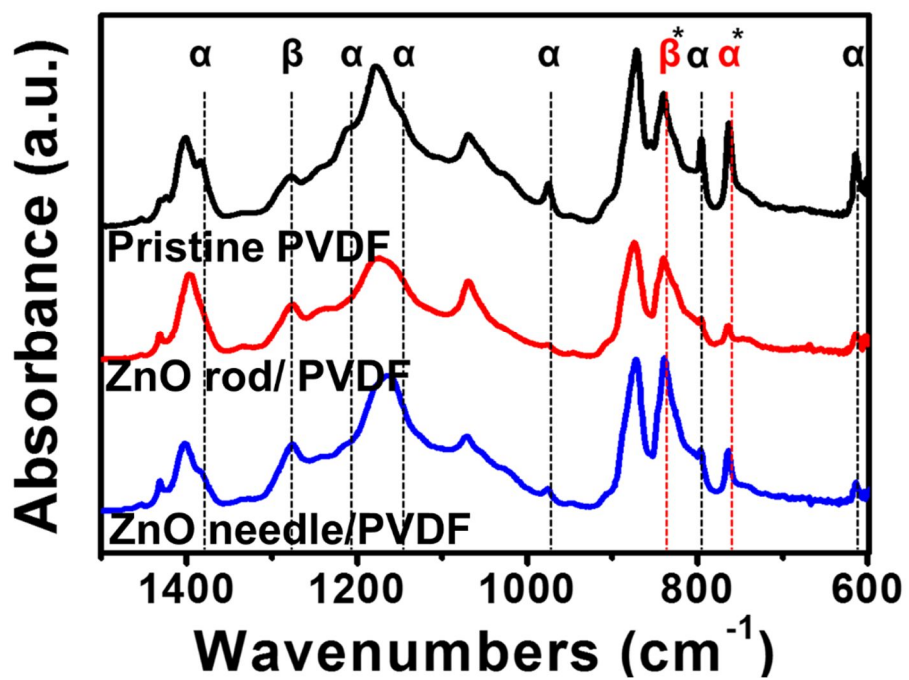


**Figure 34.** FTIR spectroscopy of pristine PVDF, ZnO nanorod/PVDF and ZnO nanoneedle/PVDF film.

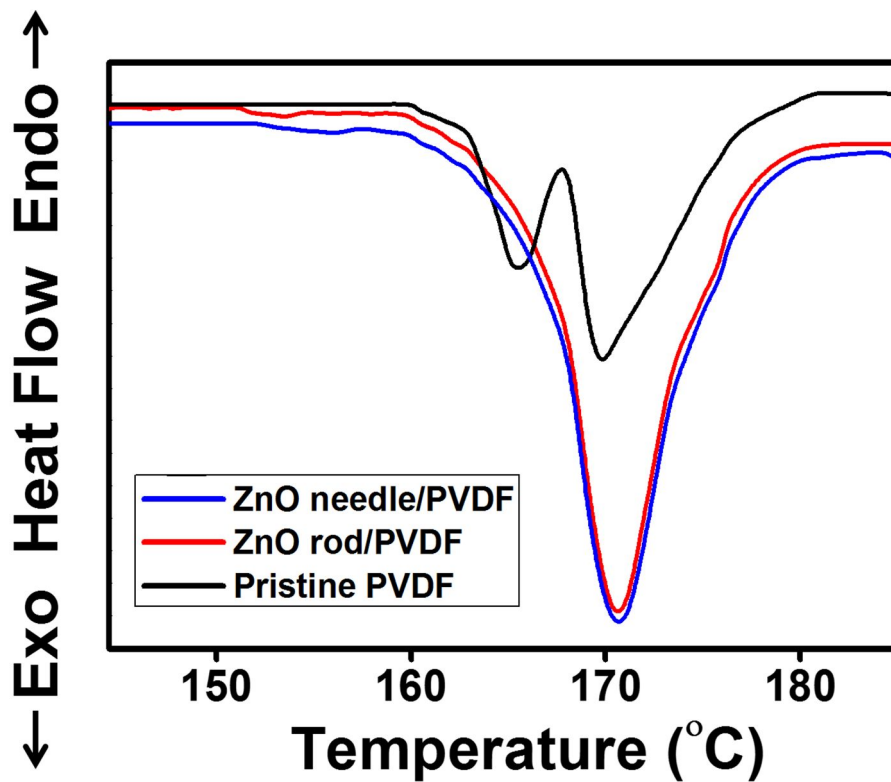


**Figure 35.** DSC thermograms of pristine PVDF, PVDF/ZnO nanorod and PVDF/ZnO nanoneedle film.

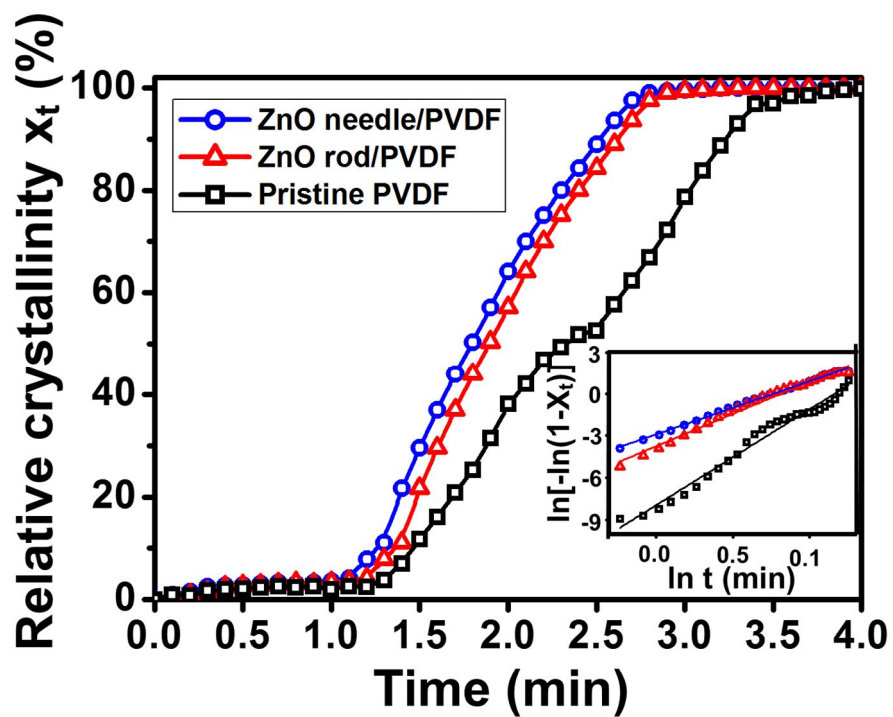


**Figure 36.** The data represented by relative crystallinity as a function of time for three different films (Inset: The plot of  $\ln[-\ln(1 - X_t)]$  versus  $\ln t$  for thermal behavior parameters).

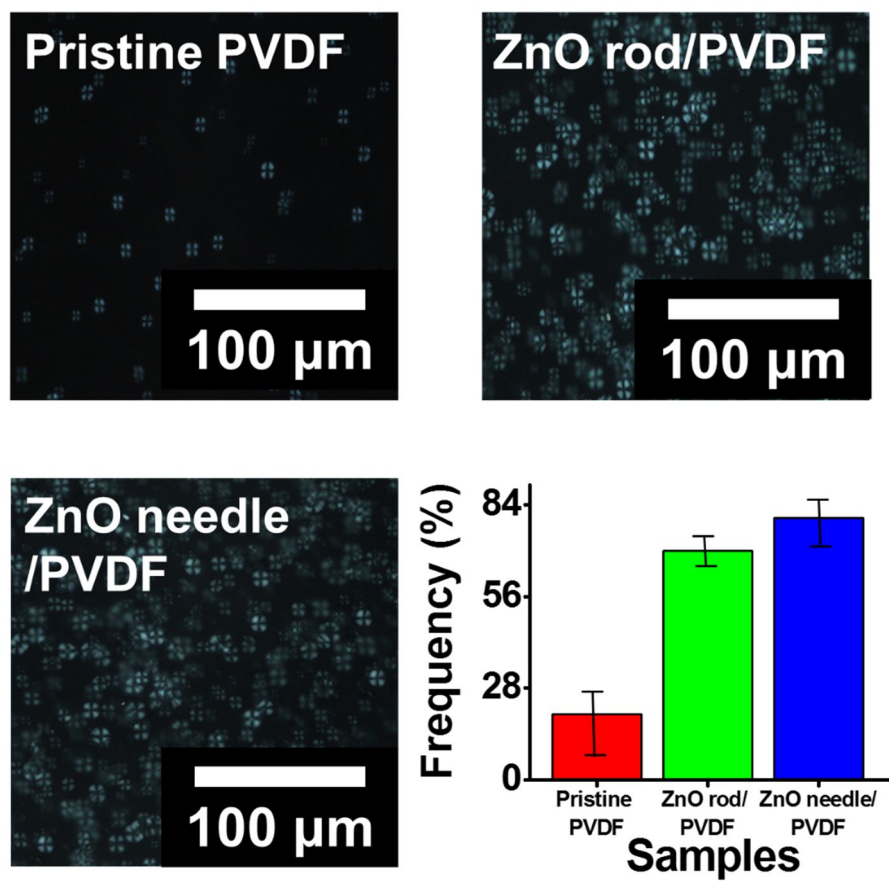


**Figure 37.** Polarized optical microscopy images of pristine PVDF, ZnO nanorod/PVDF and ZnO nanoneedle/PVDF film.

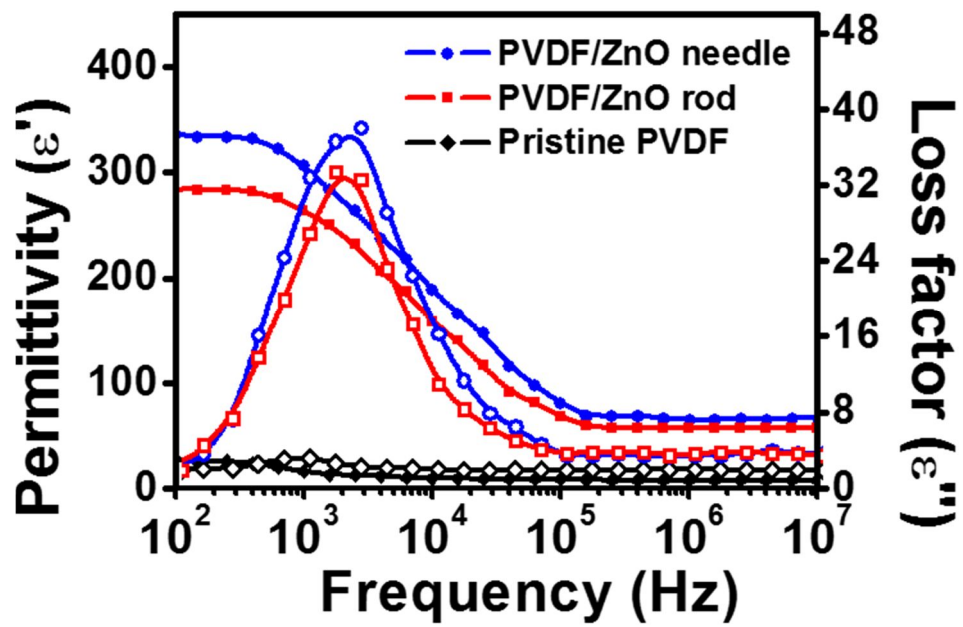


**Figure 38.** Dielectric properties such as permittivity and losses of the hybrid films.

**Table 3.** The values of  $n$ ,  $k$ ,  $t_{1/2}$  and dielectric parameters for pristine PVDF and ZnO/PVDF hybrid films.

| Sample               | $n^a$ | $k^a$   | $t_{1/2}^a$ | $\Delta\varepsilon^b$ | $\lambda/[\mu\text{s}]^c$ |
|----------------------|-------|---------|-------------|-----------------------|---------------------------|
| Pristine PVDF        | 3.004 | 0.00145 | 2.101       | 9                     | 157                       |
| PVDF/ ZnO nanorod    | 1.945 | 0.04561 | 1.512       | 213                   | 121                       |
| PVDF/ ZnO nanoneedle | 1.875 | 0.05659 | 1.498       | 274                   | 97                        |

<sup>a</sup> These values were obtained by Ozawa analysis of samples using DSC.

<sup>b</sup> Data calculated using the Havriliak-Negami and Fourier transform relationship.

<sup>c</sup> Data were obtained via the interfacial polarization response relaxation time.

### 3.2.2. Wearable and wireless heart rate sensor

**Figure 39** shows the photograph of a wireless heart rate monitoring system composed of pressure sensor, signal analyzer, Bluetooth transmitter and smart phone. To operate the wireless smart sensor, an electrical Bluetooth transmitter circuit was installed. The piezoelectric signal generated by the pulse has been delivered onto the Bluetooth circuit via signal analyzer to transmit wireless signal to the smart phone, and the smart phone screen presented the received pulse signal in real time. **Figure 40** demonstrates the schematic illustration of a flexible pressure sensor based on free-standing ZnO filler in the PVDF film (*ca.* 45  $\mu\text{m}$  thickness) between rGO electrodes. The I-V characteristic curve of the hybrid film with rGO electrodes represents that the point contact on the ZnO surface has the nonlinear and asymmetric behavior under contact force of 30 nN, which indicated of Schottky contact (**Figure 41**). Work function of rGO and ZnO was assumed to be 4.31 and 3.95 eV, respectively. Energy diagrams of rGO/n-type ZnO junction at equilibrium and under applied potential have been shown in **Figure 42**. Since the junction is rectifying contact, electron can flow from ZnO to rGO electrode via forward bias, while flow toward reverse direction is not facilitated. Inset shows a turn-on voltage  $\sim 1.8$  V for the forward bias and the voltage has been almost maintained under pressure. Where the voltage is applied over  $\sim 1.8$  V, the current of the hybrid device under the

compressive strain has decreased with increased voltage, which presents the downward I-V behavior. The phenomena can be explained in terms of the piezotronic effect, which describes the coupling of piezoelectric polarization and the intrinsic electric field in a space charge region. Once a compressive strain is applied to ZnO, it can produce a permanent polarization that induces non-mobile negative ionic charges at the rGO and ZnO interface. Since free electrons can partially screen the piezo-charges due to the finite permittivity and the limited doping concentration, the positive charges have produced at the metal side by mirror effect. It causes the negative piezopotential at the rGO and ZnO interface, which can shift the fermi energy level. As a result, the Schottky barrier height becomes pronounced, and thus a resistance has increased. The well-defined rGO pattern has been successfully printed on the PCB board of Bluetooth transmitter using rGO conducting ink for screen printing, and it can be utilized for the Bluetooth antenna (**Figure 43**).

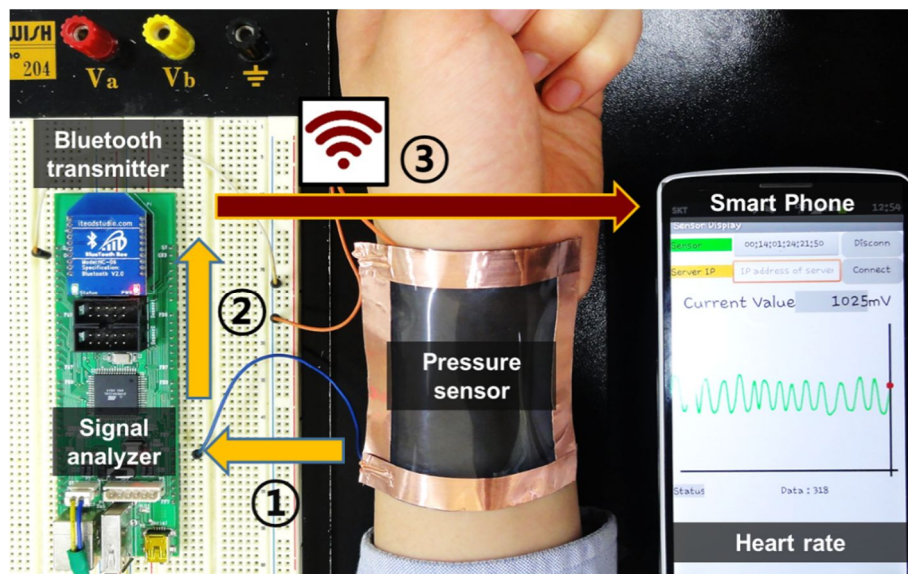


**Figure 39.** Photograph of wearable and wireless pressure sensor for heart rate monitoring.

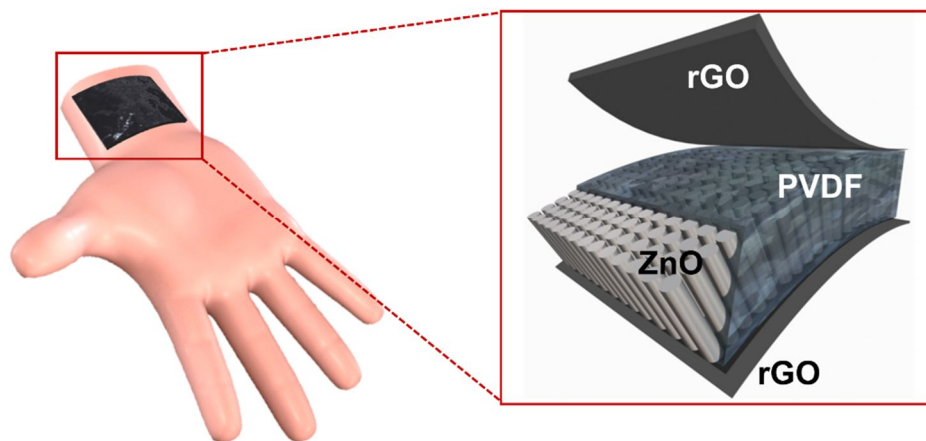


**Figure 40.** Schematic diagram of the pressure sensor using free standing ZnO/PVDF hybrid film between rGO electrodes.

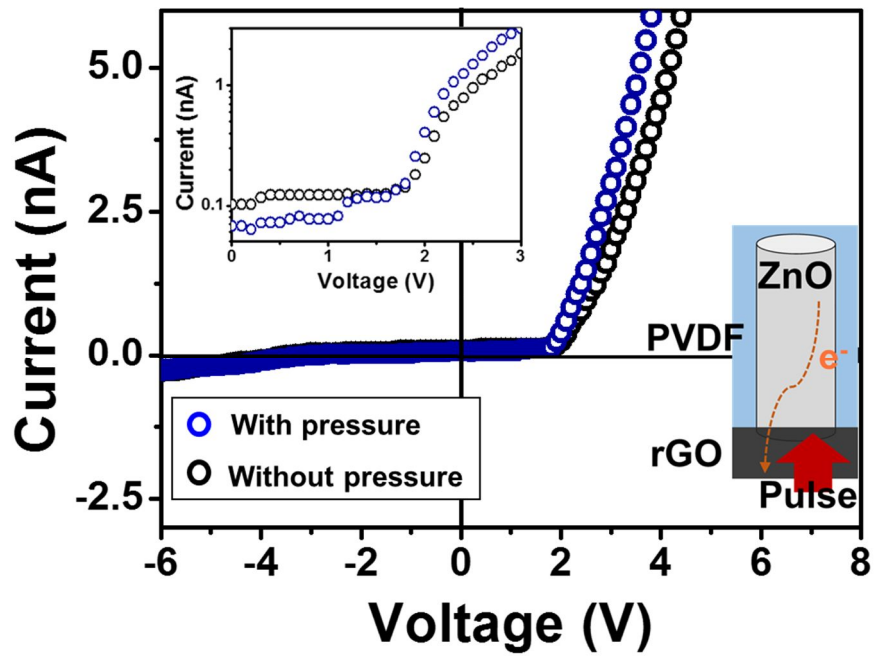


**Figure 41.** The I-V characteristic curve of the hybrid device that rectifying behaviour of Schottky contact under compressive strain. The insets show a log  $I$  vs  $V$  plot and schematic illustration of forward bias when pressure is applied.

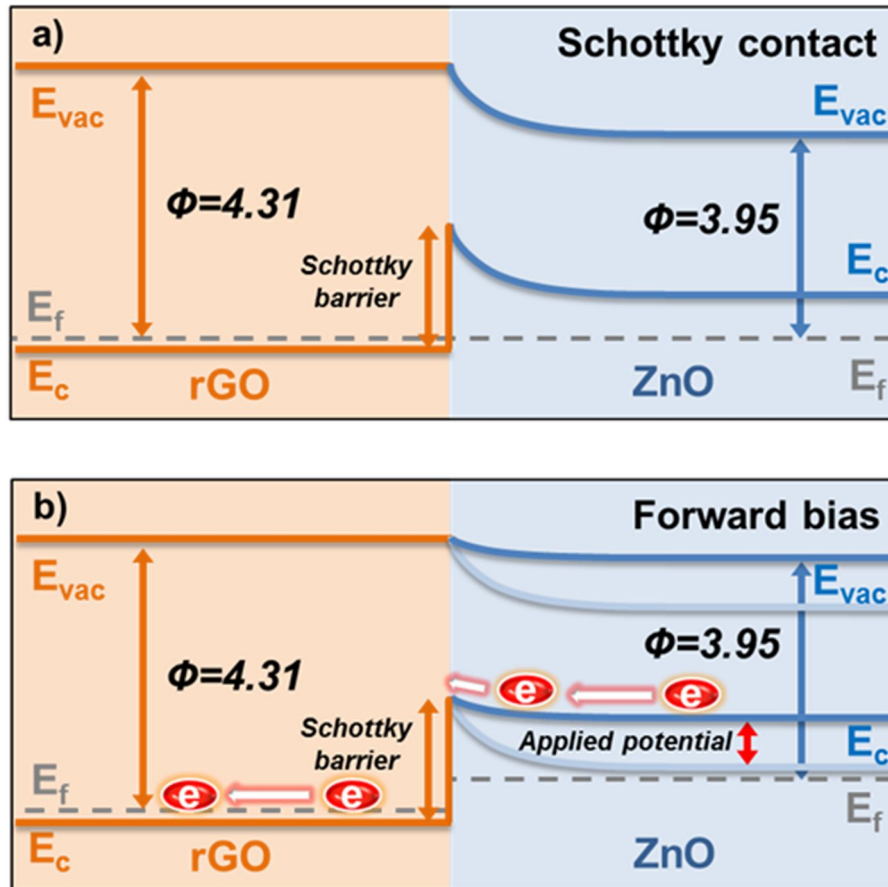
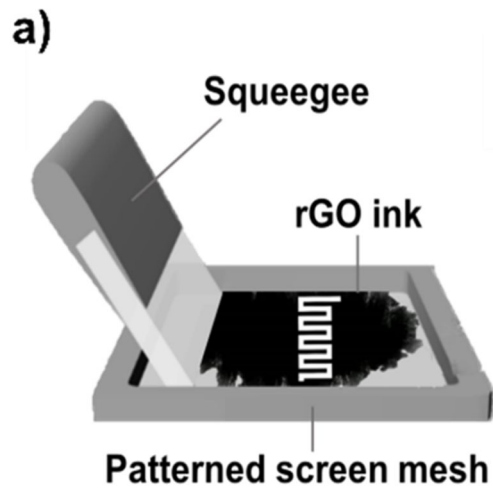


**Figure 42.** Energy diagrams of rGO/ZnO junction a) at equilibrium and b) under forward bias.



b)

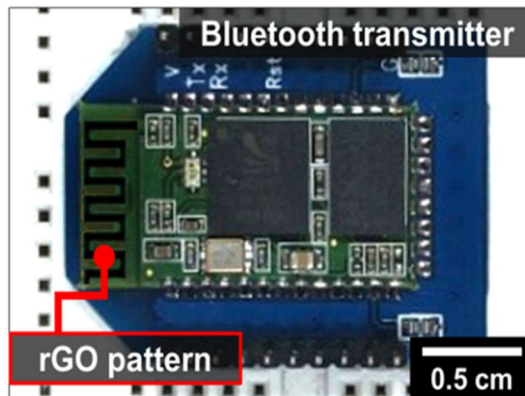


**Figure 43.** Fabrication of rGO-based Bluetooth antenna pattern on PCB board via screen printing and (e) photograph of the Bluetooth transmitter with rGO-based antenna to transmit inputted pulse signal to the smart phone.

For the fabrication of the rGO film onto the both sides of ZnO/PVDF hybrid film, exfoliated GO aqueous solution was used as conductive ink for screen printing, and the thermal annealing for a reduction process was performed under vacuum condition (*ca.*  $10^{-3}$  torr). The hydrophilic property and good dispersibility of the GO solution could make it possible to be printed onto the hybrid film through an open mesh area. As a result, rGO electrodes could be efficiently synthesized over a large area ( $6 \times 6 \text{ cm}^2$ ). To confirm the successful reduction of exfoliated GO to rGO, XPS and Raman analysis were conducted (**Figure 44**). The XPS results showed that the  $I_{C-O}/I_{C-C}$  ratio has decreased from 0.88 (GO) to 0.23 (rGO). Moreover, the Raman spectra indicated an increased  $I_D/I_G$  intensity ratio, which suggested a decrease in the average size of the  $sp^2$  domains upon reduction of the exfoliated GO. Judging from these data, it was evident that the printed GO was successfully reduced to rGO film by the hydrazine vapor as a reducing agent.

**Figure 45a** represents the return loss curve of rGO and commercial gold pattern-based Bluetooth antenna. Generally, the performance of an antenna is evaluated using its mean frequency and voltage standing wave ratio (VSWR) or return loss (RL), which is indicative of transmitted power efficiency [100]. The rGO and gold pattern-based antennas had mean frequencies of 2.43 and 2.42 GHz, respectively. The VSWR (1.38) and RL (15.9) values of the rGO

pattern-based antenna indicated transmitted power efficiency of 97.5%, which is comparable to that of gold pattern-based antenna (**Table 4**). The power gain, which combines the antenna directivity and radiation efficiency, of rGO pattern-based antenna was measured. Especially, radiation efficiency indicates of the ohmic/dielectric power loss in the antenna itself, and thus it is a measure of the radiating electromagnetic energy that propagates into the surrounding space through the antenna. **Figure 45b** shows that the rGO pattern-based thin film acted as omnidirectional antennas with relatively low gain along the substrate direction with a resultant interruption in wave propagation. As a result, the rGO pattern-based antenna exhibited a peak gain of 2.70 dBi with a higher radiation efficiency of 78.38%, which was applicable to be used as a Bluetooth antenna to transmit wireless signal to the smart phone.

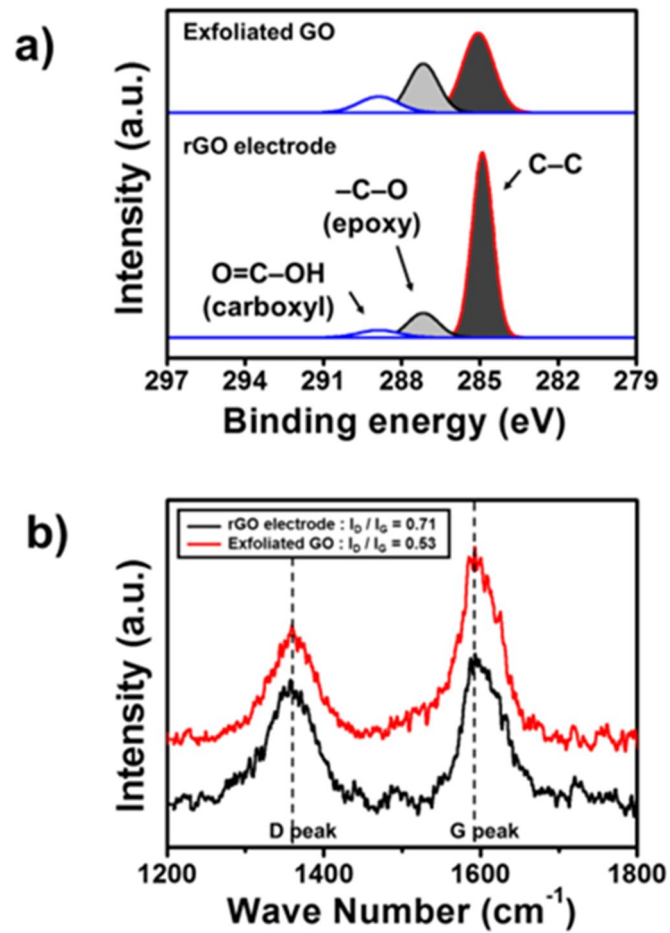


**Figure 44.** (a) XPS spectrum in the C 1s region and (b) Raman spectra of the exfoliated GO and rGO electrode for ZnO/PVDF hybrid film-based pressure sensor.

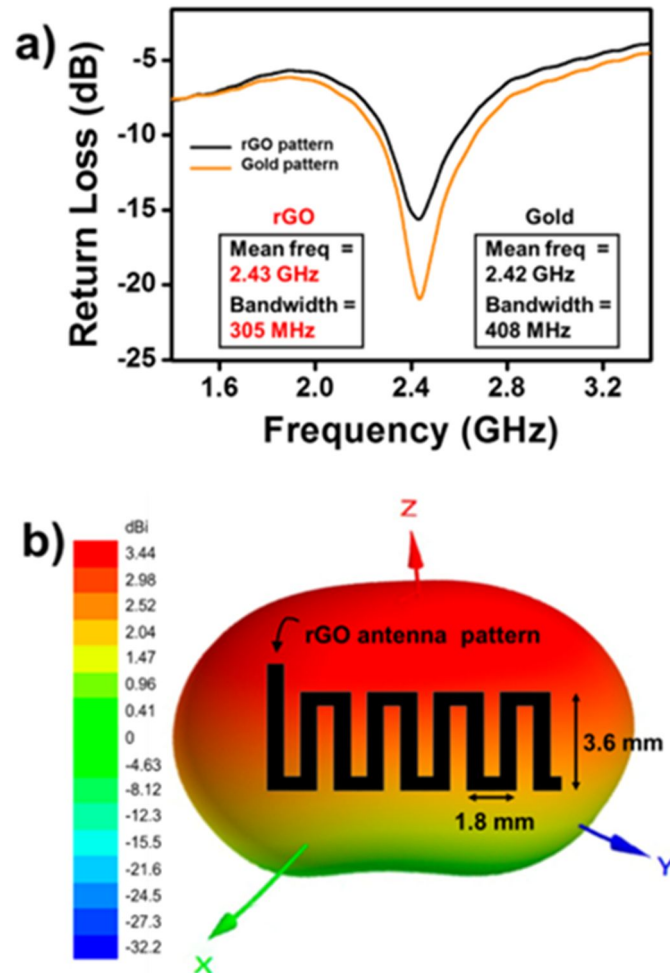


**Figure 45.** (a) The return loss curve of rGO and gold pattern-based Bluetooth antenna. (b) The radiation 3D pattern of rGO pattern-based Bluetooth antenna.

**Table 4.** VSWR, return loss (RL) and transmitted power values of rGO and gold pattern-based Bluetooth antenna.

| Sample | VSWR | RL (dBi) <sup>a</sup> | Transmitted power (%) |
|--------|------|-----------------------|-----------------------|
| RGO    | 1.38 | 15.90                 | 97.5                  |
| Gold   | 1.19 | 21.66                 | 99.2                  |

<sup>a</sup> These values were acquired in the E5071C ENA RF Network Analyzer of Agilent Technologies.

In order to compare the pressure sensing ability of the pristine PVDF and ZnO/PVDF hybrid films, a mechanical stimulus of pressure was inputted, and the performance was confirmed by changes in electrical resistance ( $\Delta R = R_{loading} - R_{Unloading}$ ). In our experiment, the optimized film thickness was assumed to be *ca.* 80  $\mu\text{m}$  considering the minimum pressure detection limits and response times. **Figure 46** shows that the thickness is associated to the minimum pressure detection limits and response times. The minimum pressure detection limits for hybrid films with 60, 80, and 100  $\mu\text{m}$  thickness were 3.8, 4.2, and 12.3 Pa, respectively. In addition, comparing response time values were 111, 124, and 163 ms, respectively. These results demonstrate that over 100  $\mu\text{m}$ -thickness of film is unsuitable for our sensing system. Furthermore, the main difference of 60 and 80  $\mu\text{m}$  was an error bar distribution. Namely, the 60  $\mu\text{m}$  of film has more rapid time but inaccurate mean times than 80  $\mu\text{m}$  hybrid film. For this reason, the optimized film thickness was assumed to be *ca.* 80  $\mu\text{m}$ . **Figure 47** illustrate the performance of three different pressure sensors as a function of the applied constant pressure (10, 25 and 50 Pa). Overall, the ZnO/PVDF film-based pressure sensors had a faster response time and higher changes in electrical resistance for output signals than pristine PVDF film-based device. Improved permittivity of the hybrid film enables to have a high electronic polarizability under pressure, which causes increased negative

piezopotential and the Schottky barrier. Thus, the electron flow by forward bias has reduced, which resultant in the high resistance change. Notably, the lowest detectable pressure of ZnO nanoneedle/PVDF film showed as small as 4 Pa (giving  $\Delta R = 0.062 \Omega$ ), which was extremely smaller than the pressure induced by a gentle touch ( $\approx 1.2 \times 10^4$  Pa) (**Figure 48**). Because slight movement and deflection of ZnO nanoneedle with large aspect ratio and high permittivity by applied pressure can be interpreted as a scalar change of electrical resistance. Furthermore, ZnO nanoneedle/PVDF film-based pressure sensor maintained its sensing ability after repeated loading-unloading of pressure (1,000 cycles), which  $\Delta R$  was *ca.* 0.12, 0.24 and 0.36  $\Omega$  under applied pressure of 5, 15 and 20 Pa, respectively (**Figure 49**). In addition, the  $\Delta R$  value has slightly reduced with decreases in curvature radius, and it was well recovered after bending (**Figure 50**). Moreover, aging data with bending cycle demonstrated that the durability of pressure sensor was maintained until 1,000 times (**Figure 51**). The initial  $\Delta R$  under applied 5 Pa of film was *ca.* 0.12, and 0.36  $\Omega$  after bending. It demonstrated that the durability of pressure sensor was maintained until 1,000 times. Judging from these results, it was evident that fabricated ZnO nanoneedle/PVDF film could be applied for the wearable and durable pressure sensor.

The different sensor performance between ZnO nanorod and nanoneedle would be attributed to the geometrical figures. Namely, the nanorod is c-axis grown hexagonal straight structure, whereas nanoneedle is closer to hexagonal vertical grown pyramid form, which causes the discrimination of piezoelectric effect ( $P_z$ ) (**Figure 52**). In general, the deflection ( $d_z$ ) of the ZnO generates a positive strain field ( $S_z$ ) with the stretched surface along the  $z$ -direction of electric field. The piezoelectric potential can be created by the relative displacement of the  $Zn^{2+}$  cations with respect to the  $O^{2-}$  anions, resultant in the wurtzite crystal structure. Therefore, these ionic charges can freely move and recombine with each other as releasing the strain. In our experiment, the top dimension of hexagonal ZnO nanorod and nanoneedle was *ca.* 6500 nm<sup>2</sup> and 1620 nm<sup>2</sup>, respectively, which led to different repulsive pressure under applied equal amount of force ( $6.5 \times 10^{-10}$  N). Most of all, the elastic modulus quantifying the resistance to elastic deformation for the ZnO nanorod/PVDF and nanoneedle/PVDF hybrid film was measured using the AFM nanoindentation, and the values were estimated to be *ca.* 25 and 3 GPa, respectively. Therefore, the ZnO nanoneedle has a better piezoelectric performance in comparison with the nanorod.

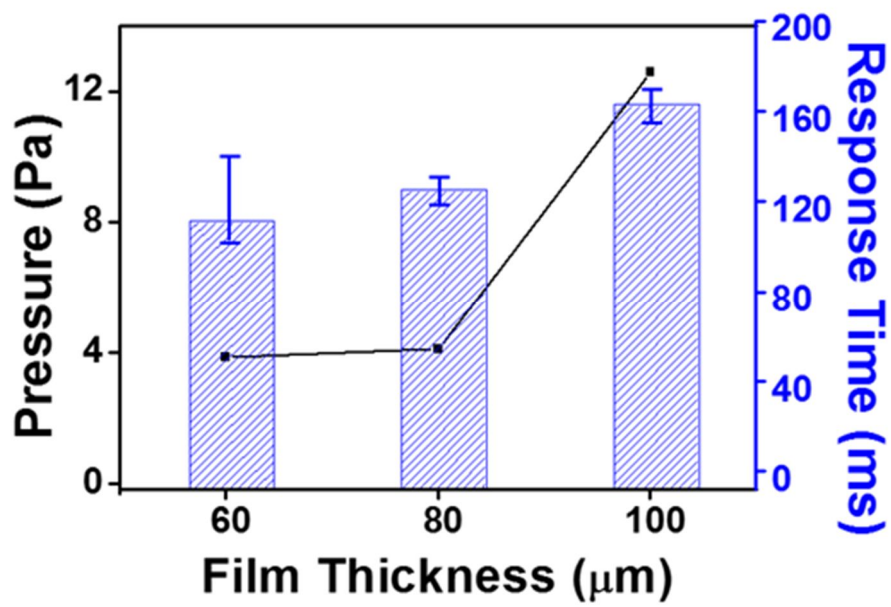


**Figure 46.** Minimum pressure detection limits and response time of ZnO nanoneedle/PVDF hybrid films as a function of film thickness.

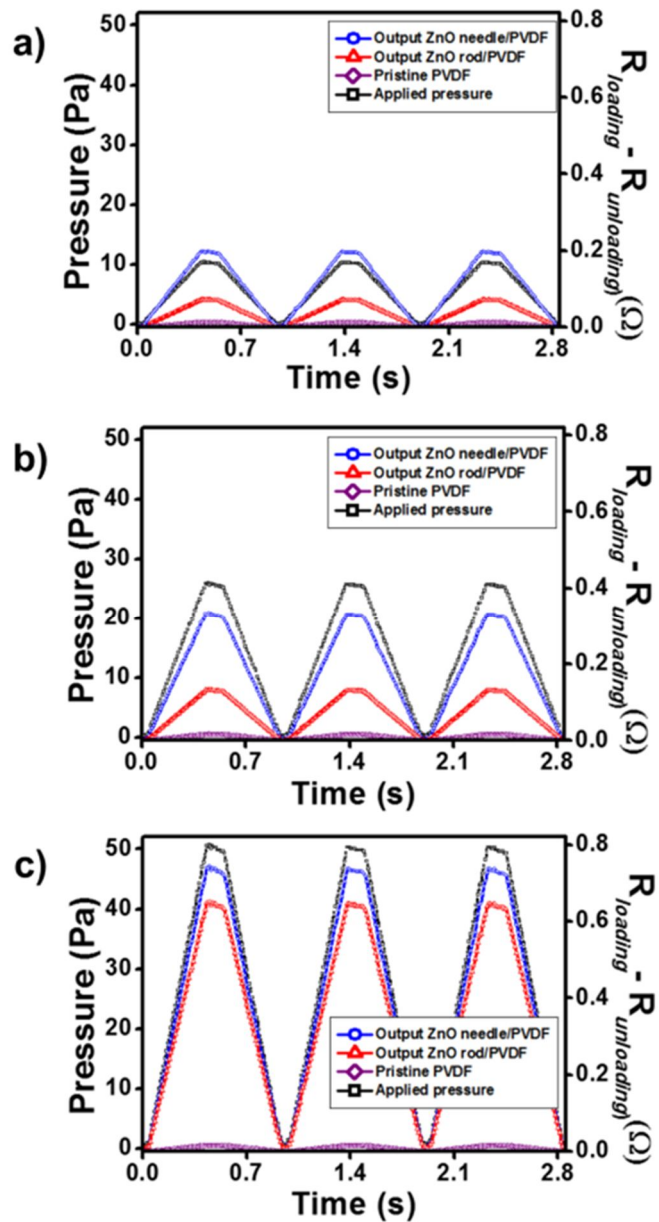


**Figure 47.** The change in resistance of pristine PVDF, ZnO rod/PVDF and ZnO needle/PVDF hybrid film-based pressure sensor according to the applied pressure of (a) 10 Pa, (b) 25 Pa and (c) 50 Pa.

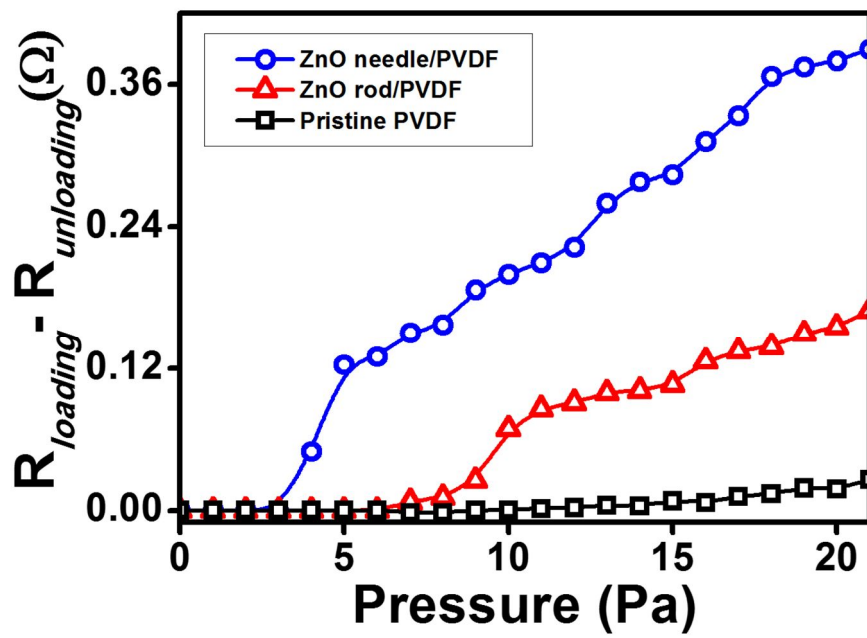


**Figure 48.** The sensitivity of three different pressure sensors with pristine PVDF, ZnO rod and ZnO needle.

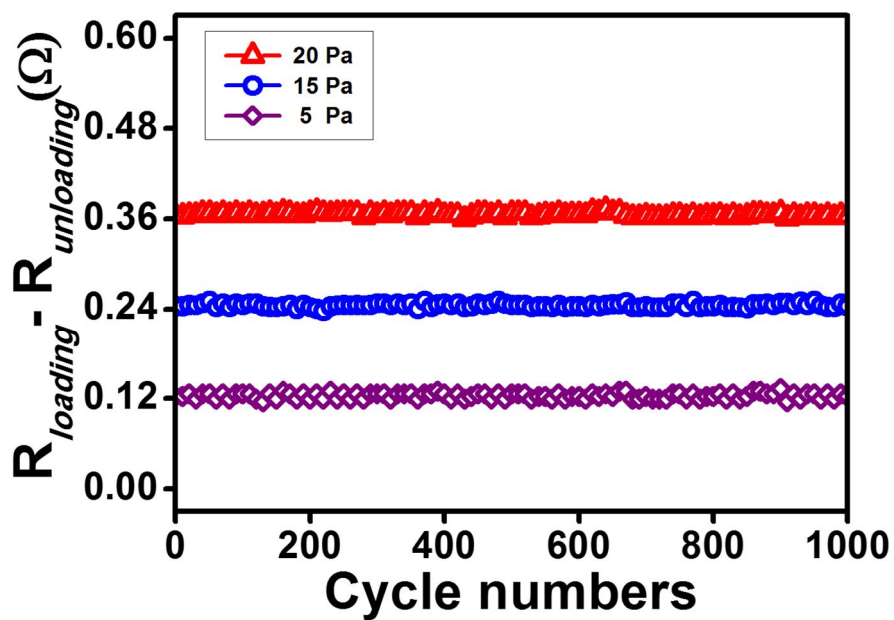


**Figure 49.** Multiple-cycle test of ZnO needle/PVDF film-based pressure sensor with repeated loading-unloading of pressure in the range of 5, 15 and 30 Pa.

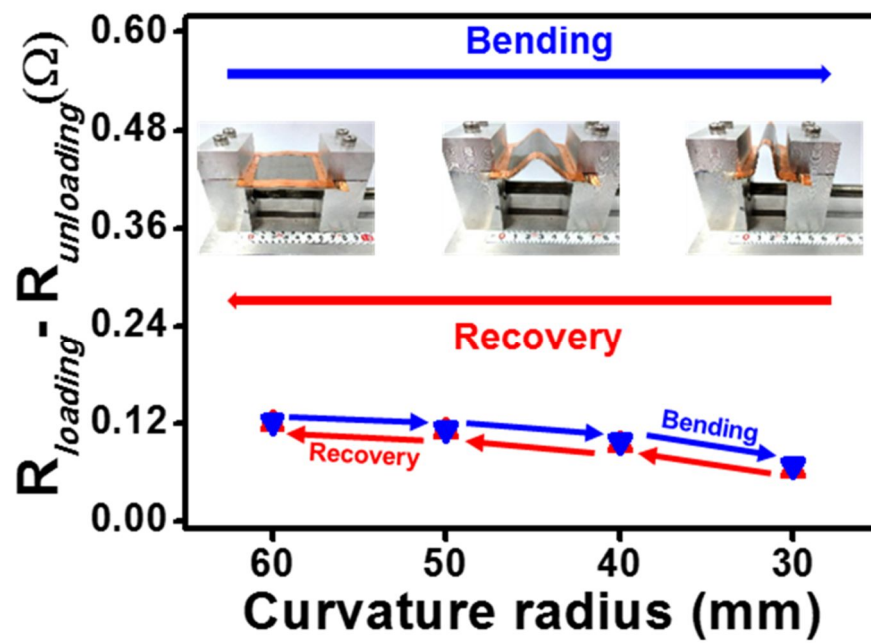


**Figure 50.** Resistance changes of ZnO needle/PVDF film-based pressure sensor with different curvature radius under constant applied pressure, 5 Pa

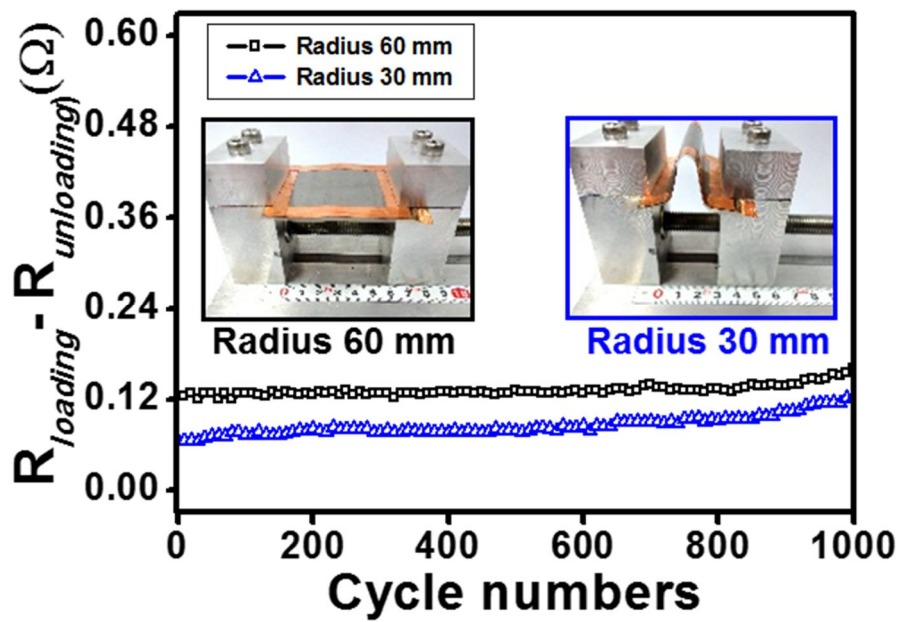


**Figure 51.** Aging bending cycle test of ZnO needle/PVDF film-based pressure sensor under constant applied pressure of 5 Pa

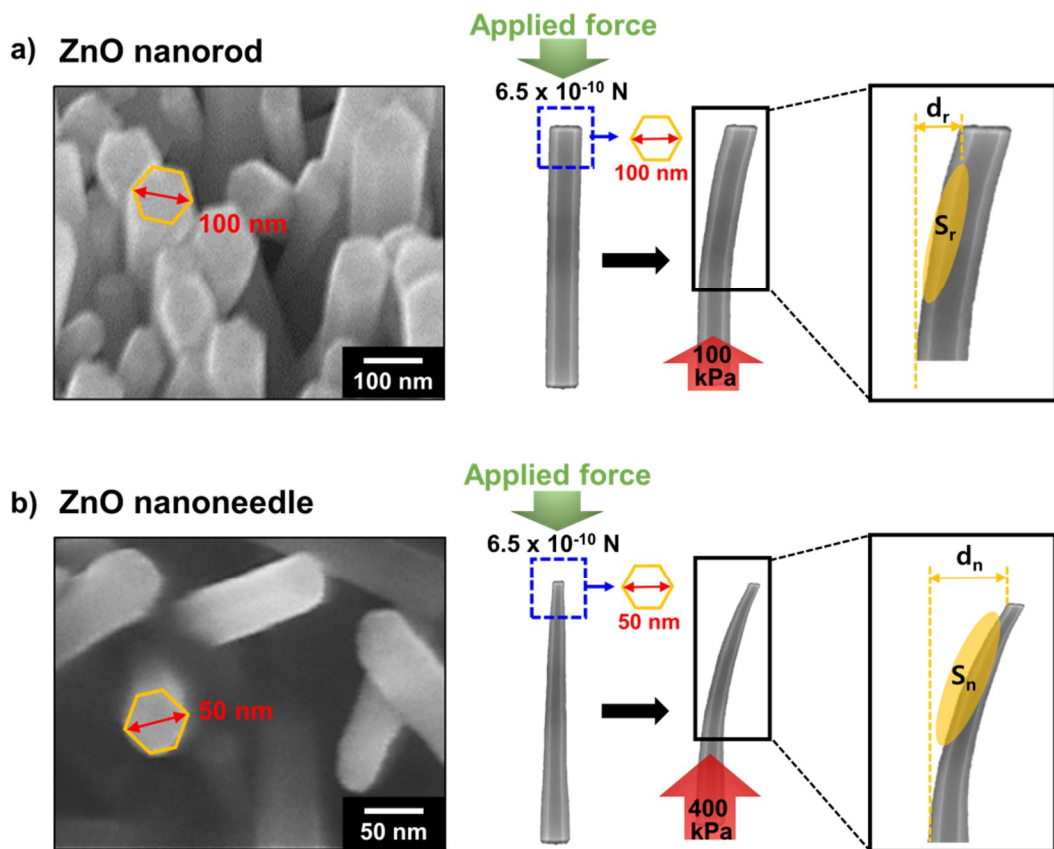


**Figure 52.** High magnification of SEM images and the discrimination of strain field under identical applied force for ZnO (a) nanorod and (b) nanoneedle.

On the basis of the above analysis, we have demonstrated for the first time that the ZnO nanoneedle/PVDF hybrid thin film was able to be applied for a wearable and wireless pressure sensor to monitor the heart rate. The physical pressure of a pulse was measured in real time after attaching the sensor directly onto a neck over the carotid artery and wrist, where the radial artery is closest to the surface, and we could monitor the heart rate via smart phone screen (**Figure 53**). The normal pulse was *ca.* 88 bpm whereas post-exercise (cycle pedaling) was *ca.* 121 bpm. As a result, the normal and post-exercise heart beat was measured more sensitively on the radial artery owing to the relatively thin scarfskin, which could deliver the more intense pressure on the device. The received wireless pulse signal showed the similar heart rate oscillation compared to the wire pressure sensor (**Figure 54**). Especially, the ability to detect a real-time pulse was evaluated by changing of pulse during cycle pedaling (**Figure 55**). As a result, the intensity and frequency of pulse signal has increased after pedaling, and it has stabilized to the normal pulse when finished. In addition, the response time and signal strength indicator (RSSI) of the wireless pressure sensor are analyzed according to the distance between Bluetooth transmitter and smartphone (**Figure 56**). As a result, the Bluetooth transmitter could transmit the pulse signal to smart phone within a distance of 8 m without distortion and time delay.

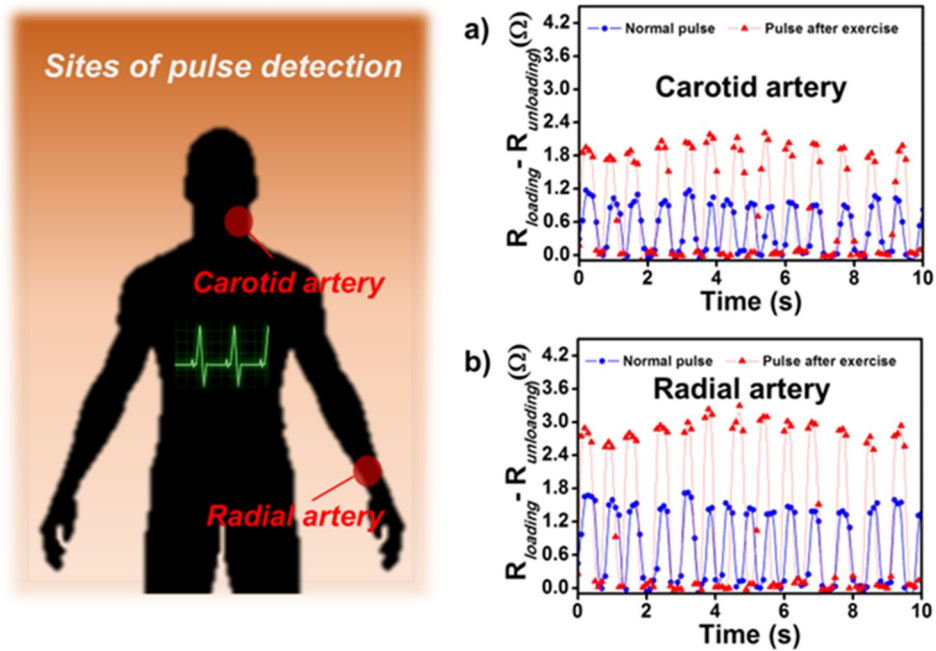


**Figure 53.** The difference in the electrical resistance of ZnO needle/PVDF film-based wireless pressure sensor as a function of time for measuring the pulse on the (a) carotid artery and the (b) radial artery of a human object. For the normal pulse, the heart rate was recorded as 88 bpm for 10 s, and 121 bpm after exercise.

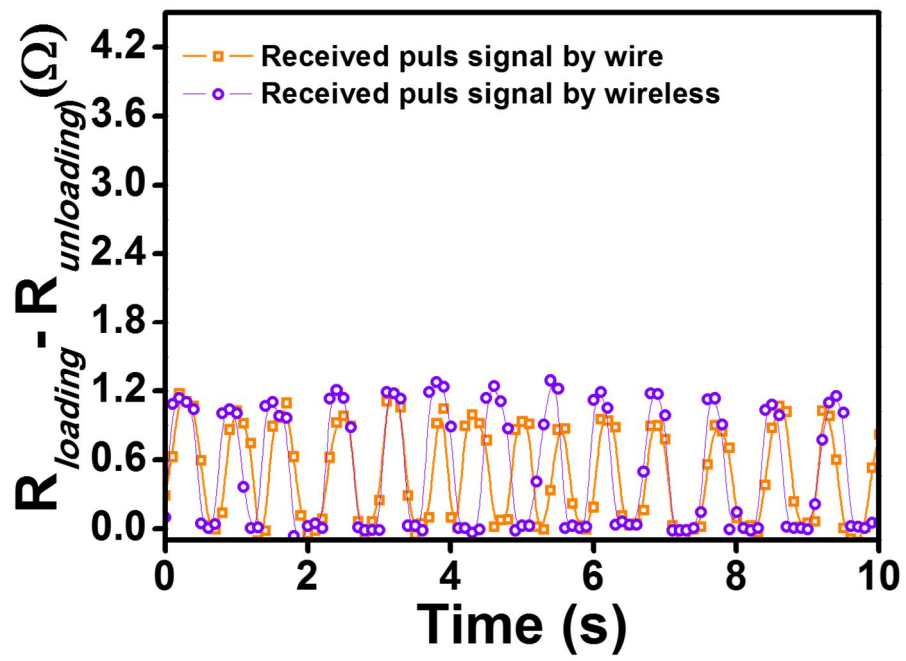


**Figure 54.** Comparing measured difference in the electrical resistance of pulse signal that received by wire and wireless sensor using ZnO needle/PVDF film.

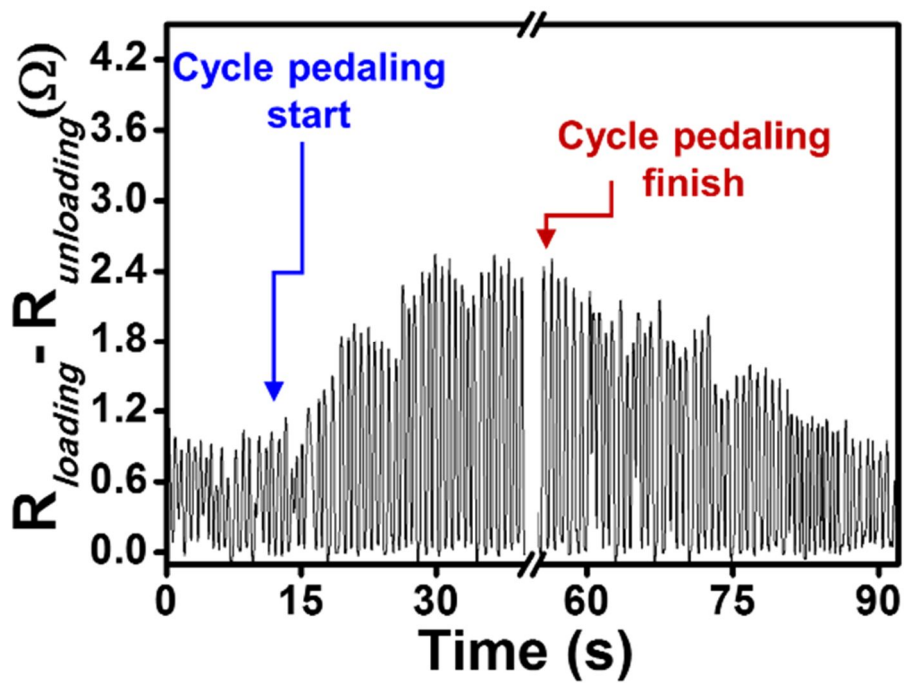


**Figure 55.** The sensor patched on wrist and the changing of pulse was monitored during cycle pedaling, and the speed of pedaling was maintained *ca.* 17 km/h for 45 s.

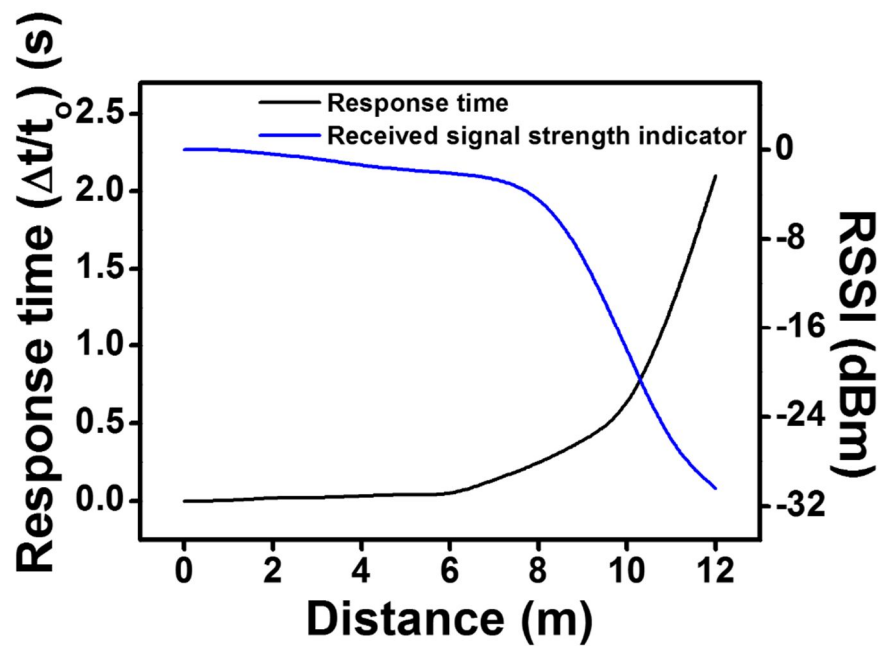


**Figure 56.** The respond time and RSSI of the wireless pressure sensor according to the distance between Bluetooth transmitter and smartphone.

### 3.3. Fabrication of PVDF Thin Film with Urchin-like ZnO for Acoustic Acuator

#### 3.3.1. Fabrication of PVDF thin film with urchin-like ZnO

The SEM images reveal that the urchin-like ZnO is composed of several *ca.* 400 nm nanospikes extending from the core with the overall size of *ca.* 1  $\mu\text{m}$  (**Figure 57a**). Whereas, rod-like ZnO had the hexagonal base diameter of *ca.* 85 nm with the length of *ca.* 300 nm (**Figure 57b**). The XRD analysis for the fabricated ZnO indicates that all of the diffraction peaks can be exactly indexed to the hexagonal ZnO with lattice constant  $c = 0.52$  nm, which is in good alignment of the ZnO along the c-axis direction. Seemingly, urchin-like ZnO should favor (101) XRD characteristic peak over ZnO rod. Nevertheless, as in **Figure 58**, the observed XRD peaks of rod-like ZnO had the greater intensity, it may have arise as shown in **Figure 59**. Furthermore, repeated XRD analysis results show a small variation in (101) peak, which results from the randomly orientated rod-like ZnO powder.

The polarized optical microscopy (POM) morphology of the crystal growth shows that the amount of spherulites has significantly increased with the addition of ZnO nanofillers, which means that added ZnO nanofillers act as nucleation sites for the PVDF crystallization (**Figure 60**). Furthermore, it can be inferred that the reinforced crystallization behavior is intimately

proportional to the  $\beta$  phase content. Consequently, increasing the deflected spikes of ZnO enhanced the piezoelectric potentials because partial polarizations which positive (outer stretched surface) and negative (inner compressed surface) potential induces the  $\beta$  phase PVDF, which also contributed to elevating the permittivity (**Figure 61**). To achieve in depth insight into the crystallization behavior by ZnO nanofillers in PVDF matrix, FTIR spectra of various PVDF films of urchin-like ZnO embedded, rod-like ZnO embedded, the homemade pristine PVDF, and commercial PVDF films were carried out (**Figure 62**). In additionally, differential scanning calorimetry (DSC) that crystallinity of PVDF is most rapidly formed with urchin-like ZnO. Especially, ZnO urchin shows the highest crystallization rate constant ( $k$ ),  $6.654 \times 10^{-6}$ , values of Ozawa exponent ( $n$ ), 3.114 and reaching half-time crystallinity ( $t_{1/2}$ ), 1.484 min (**Figure 63 and Table 5**). Among different crystalline phases of PVDF, the  $\beta$  phase exhibits piezoelectric and pyroelectric properties due to its large spontaneous polarization, arising from the aligned molecular chain configuration<sup>[14]</sup>. The representative peak of the  $\alpha$  phase, trans-gauche conformation, appeared at  $766 \text{ cm}^{-1}$ , while the  $\beta$  phase peak, all trans planar zigzag conformation, appeared at  $840 \text{ cm}^{-1}$ . The relative intensity of representative  $\alpha$  and  $\beta$  phase peaks were then calculated in order to calculate the  $\beta$  phase content in the film, using Lambert-Beer law<sup>[15]</sup>.

As a result, the urchin-like ZnO embedded PVDF film had a relative intensity of  $\beta$  and  $\alpha$  phase ( $I_{\beta}/I_{\alpha}$  ratio) of 5.74 with 88 %  $\beta$  phase, and incorporating rod-like ZnO led to the ratio of 4.31 with 84 %  $\beta$  phase. This is 18 % and 40 % enhancement with the incorporation of urchin-like ZnO in PVDF matrix compared to the homemade PVDF film and commercial PVDF film, respectively. Whereas the use of rod-like ZnO nanofillers has shown 12 % and 36 % enhancement with respect to the homemade PVDF and commercial PVDF films (**Table 6**). Judging from these results, the introduction of ZnO nanofillers into the PVDF matrix has successfully increased the  $\beta$  phase content.

The enhanced permittivity, which is related to the polarization and dipole moment of PVDF, is the key factor for improving the piezoelectric property of PVDF. For this reason, the addition of ZnO nanofillers with high dielectric constant into the PVDF matrix makes it possible to enhance the permittivity of PVDF (**Figure 64**). The fitting lines were obtained based on Cole-Cole equation below<sup>[16]</sup>.

$$\varepsilon^* = \varepsilon' + i\varepsilon'' = \varepsilon_{\infty} + \frac{\Delta\varepsilon}{\{1+(i\omega\lambda)^{1-\alpha}\}^{\beta}}$$

Where  $\varepsilon'$  is the dielectric constant,  $\varepsilon''$  is the dielectric loss; the permittivity is therefore given by

$$\Delta\varepsilon = \varepsilon_s - \varepsilon_{\infty}$$

where  $\varepsilon_s$  is the static permittivity (i.e., when  $\lim_{\omega \rightarrow 0} \varepsilon^*(\omega)$ ), and  $\varepsilon_\infty$  is the high-frequency permittivity (i.e., when  $\lim_{\omega \rightarrow \infty} \varepsilon^*(\omega)$ ).

In addition, Cole-Cole fitting curve is a particular case of the Havriliak-Negami relaxation and the equation is follow:

$$\varepsilon^* = \varepsilon_\infty + \frac{\Delta\varepsilon}{1+(i\omega\lambda)^{1-\alpha}} \quad (0 \leq \alpha < 1)$$

where  $\Delta\varepsilon$  is associated with the electrostatic interaction between the dielectric materials. Also, the relaxation time ( $\lambda$ ) is correlated with the proper interfacial polarization response and is related to the maximum value of dielectric loss ( $\varepsilon''$ ). The all measured permittivities are listed in **Table 6**.

The deflection of the ZnO generates a positive strain field on the stretched surface along the z-direction of the electric field. The piezoelectric potential of ZnO with wurtzite crystal structure can be created by the relative displacement of the  $\text{Zn}^{2+}$  cations with respect to the  $\text{O}^{2-}$  anions, upon a mechanical stress. Therefore, these ionic charges can freely move and recombine with each other as releasing the strain. The urchin-like ZnO embedded PVDF film showed the greatest enhancement in the permittivity. It is generally accepted that the dielectric property of composites is strongly influenced by the interfacial region. From our previous work by Lee et al., we have proved the interfacial polarization in rod or disk ZnO nanostructure and PVDF composites attribute to the higher dielectric constant of their composites.

Therefore, the increase in the permittivity could be explained by two factors: the added current paths of nanospike-to-nanospike contacts among adjacent urchin-like ZnO nanofillers and high surface area per structure of the urchin-like ZnO and PVDF. It is known that a larger aspect ratio of a polarizable material leads to a greater dielectric constant. Each nanospike extending from the core, forming an urchin-like structure, has a larger aspect ratio compared to the rod-like ZnO, and its 3-dimensional structure induces greater non-uniform electric dipole moments upon an external electric field, leading to a greater polarization and thus a greater dielectric constant. Also, the added current paths can facilitate the transport of charges by transforming the arrangement of charges. In addition, due to the especial hierarchical structure of urchin-like ZnO, a lot of empty space between adjacent fillers and consequently a considerably larger surface area is conceivable compared to the closely-packed rod-like ZnO. Consequently, the added nanospike-to-nanospike current paths and increased surface area arising from the 3-dimensional hierarchical structure of urchin-like ZnO contributed to uplifting the permittivity

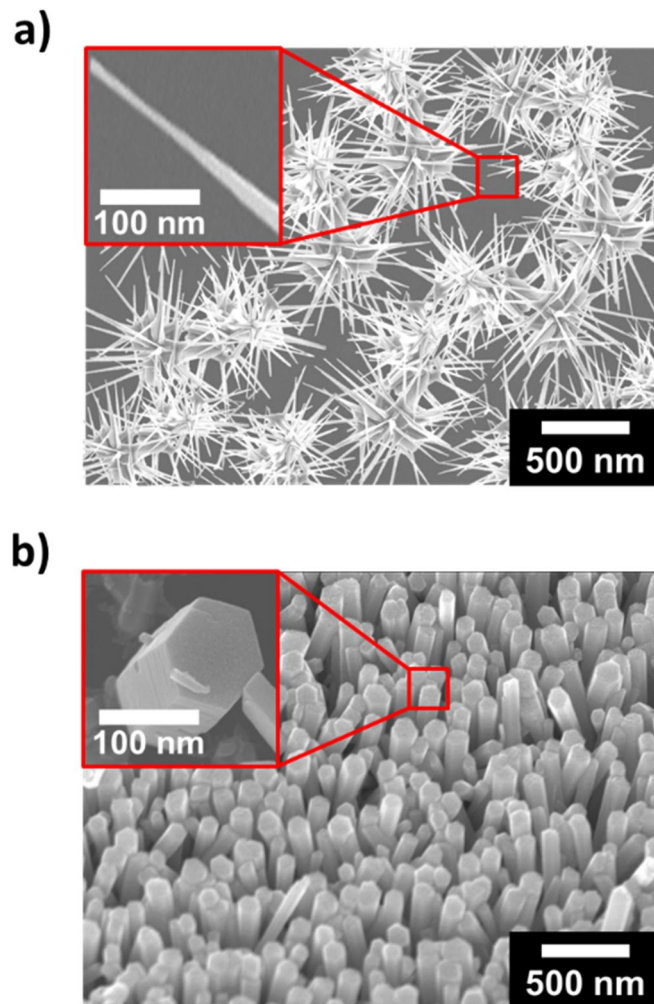


**Figure 57.** Low and high magnification of SEM images for the fabricated (a) urchin-like (b) rod-like ZnO.

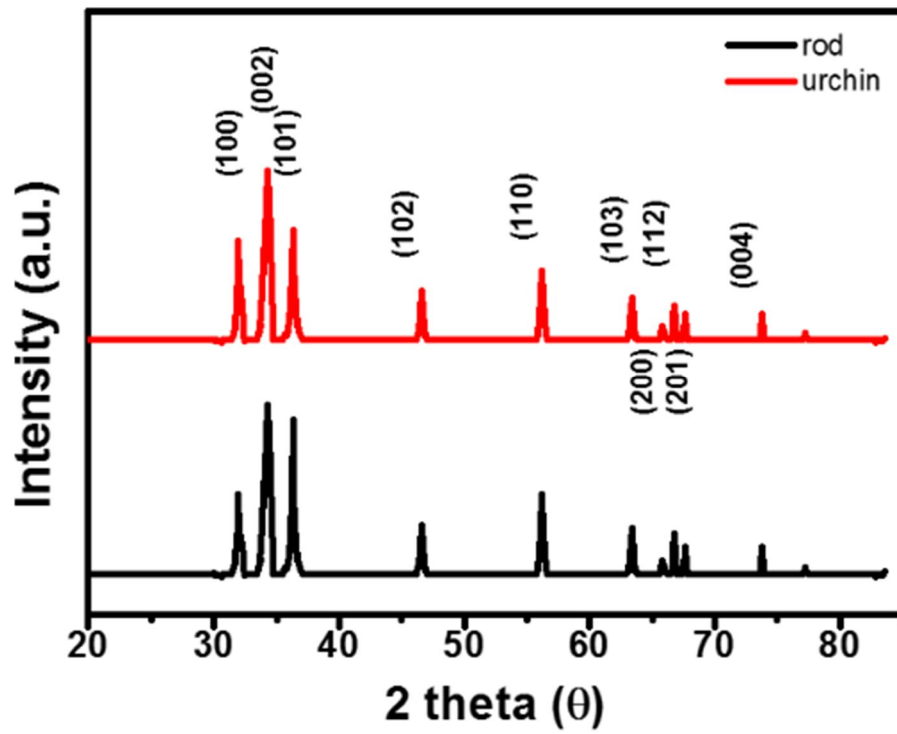


**Figure 58.** XRD patterns to investigate the crystal structure of the ZnO nanofillers.

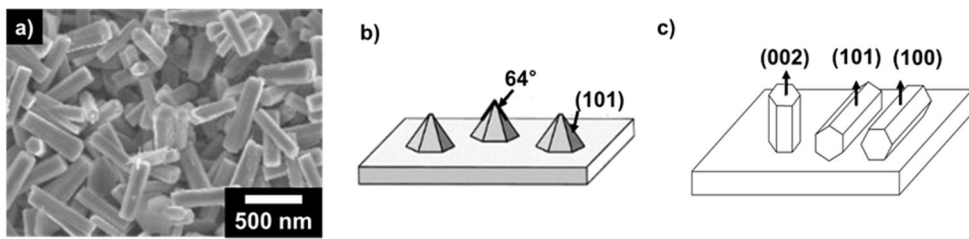


**Figure 59.** (a) SEM image of ZnO rod power, and several crystal plan sketch of ZnO (b and c).

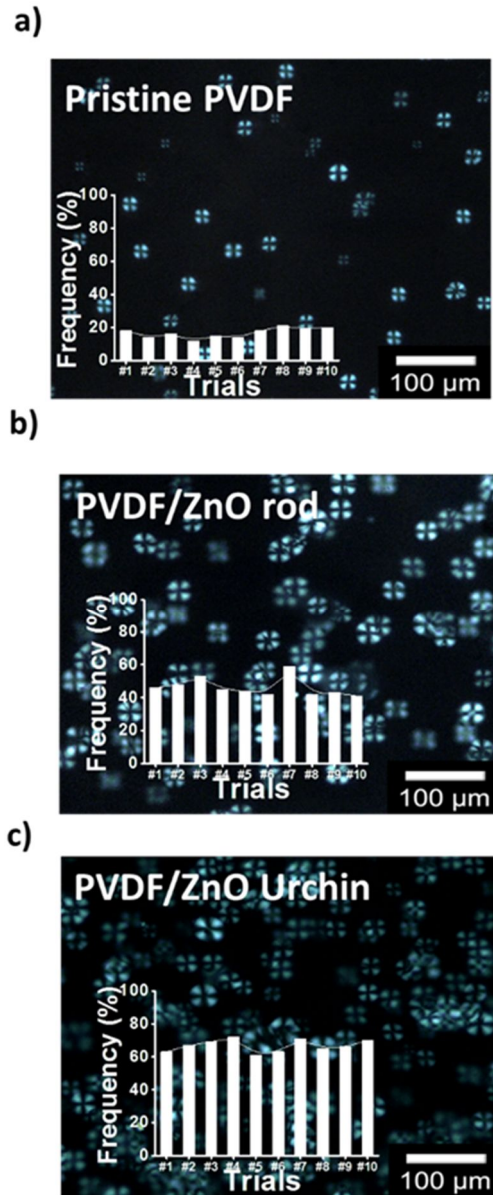


**Figure 60.** Polarized optical microscopy images of (a) Pristine PVDF film, PVDF hybrid films with (b) rod-like ZnO and (c) urchin-like ZnO by isothermally crystallized at 170 °C and maintained for 240 s then cooled down to room temperature to observe the crystal growth morphology.

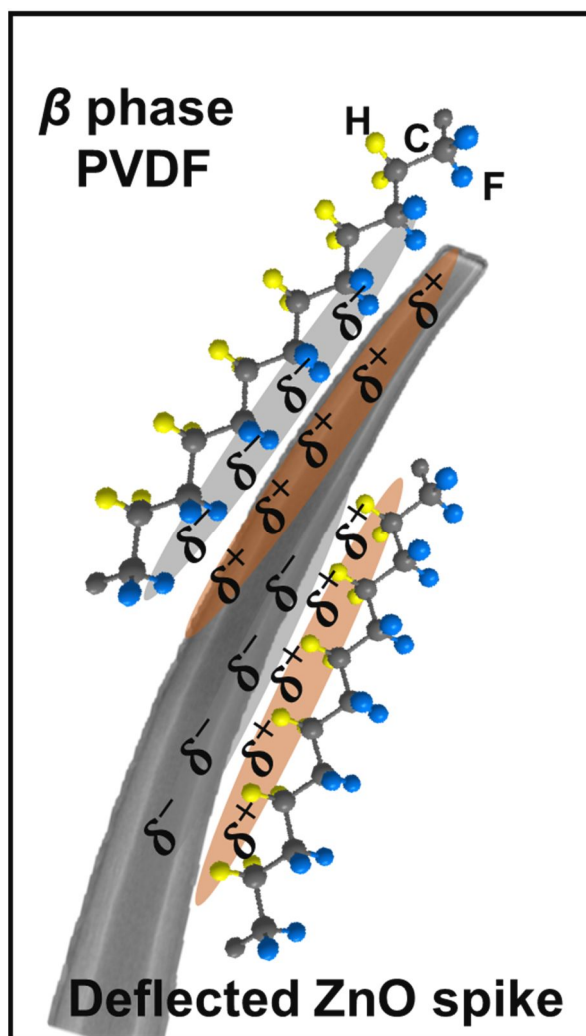


**Figure 61.** Polarized optical microscopy images of (a) Pristine PVDF film, PVDF hybrid films with (b) rod-like ZnO and (c) urchin-like ZnO by isothermally crystallized at 170 °C and maintained for 240 s then cooled down to room temperature to observe the crystal growth morphology.

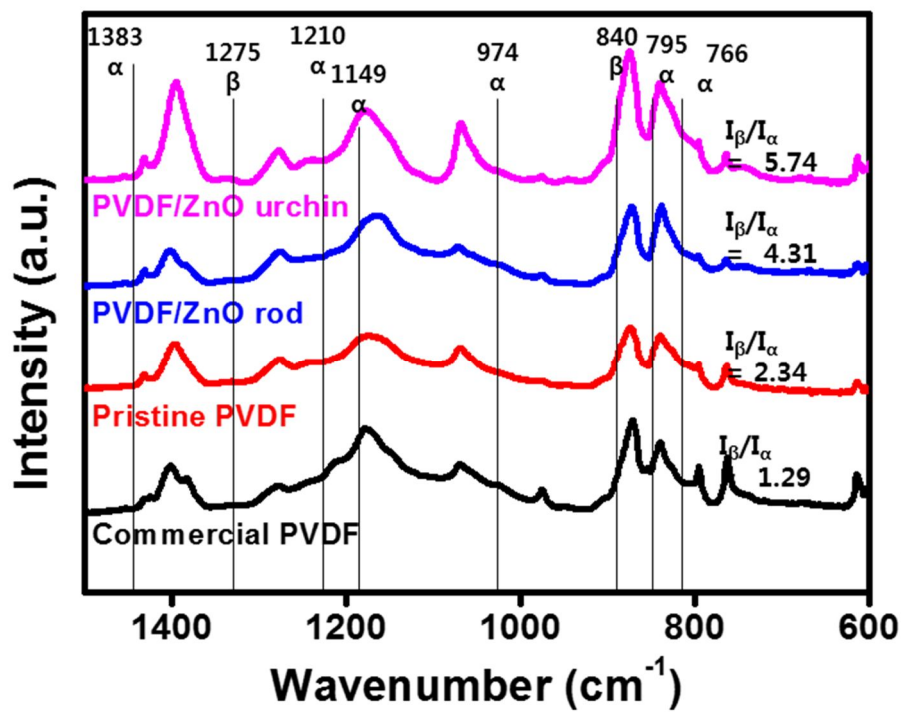


**Figure 62.** IR spectrum of pristine PVDF films and ZnO embedded PVDF hybrid films.

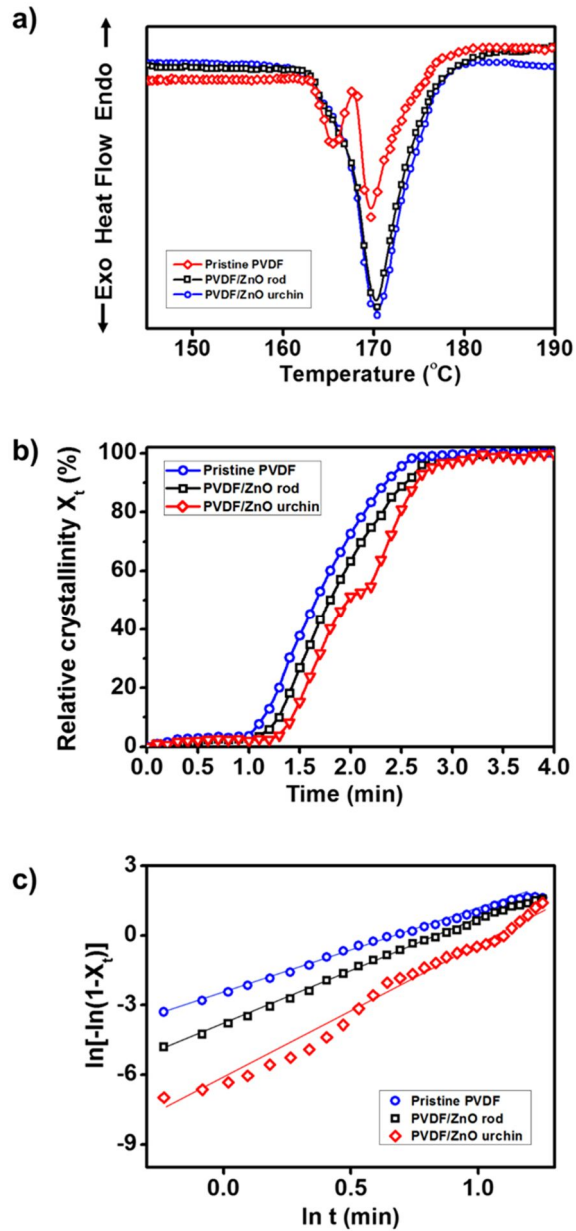


**Figure 63.** a) DSC thermograms of pristine PVDF and PVDF/ZnO hybrid films that cooled from 190 °C at a cooling rate of 10°C/min, b) Relative crystallinity as a function of time, and c) plot of  $\ln[-\ln(1-X_t)]$  versus  $\ln t$  for thermal behavior parameters.

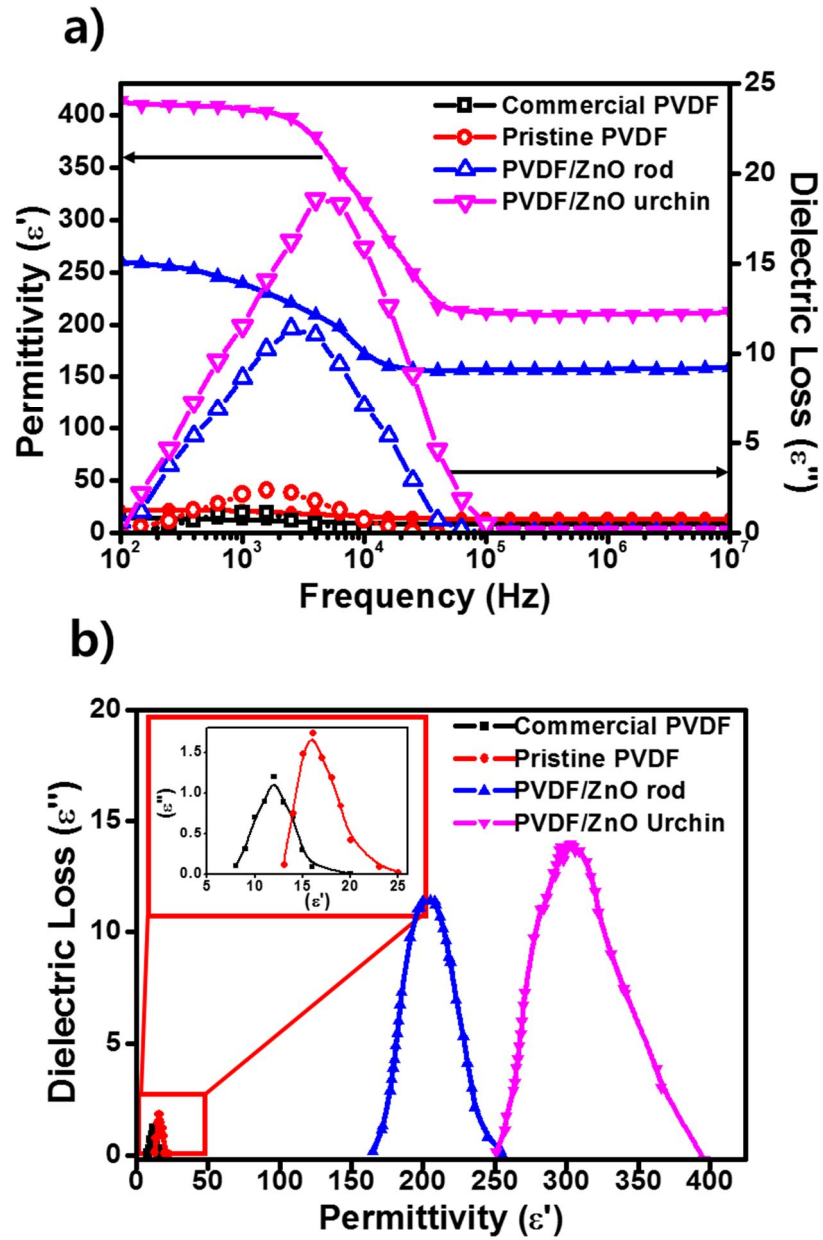


**Figure 64.** (a) Permittivity and loss factor of the fabricated thin films and (b) Cole-Cole fitting curves by permittivity versus dielectric loss.

**Table 5.** Values of  $n$ ,  $k$  and  $t_{1/2}$  for pristine PVDF and PVDF/ZnO hybrid film

| Sample          | $n^a$ | $k^a$                    | $t_{1/2}$ (min) <sup>a</sup> | T <sub>c</sub> <sup>a</sup> (°C) | T <sub>c</sub> <sup>β</sup> (°C) |
|-----------------|-------|--------------------------|------------------------------|----------------------------------|----------------------------------|
| Pristine PVDF   | 6.214 | 0.630 x 10 <sup>-6</sup> | 2.412                        | 167.21                           | 169.98                           |
| PVDF/ZnO rod    | 4.081 | 5.012 x 10 <sup>-6</sup> | 1.504                        |                                  | 170.01                           |
| PVDF/ZnO urchin | 3.114 | 6.654 x 10 <sup>-6</sup> | 1.484                        | -                                | 170.02                           |

<sup>a</sup> These values were obtained by Ozawa analysis of samples using DSC.

**Table 6.** The values of  $\beta$  content and dielectric parameters of the commercial, pristine PVDF and ZnO/PVDF hybrid films.

| Sample          | $F(\beta)^a$ | $\epsilon_S$ | $\epsilon_\infty$ | $\Delta\epsilon^b$ | $\lambda$ ( $\mu\text{s}$ ) <sup>c</sup> |
|-----------------|--------------|--------------|-------------------|--------------------|------------------------------------------|
| PVDF/ZnO urchin | 88           | 414          | 211               | 203                | 101                                      |
| PVDF/ZnO rod    | 84           | 260          | 157               | 103                | 120                                      |
| Pristine PVDF   | 74           | 22           | 13                | 9                  | 157                                      |
| Commercial PVDF | 62           | 21           | 13                | 8                  | 158                                      |

<sup>a</sup> Data calculated using Lambert-Beer law.

<sup>b</sup> Data calculated using Havriliak-Negami and Fourier transform relationship.

<sup>c</sup> Data were obtained via the interfacial polarization response relaxation time.

### 3.3.2. Acoustic generator and receiver.

Frist, urchin-like ZnO and rod-like ZnO were synthesized by chemical vapor deposition method and hydrothermal method, respectively [101-105]. The prepared ZnO was mixed a PVDF solution, which was then drop casted to form a ZnO/PVDF mat. The ZnO/PVDF films were drawn at an elevated temperature and polled under a strong constant electric field at 30 kV/mm to transform the  $\alpha$  phase to  $\beta$  phase. The setup for poling process under constant electric fields, the high voltage power supply which is connected in series with the fabricated film and with an oscilloscope for measuring the poling current using an additional resistor in the electrical circuit. The resultant film was transparent and polarized. Subsequently, an acoustic actuator electrode was fabricated with few layered *ca.* 2 nm thick graphene, which was synthesized by chemical vapor deposition method. Prior to applying graphene as an electrode, the fabricated ZnO/PVDF film surface was treated with 3-aminopropyltriethoxysilane (APS) to improve adhesion with graphene. Hence, a sandwich of the ZnO/PVDF hybrid film and graphene electrodes was prepared as an acoustic actuator, which was connected to a sound source and amplifier. As schematically illustrated in Figure 65a, the interaction between each nanospike on ZnO fillers generates the deflection ( $d_z$ ) of ZnO and a positive strain field ( $S_z$ ) with the stretched surface along the z-direction which

induces the piezoelectric effect ( $P_z$ ),  $P_z = S_z/C$ , where  $C$  is the piezoelectric effect coefficient along the positive  $z$ -axis of ZnO. Therefore, the ZnO fillers can enhance the piezoelectricity of the hybrid film, and it makes possible to fabricate a PVDF based acoustic actuator with graphene electrodes (Figure 65b). From our previous work by Lee et al., we have discovered that the electrode conductivity greatly influenced acoustic actuator performance, in midrange and treble regions. Compared to the commercial thin film loudspeaker which uses PEDOT:PSS electrode, using chemical vapor deposition (CVD) grown graphene electrodes increased the frequency response in midrange and treble by 19 % and 22 %, respectively. TEM image (Figure 66a) reveals CVD graphene with few layers and Raman spectroscopy unveils a graphitic structure with the ration of  $I_G/I_{2D}$  of *ca.* 2 (Figure 66a inset). An atomic force microscopy result exhibit a 2 nm multilayered graphene (Figure 66b).

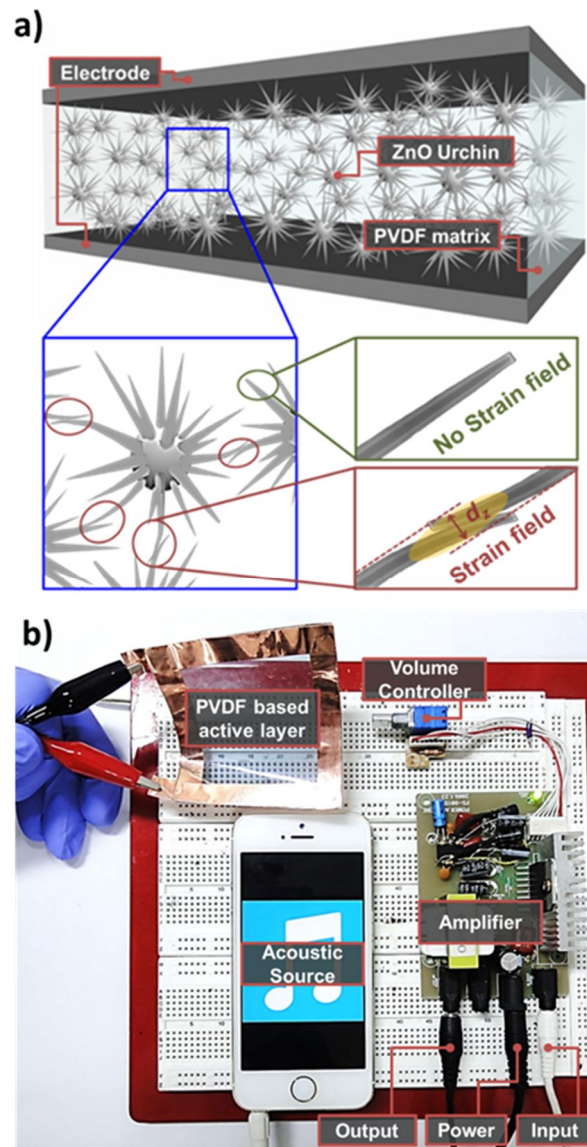


**Figure 65.** (a) A schematic illustration of the structural and interphase mechanism with fillers and (b) a photograph of the hybrid thin film loudspeaker consisting of ZnO/PVDF or pristine PVDF with graphene electrodes.

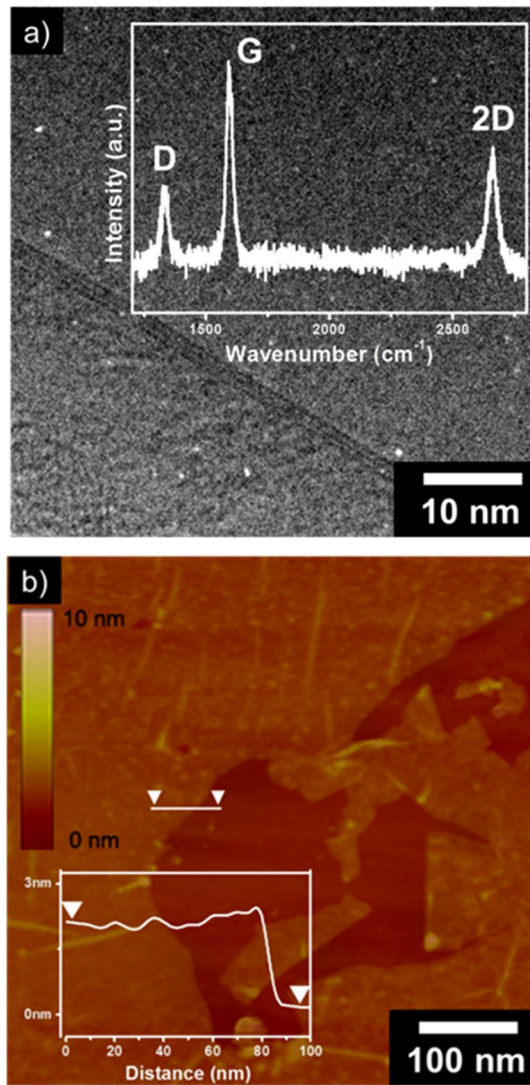


**Figure 66.** (a) HR-TEM (inset: Raman spectrum) and (b) AFM of the fabricated graphene electrode.

**Figure 67a** illustrates the piezoelectric acoustic generator performance of various fabricated PVDF films as a function of frequency. Notably, the urchin-like ZnO embedded PVDF film showed the greatest improvement in all measured frequency regions: approximately 29 dB full-scale (72 %) increase in the low bass region (below 100 Hz). From our previous study with the Ba-doped SiO<sub>2</sub>/TiO<sub>2</sub> nanoparticles embedded PVDF film, the overall frequency response at low frequency was limited to above 200 Hz. However, with the introduction of urchin-like ZnO, the bass frequency response significantly improved. In addition, the total harmonic distortion in the bass region decreased by 82 % (**Figure 67b**). We suggest that this significant enhancement is due to the increased dielectric constant and enhanced crystallinity of PVDF because of the space charge interaction between the PVDF interfaces with embedded ZnO nanofillers. The improved midrange and treble frequency response is due to a decreased sheet resistance by replacing PEDOT:PSS electrode with graphene electrode and by embedding urchin-like ZnO which has added nanospike-to-nanospike current paths (**Figure 68**). This result implies that the fabricated urchin-like ZnO embedded PVDF film had the significant enhancement as the thin film acoustic actuator for the maximum sound with controlled acoustic distortion. Importantly, not only the high  $\beta$  phase content but also the added nanospike-to-nanospike current paths play a

key role in the improvement for the acoustic actuator. With more number of current paths present in the film, more electrons are transferred to the surface of ZnO which gets transformed to the vibrational force, generating more stable sound. The cyclic stability of urchin-like ZnO morphology be examined. **Figure 69a** reveals the initial condition of urchin-like ZnO SEM image. First of all, this pristine urchin-like ZnO was modified to fabricate PVDF based hybrid film. After then, the film was utilized as a sound generator for 240 h continually. The played acoustic source was “Billie Jean” by Michael Jackson and the output sound was maintained for -12 dBV. Afterwards, a part of hybrid PVDF film was dissolved again in dimethylformamide (DMF) and the mixture is centrifuged in order to collect after-used urchin-like ZnO fillers. As a result, the visible morphology after-used ZnO seems not damaged nor distorted compared to the pristine urchin-like ZnO (**Figure 69b**). Moreover, XRD patterns shows identical peaks of urchin-like ZnO filler (**Figure 69c**). Additionally, the acoustic performance of tested hybrid film was compared to the initial condition of hybrid PVDF film (**Figure 69d**). Consequently, it was confirmed that the durability of urchin-like ZnO and hybrid PVDF film is very stable at least 240 working hours. **Figure 70** shows the frequency response of the film as a function of the film thickness. The output sound level of 60  $\mu\text{m}$  film decreased at low frequency range because of a relatively low

piezoelectricity, and acoustic performance of 100  $\mu\text{m}$  film showed the decreased frequency response in midrange and treble ranges since the thick and heavy surface of the film obstruct the vibration of the film surface to generate an acoustic signal. **Figure 71** illustrates the acoustic performance as a function of urchin-like ZnO filler contents. Loading ZnO filler enhanced the frequency response at the bass frequency range up until 30 wt%. However, exceeding the optimal filler concentration might have caused an aggregation of fillers and thus reduced sound level. Therefore, it showed a clear evidence that the 80  $\mu\text{m}$  thick PVDF film with 30 wt% of ZnO urchin filler is optimum for the thin film piezoelectric acoustic generator for the maximum sound performance as represented by the enhanced frequency response with stable distortion. Since the fabricated urchin-like ZnO/PVDF hybrid film showed great piezoelectricity (piezoresistive or reverse-piezoelectricity), it makes possible to measure the acoustic receiving  $\Delta R/R_0-t$  signals (**Figure 72**) presented distinct patterns when the speaker spoke different words and phrases such as “Scientist”, “Acoustic actuator”, “Seoul National University”, and “I love sunny days”, a uniform signal of 55 dB of 500 Hz (**Figure 73a and b**). The use of the composite film in microphone is completed by analyzing piezoresistive signal on the device surface, which the input signal is surface pressure originated from sound pressure in air medium. Vocal experiment was done as described in the journal:

a uniform signal of 55 dB of 500 Hz was played 10 cm away from the device. Large sound intensity demonstrates large sound pressure on the device, resulting from the high air pressure on the active film. Therefore, as the reviewer mentioned, the high intensity of the sound (high dB) increases the piezoresistance and thus more distinctive peak. However, experimental data suggests the intensity over 90 dB resulted in high peak noise and the intensity below 15 dB did not convey enough sound pressure to the device. To further investigate repeatability, the word “Scientist” and “I love sunny days” were recorded for three times each (Figure 73c and d). Measured  $\Delta R/R_0-t$  presented very similar profiles, including highlighted characteristic peaks and curves in the same word and phrases. These are mainly caused by the applied sound pressure and sound wave with different energy level of frequency while speaking. As a result, the urchin-like ZnO/PVDF hybrid film may provide a promising and effective method for voice recognition and receiver.

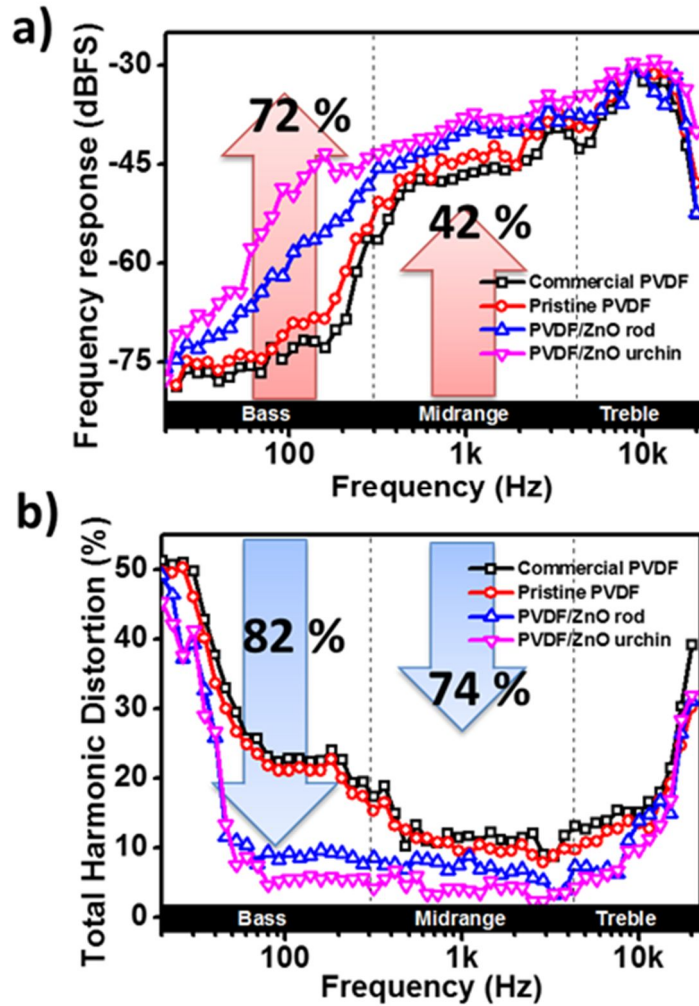


**Figure 67.** (a) The frequency responses and (b) total harmonic distortion of different PVDF-based thin film loudspeakers. (c) The frequency response as a function of the film thickness. (d) Relative efficiency of the actuators performance compare to the pristine PVDF acoustic actuator at 100 Hz as a function of the filler content.

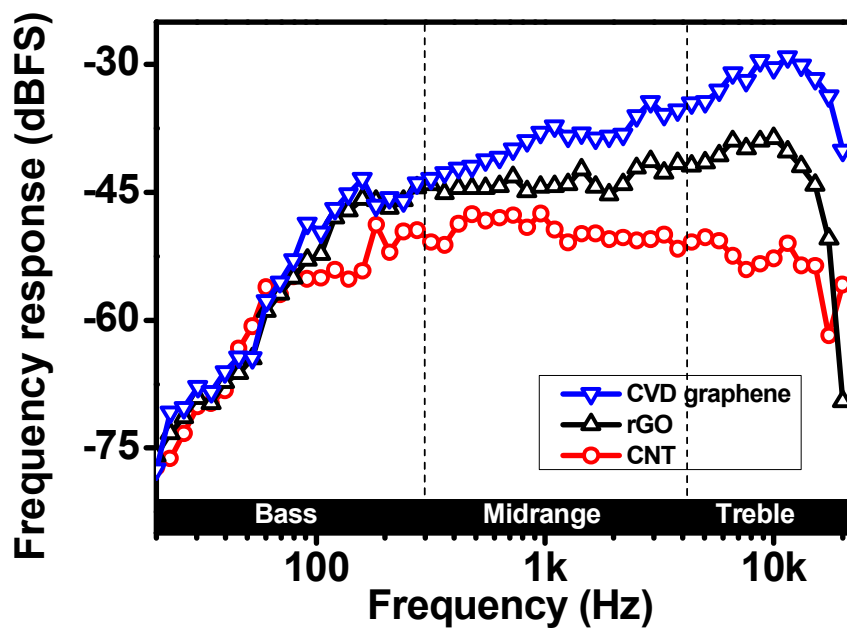


**Figure 68.** The frequency responses of PVDF/ZnO urchin-based thin film acoustic actuators with CVD graphene, rGO and CNT electrodes.

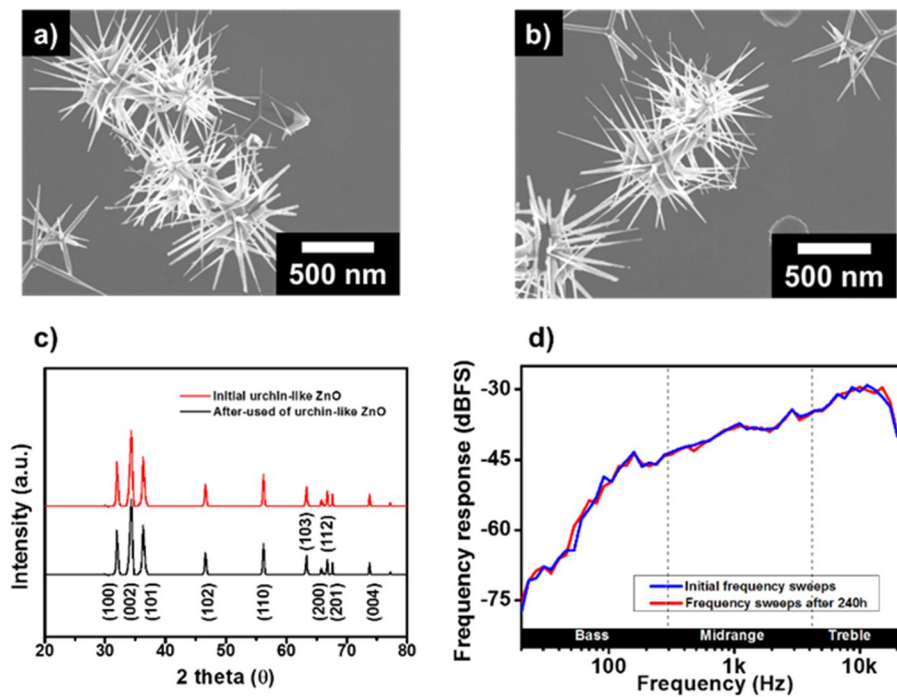


**Figure 69.** Initial condition and after-used condition of urchin-like ZnO SEM images (a and b). Comparing c) XRD patterns and d) frequency response.

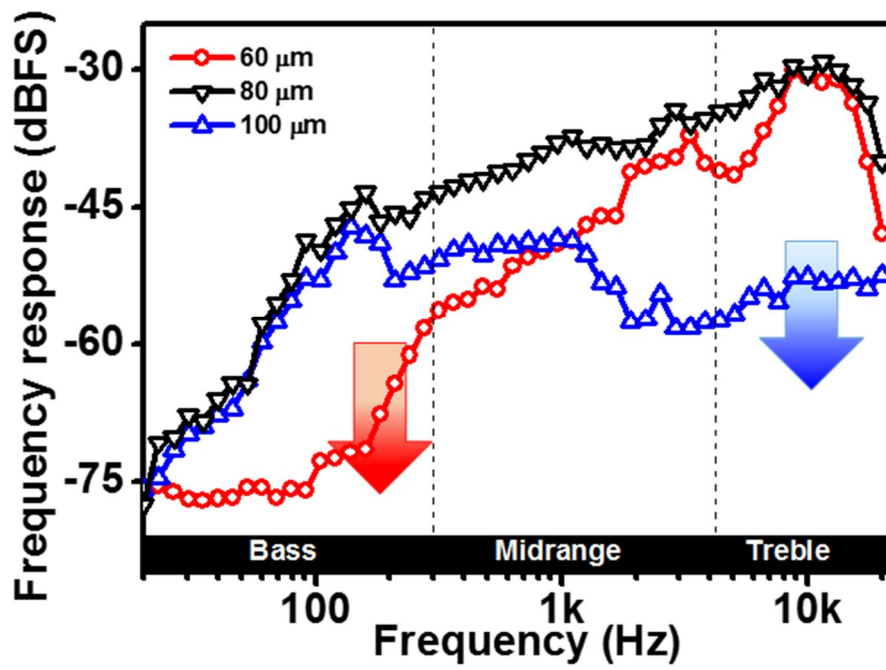
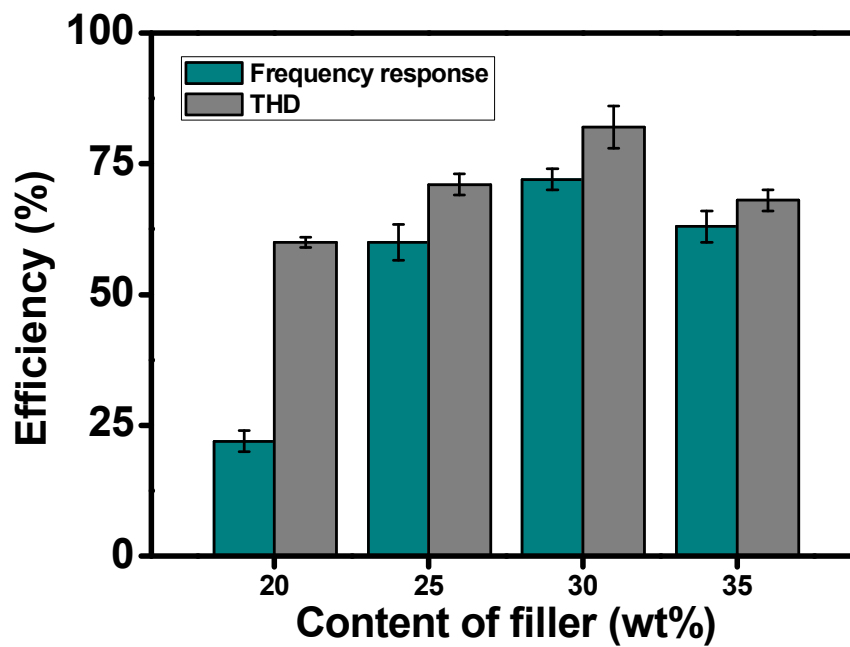
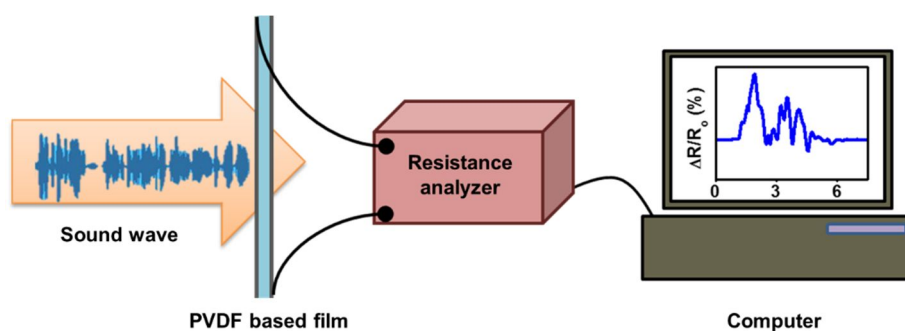


Figure 70. The frequency response as a function of the film thickness.



**Figure 71.** Relative efficiency of the actuators performance compare to the pristine PVDF acoustic actuator at 100 Hz as a function of the filler content.



**Figure 72.** (a) The schematic illustration of measurement setup to investigate the PVDF based acoustic analyzer. The real time change in the resistance of the urchin-like ZnO/PVDF hybrid film as the acoustic analyzer was monitored during speech.

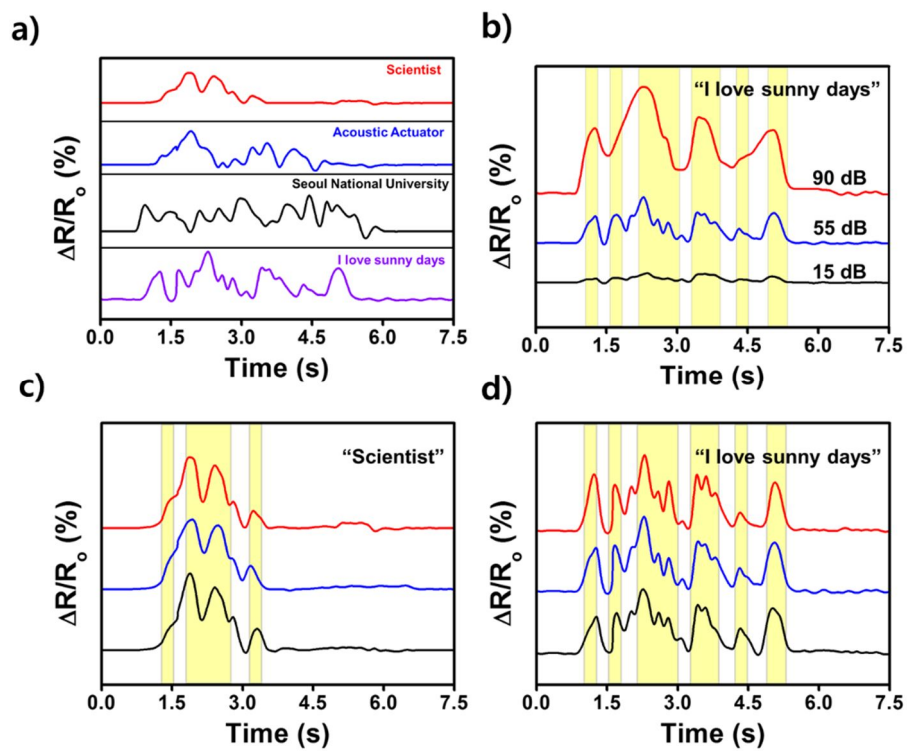


**Figure 73.** (a) The real time change in the resistance of the urchin-like ZnO/PVDF hybrid film as an acoustic analyzer. (b) The phrase “I love sunny days” was tested in different decibels. Each spoken words and phrases show unique I-V peaks as a function of time (c-d).

#### 4. CONCLUSIONS

1. Nano-scaled ZnO fillers and thin PVDF film is able to provide light weight and flexible property for device. Moreover, PVDF based sensor can be simply fabricated because of easy to handle. In addition, utilizing rGO electrode will give competitive market price for future applications due to mass producible of GO. It is demonstrated the detection of two different independent stimuli, pressure and temperature simultaneously and in real time. The piezoelectric and pyroelectric properties of hybrid PVDF matrix with a ZnO nanofiller system enable to fabricate multifunctional gauge sensors. An 80- $\mu\text{m}$ -thick film (which is around 15% of the thickness of the human epidermis), which is a highly sensitive hybrid functional gauge sensor, and was fabricated from PVDF and ZnO nanostructures with graphene electrodes. Using this film, we were able to simultaneously measure pressure and temperature in real time. The pressure was monitored from the change in the electrical resistance via the piezoresistance of the material, and the temperature was inferred based on the recovery time of the signal. Our thin film system enabled us to detect changes in pressure as small as 10 Pa which is pressure detection limit was  $10^3$ -fold lower than the minimum level required for artificial skin, and to detect temperatures in the range 20–120 °C

2. The nanoneedle structure of ZnO with large aspect ratio and hexagonal vertical grown pyramid form could lower the elastic modulus of the hybrid film compared to the ZnO nanorod, which caused the improved piezoelectric effect. Therefore, it was successfully fabricated based on the ZnO nanoneedle/PVDF hybrid film. The nanoneedle structure of ZnO with large aspect ratio and hexagonal vertical grown pyramid form could lower the elastic modulus of the hybrid film compared to the ZnO nanorod. Due to its high permittivity, low polarization response time and outstanding durability, the hybrid film can be applied for a real-time pressure sensor to monitor the heart rate. Notably, the lowest detectable pressure of the hybrid film was as small as 4 Pa. Furthermore, the reduced graphene oxide (rGO) electrode-based Bluetooth antenna attained high peak gain (2.70 dBi) and radiation efficiency (78.38%), which was applicable to be used as an omnidirectional antenna to transmit wireless signal to the smart phone. Interestingly, the received wireless heart beat signal within a distance of 8 m was more sensitively measured on the radial artery than carotid artery without distortion and time delay, and it had a similar oscillation in comparison with the wire pressure sensor. This approach offers a valuable and promising tool for producing the commercial and continuous wireless pressure sensor for use in routine biomedical research and critical

healthcare.

3. A bass frequency response enhanced flexible PVDF based thin film acoustic actuator was successfully fabricated. High concentration of various zinc oxide (ZnO) was embedded in PVDF matrix, enhancing the  $\beta$  phase content and the dielectric property of the composite thin film. ZnO acted as a nucleation agent for the crystallization of PVDF. A chemical vapor deposition (CVD) grown graphene was used as electrodes, enabling high electron mobility for the distortion free acoustic signals. The frequency response of the fabricated acoustic actuator was studied as a function of the film thickness and filler content. The optimized film had the thickness of 80  $\mu\text{m}$  with 30 wt% filler content, and showed 72% and 42 % frequency response enhancement in bass and midrange compared to the commercial PVDF, respectively. In addition, the total harmonic distortion decreased 82 % and 74 % in the bass and midrange regions, respectively. Furthermore, the composite film showed a promising potential for microphone applications. Most of all, it is demonstrated that acoustic actuator performance is strongly influenced by degree of PVDF crystalline.

In summary, four different morphology of ZnO nanostructures were used as nanofillers for PVDF based thin film. Afterthen, the fabricated films were applied on various electronic devices. First, fabricated composite disk-like and rod-like ZnO/PVDF thin films, and used these structures to independently measure the pressure applied to the film and the temperature of the object used to apply the pressure. The pressure detection limit was  $10^3$ -fold lower than the minimum level required for artificial skin, could be monitored in real time, and the temperature could be inferred from the recovery time of the signal. Second, a simple and effective strategy to fabricate the highly sensitive, wearable and wireless pressure sensor is demonstrated. The incorporation of ZnO nanoneedle, which acted as nucleating agent, allowed for enhanced crystallinity, permittivity and reduced elastic modulus of the PVDF-based hybrid film. Furthermore, the high conductivity of rGO pattern made it possible to have a highly efficient and omnidirectional Bluetooth antenna to transmit wireless signal to the smart phone. Interestingly, the wireless signal for heart rate was sensitively monitored without distortion and time delay, and it had a similar oscillation compared to using the wire pressure sensor. Lastly, the PVDF based acoustic actuator performance can be effectively boosted by incorporating various ZnO structure, urchin-like and rod-like, using CVD graphene electrode. Most of all, it is confirmed the increased dielectric constant

and the high degree of crystallinity of PVDF, arising from the 3-dimensional hierarchical structure of urchin-like ZnO, certainly enriched the bass frequency response of the acoustic generator. Furthermore, the composite film showed a promising potential for microphone applications.

The PVDF-based thin films with various ZnO nanofiller have been successfully applied in a wide variety of applications, suggesting that these composite films showed a promising potential in many wireless based e-skin, pressure sensor, sonar, and acoustic devices.

## REFERENCES

- [1] S. H. Bea, O. Kahya, B. K. Sharma, J. Kwon, H. J. Cho, B. Özyilmaz, J. H. Ahn, *Nano Lett.* **2013**, *7*, 3130.
- [2] S. Wang, L. Lin, Z. L. Wang, *Nano Lett.* **2012**, *12*, 6339.
- [3] P. Calvert, *Nature*, **1975**, *256*, 694.
- [4] A. J. Lovinger, *Science*, **1983**, *220*, 1115.
- [5] V. K. Tiwari, D. K. Avasthi, P. Maiti, *ACS Appl. Mater. Interfaces*, **2011**, *3*, 1398
- [6] A. Bruna da Silva, C. Wisniewski, J. V. A. Esteves, R. Gregorio Jr, *J Mater Sci.*, **2010**, *45*, 4206.
- [7] V. Koval, J. Briancin, *Ferroelectrics*, **1997**, *193*, 41.
- [8] S. Yu, W. Zheng, W. Yu, W. Zhang, Q. Jiang, Z. Zhao, *Macromolecules*. **2009**, *42*, 8870.
- [9] P. Martins, R. Goncalves, P. M. Martins, M. Benelmekki, G. Botelho, S. Lanceros-Mendez, *J. Phys. Chem. C*. **2012**, *116*, 15790.
- [10] P. Martins, C. Caparros, R. Gonçalves, P. M. Martins, M. Benelmekki, G. Botelho, S. Lanceros-Mendez, *J. Phys. Chem. C.*, **2012**, *116*, 15790.
- [11] M. G. Kang, W. S. Jung, C. Y Kang, S. J. Yoon, *Actuators*, **2016**, *5*, 5.
- [12] J. L. Nelson, J.C. Fothergill, *Nano Tech.*, **2004**, *15*, 586.
- [13] S. F. Mendes, C. M. Costa, C. Caparros, V. Sencadas, S. Mendez-Lanceros, *J. Mater. Sci.*, **2012**, *47*, 1378.

- [14] P. Martins, R. Goncalves, P. M. Martins, M. Benelmekki, G. Botelho, S. Lanceros-Mendez, *J. Phys. Chem. C* **2012**, *116*, 15790.
- [15] K. Yoshinaga, J. Shimada, H. Nishida, M. Komatus, *J. Colloid Interf. Sci.* **1999**, *2*, 180.
- [16] S.-W. Bian, I. A. Mudunkotuwa, T. Rupasinghe, V. H. Grassian, *Langmuir* **2011**, *10*, 6059.
- [17] P. Linse, H. Wennerström, *Soft Matter*. **2012**, *8*, 2468.
- [18] A. R. Petosa, D. P. Jaisi, I. R. Quevedo, M. Elimelech, *Sci. Technol.*, **2010**, *17*, 6532.
- [19] Q. Leng, L. Chen, H. Guo, Jianlin Liu, C. Hu, Y. Xi, *J. Mater. Chem. A*, **2014**, *2*, 11940.
- [20] Z. L. Wang, *J. Phys.; Condens. Matter*, **2004**, *16*, R829.
- [21] O. Dulub, L. A. Boatner, U. Diebold, *Surf. Sci.*, **2002**, *519*, 201.
- [22] B. Meyer, D. Marx, *Phys. Rev. B.*, **2003**, *12*, 4977.
- [23] P. W. tasker, *J. phys. C: solid state phys.*, **1979**, *12*, 4977.
- [24] O. Dulub, U. Diebold, G. Kresse, *phys. Rev. Lett.*, **2003**, *90*, 016102.
- [25] Z. R. Dai, Z. W. Pan, Z. L Wang, *Adv. Funct. Mater.*, **2003**, *13*, 9.
- [26] P. X. Gao, Z. L. Wang, *Nano Lett.*, **2002**, *3*, 1315.
- [27] Z. W. Pan, Z. R. Dai, Z. L. Wang, *Science* **2001**, *291*, 1947.
- [28] S. Hashimoto, A. Yamaguchi, *J. Am. Ceram. Soc.*, **1996**, *79*, 1121.

- [29] Z. L. Wang, X. Y. Kong, J. M. Zuo, *Phys. Rev. Lett.*, **2003**, *91*, 185502.
- [30] D. Moore, C. Ronning, C. Ma, Z. L. Wang, *Chem. Phys. Lett*, **2004**, *385*, 8.
- [31] S. Park, J. An, I. Jung, R. D. Piner, S. J. An, X. Li, A. Velamakanni, R. S. Ruoff, *Nano Lett.*, **2009**, *9*, 1593.
- [32] M. A. Rafiee, J. Rafiee, Z. Wang, H. Song, Z.-Z. Yu, N. Koratkar, *ACS Nano*, **2009**, *3*, 3884.
- [33] Y. Shao, J. Wang, M. Engelhard, C. Wang, Y. Lin, *J. Mater. Chem.*, **2010**, *20*, 743.
- [34] L. J. Cote, R. Cruz-Silva, J. Huang, *J. Am. Chem. Soc.*, **2009**, *131*, 11027.
- [35] V. Strong, S. Dubin, M. F. El-Kady, A. Lech, Y. Wang, B. H. Weiller, R. B. Kaner, *ACS Nano*, **2012**, *6*, 1395.
- [36] D. V. Kosynkin, A. L. Higginbotham, A. Sinitskii, J. R. Lomeda, A. Dimiev, B. K. Price, J. M. Tour, *Nature*, **2009**, *458*, 872.
- [37] L. Jiao, L. Zhang, X. Wang, G. Diankov, H. Dai, *Nature*, **2009**, *458*, 877.
- [38] A. G. Cano-Márquez, F. J. Rodríguez-Macías, J. Campos-Delgado, C. G. Espinosa-González, F. Tristán-López, D. Ramírez-González, D. A. Cullen, D. J. Smith, M. Terrones, Y. I. Vega-Cantú, *Nano Lett.*, **2009**, *9*,

1527.

- [39] K. I. Bolotin, K. J. Sikes, Z. Jiang, M. Klima, G. Fudenberg, J. Hone, P. Kim, H. L. Stormer, *Solid State Commun.*, **2008**, *146*, 351.
- [40] J. Moser, A. Barreiro, A. Bachtold, *Appl. Phys. Lett.*, **2007**, *91*, 163513.
- [41] L. Xie, H. Wang, C. Jin, X. Wang, L. Jiao, K. Suenaga, H. Dai, *J. Am. Chem. Soc.*, **2011**, *133*, 10394.
- [42] S. Cho, K. Kikuchi, A. Kawasaki, *Carbon*, **2011**, *49*, 3865.
- [43] P. Sutter, *Nat. Mater.*, **2009**, *8*, 171.
- [44] K. V. Emtsev, A. Bostwick, K. Horn, J. Jobst, G. L. Kellogg, L. Ley, J. L. McChesney, T. Ohta, S. A. Reshanov, J. Rohrl, E. Rotenberg, A. K. Schmid, D. Waldmann, H. B. Weber, T. Seyller, *Nat. Mater.*, **2009**, *8*, 203.
- [45] R. M. Tromp, J. B. Hannon, *Phys. Rev. Lett.*, **2009**, *102*, 106104.
- [46] C. Pang, G.-Y. Lee, T.-i. Kim, S. M. Kim, H. N. Kim, S.-H. Ahn, K.-Y. Suh, *Nature Mater.* **11**, 795-901 (2012).
- [47] A. Pecora, L. Maiolo, F. Maita, A. Minotti, *Sensor Actuat. A-Phys.* **2012**, *185*, 39.
- [48] M. L. Hammock, A. Chortos, B. C. -K. Tee, J. B.-H. Tok, Z. Bao, *Adv. Mater.* **2013**, *25*, 5997.
- [49] J. S. Lee, K.-Y. Shin, C. Kim, J. Jang, *Chem. Commun.* **2013**, *49*,

11047.

- [50] D. –H. Kim *et al.* *Science*. **2011**, 333, 838.
- [51] P. W. Sutter, J. –I. Flege, E. A. Sutter, *Nat. Mater.*, **2008**, 7, 406.
- [52] S. Mao, K. Yu, J. Chang, D. A. Steeber, L. E. Ocola, J. Chen, *Sci. Rep.* **2013**, 3, 1696.
- [53] S. Bae, H. Kim, Y. Lee, X. Xu, J. –S. Park, Y. Zheng , J. Balakrishnan, T. Lei, H. Ri Kim, Y. I. Song, Y. –J. Kim, K. S. Kim, B. Ozyilmaz, J. –H. Ahn, B. H. Hong, S. Iijima, *Nat. Nanotechnol.*, **2010**, 5, 574.
- [54] T. Yamada, Y. Hayamizu, Y. Yamamoto, Y. Yomogida, A. Izadi-Najafabadi, D. N. Futaba, K. Hata, *Nature Nanotech.* **2011**, 27, 296.
- [55] A. Reina, X. Jia, J. Ho, D. Nezich, H. Son, V. Bulovic, M. S. Dresselhaus, J. Kong, *Nano Lett.*, **2009**, 9, 30.
- [56] R. Go´mez-Marti´nez *et al.* *Nature Nanotech.* **2013**, 8, 517.
- [57] H. Bi, K. Yin, X. Xie, J. Ji, S. Wan, L. Sun, M. Terrones, M. S. Dresselhaus, *Sci. Rep.* **2013**, 3, 2714.
- [58] S. Bhaviripudi, X. Jia, M. S. Dresselhaus, J. Kong, *Nano Lett.*, **2010**, 10, 4128.
- [59] K. Yan, H. Peng, Y. Zhou, H. Li, Z. Liu, *Nano Lett.*, **2011**, 11, 1106.
- [60] S. Chen, W. Cai, R. D. Piner, J. W. Suk, Y. Wu, Y. Ren, J. Kang, R. S. Ruoff, *Nano Lett.*, **2011**, 11, 3519.

- [61] A. Dato, V. Radmilovic, Z. Lee, J. Phillips, M. Frenklach, *Nano Lett.*, **2008**, *8*, 2012.
- [62] S. Cha, S. M. Kim, H. Kim, J. Ku, J. I. Sohn, Y. J. Park, B. G. Song, M. H. Jung, E. K. Lee, B. L. Choi, J. J. Park, Z. L. Wang, J. M. Kim, K. Kim, *Nano Lett.*, **2011**, *11*, 5142.
- [63] C. R. Herron, K. S. Coleman, R. S. Edwards, B. G. Mendis, *J. Mater. Chem.*, **2011**, *21*, 3378.
- [64] J. Wu, W. Pisula, K. Muellen, *Chem. Rev.*, **2007**, *107*, 718.
- [65] X. Yang, X. Dou, A. Rouhanipour, L. Zhi, H. J. Rader, K. Müllen, *J. Am. Chem. Soc.*, **2008**, *130*, 4216.
- [66] J. Cai, P. Ruffieux, R. Jaafar, M. Bieri, T. Braun, S. Blankenburg, M. Muoth, A. P. Seitsonen, M. Saleh, X. Feng, K. Muellen, R. Fasel, *Nature*, **2010**, *466*, 470.
- [67] J. Naciri, D. Shenoy, K. Keller, P. Gray, S. Crandall, K. Shashidhar, *Chem. Mater.* **2002**, *14*, 5134.
- [68] X. Yan, X. Cui, B. Li, L.-s. Li, *Nano Lett.*, **2010**, *10*, 1869.
- [69] A. K. Geim, K. S. Novoselov, *Nature Mater.*, **2007**, *6*, 183.
- [70] M. Segev-Bar, A. Landman, M. Nir-Shapira, G. Shuster, H. Haick, *ACS Appl. Mater. Interfaces*. **2013**, *5*, 5531.
- [71] B. C-K. Tee, C. Wang, R. Allen, Z. Bao, *Nature Nanotechnology*. **2012**,

7, 825.

- [72] W. J. Yu, S. H. Chae, S. Y. Lee, D. L. Duong, Y. H. Lee, *Adv. Mater.*, **2011**, *23*, 1889.
- [73] R. -H. Kim, M. -H. Bae, D. G. Kim, H. Cheng, B. H. Kim, D. -H. Kim, M. Li, J. Wu, F. Du, H.-S. Kim, S. Kim, D. Estrada, S. W. Hong, Y. Huang, E. Pop, J. A. Rogers, *Nano Lett.*, **2011**, *11*, 3881.
- [74] K. S. Kim, Y. Zhao, H. Jang, S. Y. Lee, J. M. Kim, K. S. Kim, J. H. Ahn, P. Kim, J.-Y. Choi, B. H. Hong, *Nature*, **2009**, *457*, 706.
- [75] E. S. Dellon, R. Mourey, D. Lee, A. Dellon. *Plastic & Reconstructive Surgery*. **1992**, *90*, 112.
- [76] J. S. Lee, K.-Y. Shin, O. J. Cheong, J. H. Kim, J. Jang, *Sci. Rep.* **2015**, *5*, 7887.
- [77] J. S. Lee, K.-Y. Shin, C. Kim, J. Jang, *Chem. Commun.*, **2013**, *49*, 11047.
- [78] J. Rödel, W. Jo, K. T. P. Seifert, E.-M. Anton, T. Granzow, D. Damjanovic, *J. Am. Ceram. Soc.*, **2009**, *92*, 1153.
- [79] P. Murali, *J. Am. Ceram. Soc.*, **2008**, *91*, 1385.
- [80] B. Panigrahy, M. Aslam, D. Bahadur, *Nanotechnology*, **2013**, *23*, 115601.
- [81] K.-Y. Shin, J.-Y. Hong, J. Jang, *Chem. Commun.* **2011**, *47*, 8527.

- [82] P. Martins, C. Caparros, R. Gonçalves, P. M. Martins, M. Benelmekki, G. Botelho, S. Lanceros-Mendez, *J. Phys. Chem. C*, **2012**, *116*, 15790.
- [83] S. Tan, E. Liu, Q. Zhang, Z. Zhang, *Chem. Commun.*, **2011**, 47,4544.
- [84] J. Y. Hong, E. Lee, J. Jang, *J. Mater. Chem. A*, **2013**, *1*, 117.
- [85] J. Shi, M. B. Starr, X. Wang, *Adv. Mater.* **2012**, *24* 4683.
- [86] V. Dua, S. P. Surwade, S. Ammu, S. R. Agnihotra, S. Jain, K. E. Roberts, S. Park, R. S. Ruoff, S. K. Manohar, *Angew. Chem. Int. Ed.*, **2010**, *49*, 2154.
- [87] C. Q. Chen, Y. Shi, Y. S. Zhang, J. Zhu, Y. J. Yan, *Phys. Rev. Lett.*, **2006**, *96*, 075505.
- [88] S. Alwarappan, A. Erdem, C. Liu, and C. Z. Li, *J. Phys. Chem. C*, **2009**, *113*, 8853.
- [89] J. Jang, J. Bae, M. Choi, *Carbon*, **2005**, *43*, 2730.
- [90] S. B. Lang, S. A. M. Tofail, A. L. Kholkin, M. Wojtas', M. Gregor, A. A. Gandhi, Y. Wang, S. Bauer, M. A. Krause, *Sci. Rep.* **2013**, *3*, 2215.
- [91] Z. Y. Jiang, G. P. Zheng, Z. Han, Y. Z. Liu, J. H. Yang, *J. Appl. Phys.* **2014**, *115*, 204101.
- [92] A. V. Murugan, T. Muraliganth, A. Manthiram, *Chem. Mater.*, **2009**, *21*, 5004.
- [93] H. H. S. Chang, R. W. Whatmore, Z. J. Huang, *Appl. Phys.* **2009**, *106*,

114110.

- [94] X. Qiu, *J. Appl. Phys.* **2010**, *108*, 11101.
- [95] M. D. Stoller, S. Park, Z. Yanwu, J. An, R. S. Ruoff, *Nano Lett.*, **2008**, *8*, 3498.
- [96] J. J. Yoo, K. Balakrishnan, J. Huang, V. Meunier, B. G. Sumpter, A. Srivastava, M. Conway, A. L. Mohana Reddy, J. Yu, R. Vajtai, P. M. Ajayan, *Nano Lett.*, **2011**, *11*, 1423.
- [97] Z. Zheng, Z. S. Lim, Y. Peng, L. You, L. Chen, J. Wang, *Sci. Rep.*, **2013**, *3*, 2434.
- [98] K. H. Kim, K. Y. Lee, J. S. Seo, B. Kumar, S.-W. Kim, *Small*, **2011**, *7*, 2577.
- [99] J. Cho, K. Shin, J. Jang, *Thin Solid Films*, **2010**, *518*, 5066.
- [100] K. -Y. Shin, J. -Y. Hong, J. Jang, *Adv. Mater.* **2011**, *23*, 2113.
- [101] M. Guo, P. Diao, S. Cai, *Journal of Solid State Chemistry*, **2005**, *178*, 1864.
- [102] M. H. Huang, S. Mao, H. Feick, H. Yan, Y. Wu, H. Kind, E. Weber, R. Russo, P. Yang, *Science* **2001**, *292*, 1897.
- [103] J.-J. Wu, S.-C. Liu, *Adv. Mater.* **2002**, *14*, 215.
- [104] B. Lim, J. Jang, *Angew. Chem. Int. Ed.*, **2003**, *42*, 5600.
- [105] Wu, S.-C. Liu, *J. Phys. Chem. B*, **2002**, *106*, 9546.

- [106] K. -Y. Shin, J. -Y. Hong, S. Lee, J. Jang, *J. Mater. Chem.*, **2012**, *22*, 7871.

## 국문초록

지난 수년 동안 집중적인 연구적 관심을 불러 일으키고 있는 유전성 소재는 압전, 초전기 그리고 강유전성의 성질등에 의하여 전자공학, 광전자공학, 촉매반응, 에너지 저장 및 변환, 생의학 등의 다양한 분야에 적용되고 있다.

본 연구에서는 다양한 형태의 산화아연을 제조하고, 이를 폴리비닐리덴다이플로라이드에 충전제로 사용하여 유연성 있는 박막을 제조하였으며, 이들의 형성 메커니즘과 기계적, 전기적 특성을 체계적으로 고찰하였고, 아울러 압전 및 열 센서, 스마트 무선 헬스케어 시스템 및 음향 작동장치로 응용 하여 살펴보았다.

첫째로, 열수 반응을 이용하여 판상형태, 수직형태의 막대모양, 침상모양 및 성게 형태의 산화아연을 제조하였고 이를 폴리비닐리덴다이플로라이드의 충전제로 사용하였다. 둘째로, 이렇게 제조된 필름의 물성을 확인 하였다. 충전제와 폴리비닐리덴다이플로라이드 의 결정성, 유전율 및 서로의 상호작용에 대한 분석이 이루어 졌다. 마지막으로, 이렇게 제조된 필름을 이용하여 필름의 고유의 특성인 압전과 초전기 성질을 이용하여 초미세 압력과 타겟 물질의 잔열을 이용하여 온도의 변화도 감지 할 수 있는 촉각 센서를 제조 하였고, 또한 이를 블루투스 칩과 연결하여 스마트폰과 연동 시켜 맥박에 의해 인가되는 압력을 스마트폰의 스크린 화면으로 실시간 감지 하게 하였다. 그리고 역압전성질을 이용하여 외부에서 전기적인 자극을

주어 필름의 표면에 진동을 유발하여 음파작동기로 사용 하였으며 또한 음성을 인식하는 마이크로서의 가능성도 제시하였다.

본 연구에서 총 네가지의 다른 모양의 산화아연과 폴리비닐리덴다이플로아이드간의 유전성 및 결정성에 대한 다양한 분석이 이루어, 상용화된 박막에 비해 압전, 초전성의 특성을 향상시킬 수 있었다. 무엇보다도, 제조된 박막은 매우 얇고 제조 방법이 간단하며 투명하고 플렉서블하여 다양한 여러가지 전자소자 응용분야에 폭넓게 활용될 수 있을 것으로 사료된다.

주요어: 폴리비닐리덴다이플로아이드, 나노 산화아연 증진제, 하이브리드 필름, 촉각센서, 음향작동기

학번: 2013-31306